Design of a Novel Concept for Harnessing Tidal Stream Power

A Major Qualifying Project submitted to the faculty of Worcester Polytechnic Institute in fulfillment of the requirements for the degree of Bachelor of Science

Submitted by:

Ian Costanzo

Alden Kelsey

Fiona Ogren

David Wians

Project Advisor:

Professor Brian Savilonis

Abstract

This project involved the design, manufacture, and testing of a novel water energy harvesting device. Inspired by biomimetic propulsion mechanisms, the device extracted power from flowing water with a competitive efficiency. A mechanical ribbon fin takes advantage of a swept volume; this device has the potential to outperform conventional turbines that extract power through a swept area. This advantage is best realized in low speed flow environments such as tidal streams or rivers. This technology is suited for small hydro installations, with the potential for scaling to higher capacity generation. Three prototypes were created, each advancing the concept to a form capable of extracting 14 watts of power with an average efficiency of 41%. Testing was conducted in WPI's Donahue Rowing Center, which served as a flow environment capable of flow speeds between 0 and 2 m/s. Several iterations of the fin were created and tested, differentiated by varying size and construction. Three sensors collected data for angular velocity, flow speed, and the force experienced by a brake. This data was then used to determine shaft speed, torque, power, and the phase velocity of the fin. These metrics established the efficiency and scalability of this technology.

Table of Contents

Table of Figures

Introduction

Water energy has long been a cornerstone of human civilization. Installations from small water wheels to massive hydroelectric dams have been constructed to help people complete tasks varying from grinding corn meal to powering cities. Hydro power has many applications and has great potential for small scale energy generation, with many small streams and rivers left untapped. Small hydro also has the benefit of being ecologically friendly and responsible. A small hydro energy generator that worked cohesively with its environment, with minimal impact, while providing power would have applications all over the world.

Currently, engineers are looking to the oceans as sources of previously untapped hydrokinetic energy. Tidal currents are a powerful and predictable energy source, and much development has been done on various turbine designs to take advantage of this resource. However, many of these technologies remain in their infancy and implementation has not yet progressed beyond a few small installations worldwide. An alternative to turbines for tidal energy capture could help to mediate concerns regarding safety for marine life and long-term device survivability.

The ribbon fin concept is based on a biological structure used for propulsion by various species of eel, particularly the ghost knife-fish. They have a long, ribbon-like fin that runs along the bottom of their bodies. This fin is used to provide rapid propulsion as it oscillates. It enables high maneuverability and provides high thrust forces, allowing the fish to swim agilely.

A mechanical ribbon fin is a long, continuous membrane suspended between masts for the purpose of propulsion or power generation. The benefit of the ribbon fin can be most clearly seen in its ability to extract power from flow without blocking the current. The ribbon fin design also limits hazards imposed on local fauna. The ribbon fin has shown great promise in robotic propulsion, especially at low velocities. This project explores the application of these fins in a power generation system.

Ribbon fin style mechanisms have been explored by artist Theo Jansen with his "Strandbeest" creations, and utilized by Northwestern University in their submersible GhostBot robot. Used for energy harvesting and propulsion respectively, these two mechanisms illuminated the possibilities of the ribbon fin. Theo Jansen’s work proves the system is moderately functional with air as the working fluid. Implementing a ribbon fin in a denser fluid such as water increases the amount of available power.

Inspiration came from both the biological system and the mechanically simple systems that were able to effectively produce and harness energy for propulsion. The simple systems were found to be robust, effective, and easy to build. Therefore, the idea to turn a propulsion system into a power generation system was a logical step.

Through the construction of three prototypes the team developed a novel ribbon fin energy capture technology for use in free running currents. The first prototype was a proof of concept model that laid the foundation for the mechanism design. The second prototype was a larger scale model and improved upon the original mechanism design and was fitted with a small fin to test the concept in a flow tank before further work was undertaken. The final prototype was larger still and sized to fit the dimensions of the testing environment. This model incorporated custom made eccentric cams with built in bearings and a hybrid acrylic and neoprene rubber fin. It was designed to enable testing of fin performance through easy replacement of different fin constructions and sizes onto the same mechanism.

The design decisions made were based on several constraints. These included stability, ease of manufacture, friction reduction, fin flexibility, and power capture optimization. To make an efficient power capture device it was crucial that the device take full advantage of one of its most unique characteristics; the ability to capture energy from a volume instead of an area of moving fluid. Typical freestream turbines capture power through a swept area, meaning that a relatively small fraction of the energy can be extracted from the flow. By capturing energy through a three dimensional swept volume the ribbon fin device has the potential to capture a higher fraction of the available energy in the stream.

To gauge the performance of the device, testing was conducted to determine the relationships between the flow speed of the water, the applied torque, and the rotational speed of the shaft. From these measurements power outputs and efficiencies were calculated. Testing was conducted in the Donahue Rowing Center using a custom testing apparatus designed to support the device and sensors, and to protect the tank from any possible damage. The device was tested with different fin constructions and fin heights. Testing various fin constructions was an entirely exploratory endeavor, allowing the team to investigate this new technology. Varying heights were also tested for one of the constructions, allowing for the extrapolation of results for larger scale iterations.

Once data was collected, analysis was performed using graphical methods to provide visual representations of the results. The power outputs, efficiencies, and torque speed curves generated in this analysis form a powerful tool to determine the viability of the design as an alternative method of power capture for free running current conditions in either rivers or tidal zones.

Background

Small Scale Energy Generation

Small scale energy generation provides local communities with control over their own resources and reduces dependence upon external power sources. Worldwide, most electrical energy reaches consumers via centralized generation plants connected to a distribution system supplying entire regions. Systems tailored to a local environment are often more sustainable and effective for the region. This strategy also increases security; bringing both independence from fossil fuels and the ability to avoid major grid failure.

Small energy generation plants often utilize wind, hydro, solar power, or a combination thereof. They are typically small plants with only a handful of wind turbines or a small collection of solar panels. These small scale plants are often more easily adopted by developing communities and industries due to the lower costs associated with installation and maintenance.

State of the Art for Hydro Energy Generation

Hydropower is a well-established method of energy generation, dating back centuries. Today, hydroelectric sources produce about 15% of the world's electricity. The majority of that power is generated by large installations like the Hoover Dam and the Three Gorges Dam, with the rest of that percentage generated by small hydro installations. [36]

Tidal Current Power

With the estimated extractable power from tidal streams exceeding 50 GW in the United States alone, there is great potential for the development of a large tidal current energy industry. [12] Tidal resources are highly concentrated in specific areas, typically in northern latitudes. The high rates of flow due to extreme tidal fluctuations in these areas are less common in other regions of the world, requiring specialized designs that are not universally applicable. Numerous designs and concepts have been put forth to capture the power of this resource, with the vast majority building upon different styles of cross-flow and axial flow turbines. [34] These designs are generally differentiated by their size, configuration of turbine-generator units, material choices, and mooring configurations. Of these many concepts, those from the Ocean Renewable Power Company and Atlantis Resources both show promise in a commercial setting.

The TidGen employs two or more cross-flow turbines connected to a permanent magnet generator unit has a rated capacity of 150kW. Presently, this system has reached a small scale deployment in the Bay of Fundy, Maine, with an eventual expected installed capacity of 5 MW. [23] This device has several advantages, easy installation, and adaptability through sizing and mooring. These should allow it to be deployed in a variety of locations rivers deep ocean currents.

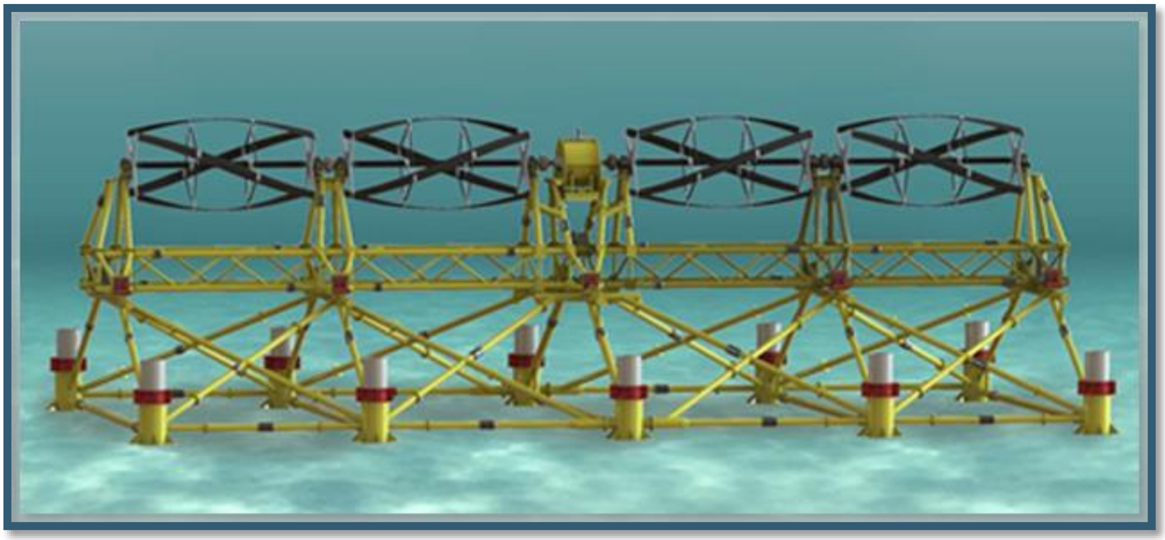

Figure 1: TidGen system rendering by ORPC. [23]

The AR1000 from Atlantis Resources is a horizontal axis turbine with a rated capacity of 1MW when currents meet or exceed 2.65 meters per second. It is designed to withstand conditions in the open ocean, and has proven both durable and capable of producing its rated capacity. The AR1500, though still in development, is the turbine of choice for the tidal power installation in the Pentland Firth, Scotland. When completed, it will have a rated capacity of 1.5MW when currents meet or exceed 3.0 meters per second. Additionally, the turbine has full yaw control to better maximize production by matching shifts in current direction. [1]

Figure 2: AR1500 from Atlantis Resources. [1]

A few other methods for harvesting energy from tidal currents are under development, such as the Stingray generator from The Engineering Business Limited, but none have passed the early testing and scale prototyping stage. The Stingray uses a unique design, featuring a large horizontal hydroplane, positioned perpendicular to the direction of the current. Oscillations are induced as the current passes over the hydroplane, pumping hydraulic cylinders to produce a flow of oil, which is used to generate electrical current by way of a hydraulic motor. The expected capacity of a single Stingray generator is 150kW, making it competitive with technologies such as the TidGen. However, the machine is very large, with a swept area of about 172 square meters. [8] The Stingray project is still early in its development, with the only working prototype deployed in the Yell Sound, United Kingdom.

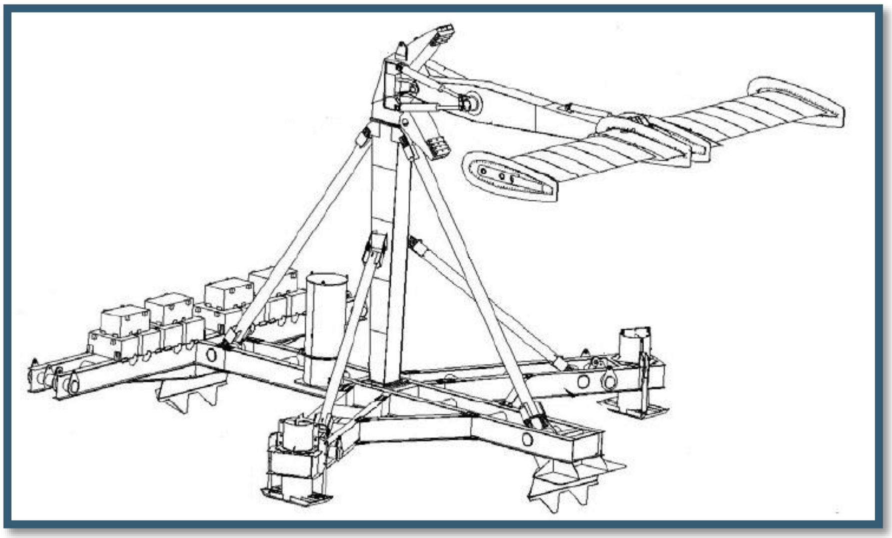

Figure 3: StingRay Generator by the Engineering Business ltd. [9]

On-shore Wave Power

Capture of wave energy that is incident upon the shoreline is a form of hydro-power that, although less developed than other technologies, has achieved some noteworthy successes. The total installed capacity of these technologies has not reached the megawatt range. Leading among these is an oscillating water column (OWC) device installed by Wavegen and Queen's University on the coast of the Scottish island of Islay. With a maximum installed capacity of 500 kW, and an average output of 200kW, the LIMPET, or Land Installed Marine Power Energy Transmitter**,** is the only on-shore wave plant that has been connected to the grid. [4] An OWC is a concrete enclosure built with a submerged opening. As waves break at the site, the water column inside of the enclosure rises and falls, driving air through a turbine. By using two Wells turbines, turbines which rotate the same direction for both incoming and outgoing airflow. The system not only represents the first on-shore wave generator to supply power to a commercial grid, it is also the longest running wave power generator.

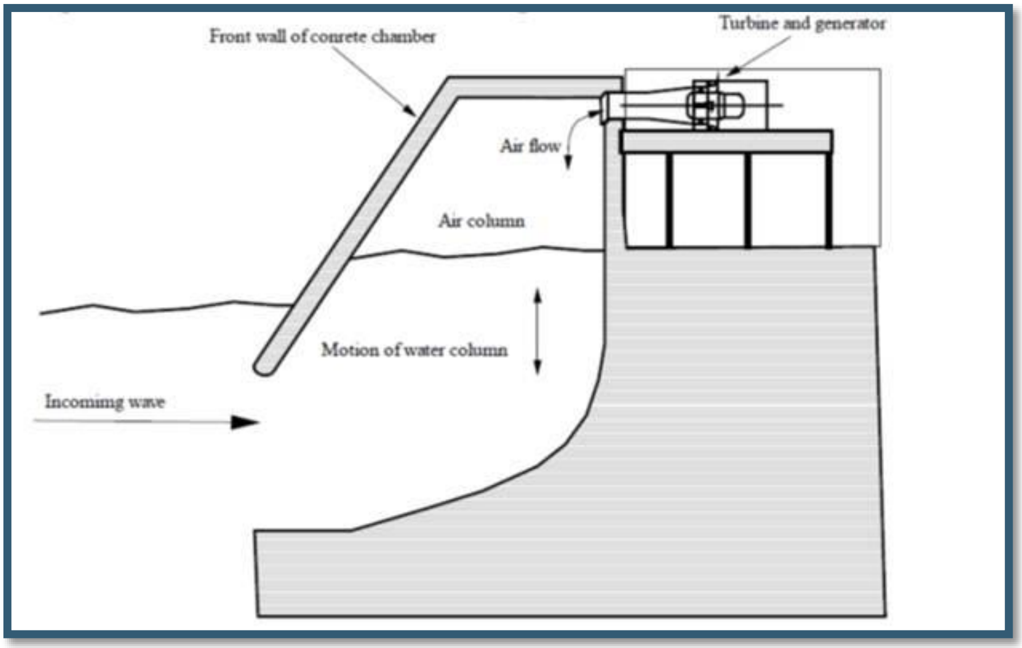

Figure 4: LIMPET onshore wave energy system. [31]

Others have sought to emulate the success of the LIMPET. The Mutricku Breakwater on the northern coast of Spain is an OWC that has been installed on an existing breakwater. This OWC system uses 16 chambers and is able to produce an average power of 174.5 kW at 12.12 kW per chamber. [32] Not all of the installations that have emulated the LIMPET have been successful. An OWC of similar construction to the LIMPET built on Pico Island in the Azores was plagued by technical difficulties and insufficient funding, and only reached a capacity of 30 kW. [4]

Diverging from the OWC technology are a few other designs, all of which use wave forces to pressurize fluid in hydraulic rams. A company called SDE ltd. has developed a shore based technology using a hinged float to generate power as it is lifted up and down by the impinging waves. This system however is not heavily documented, and has supposedly only topped 40 kW. [4]

Figure 5: Wave energy harvester from SDE ltd. [26]

Off-Shore Wave Power

Comprising over seventy percent of the Earth's surface area, the ocean is a vastly underdeveloped region with the potential to generate extremely large amounts of renewable energy. Ocean waves in particular are extremely energetic, especially beyond the continental shelf where waves travel without breaking upon the seafloor or coast-line. It is estimated that the total sustainable energy potential of wave energy along the U.S. continental shelf is 1,170 TWh per year, enough energy to meet nearly thirty percent of the nation's total annual power consumption. [13] In the past decade, numerous technologies and prototypes have been developed to harvest the energy contained in ocean waves. These technologies come in a few primary designs; the Point Absorber, the Line Attenuator, and the Oscillating Wave Converter.

The Point Absorber is a very simple method of harvesting wave energy. A buoyant cylindrical structure floats on the surface of the waves, rising and falling as waves pass beneath it. In order to convert this energy into electricity, the buoy is connected to a hydraulic system, pumping the fluid through electrical generators. The hydraulic system for a point absorber is typically set in one of two configurations; attached to the bottom or attached to the top of the point absorber.

When positioned on the underside of the point absorber, the hydraulic system acts as a single large piston, with the rising and falling of the buoy compressing hydraulic fluid. Hydraulic systems can also be mounted on top of the buoy, actuating mechanical lever-arms attached to a fixed structure to compress hydraulic fluid. A point absorber of the first variety currently operating is Ocean Power Technology's "PowerBuoy." Deployed in 2011, the Mark 3 PowerBuoy has a peak rating of 866kW, and averages 30-45% of that capacity.

[22] OPT plans to install PowerBuoys in large arrays; making the PowerBuoy a strong representative for the potential of Point Absorber technology to create sustainable energy.

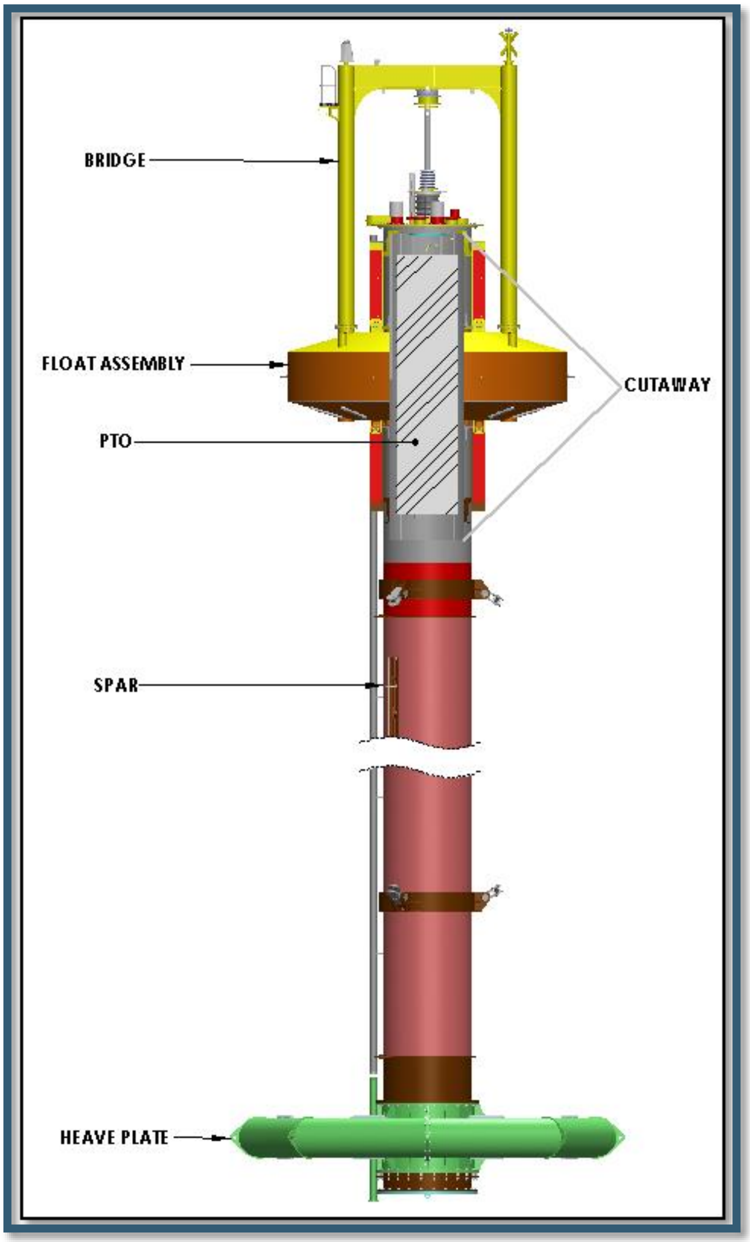

Figure 6: PowerBuoy from Ocean Power Technologies. [22]

The line attenuator is a long cylindrical mechanism, resembling a snake, which floats on the surface or just beneath the surface of the waves. Orientated fore into the wave front, sections of the attenuator rise and fall independently as a wave travels along its entire length. In order to maximize the electricity generated by a line attenuator the system must be long, with current machines reaching 140m. This design is very beneficial, allowing the machine to harvest more energy per unit of area than point absorbers. [29]

The most advanced line attenuator deployed currently is the Pelamis Wave system. The Pelamis is 140m long and 4m in diameter, and comprises five steel segments that are hinged fore and aft to one another. As a wave travels along the body of the Pelamis, sections rise and fall independently. Hydraulic pistons at the joints compress fluids that are then passed through generators located within each segment. Pelamis Wave systems have a target capacity of 750kW and have already proven themselves in full-scale deployments. An array of three Pelamis machines placed in Agucadoura, Portugal was able to reach an output of 2.25MW. [25]

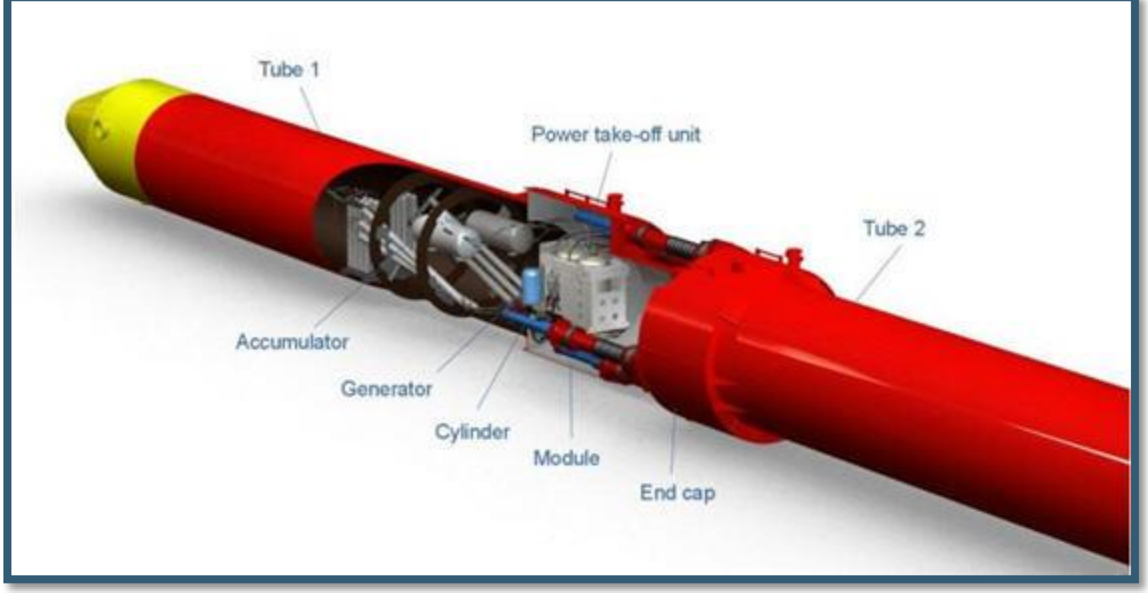

Figure 7: Cutaway view of Pelamis wave energy device. [24]

The oscillating surge converter is a wave energy converter that is mounted to the sea floor, and is either fully or partially submerged beneath the surface of the waves. As ocean waves approach the shoreline, the wave energy becomes much more linear, creating areas of very high horizontal energy. Hinged at its base, the OSC responds to this energy, moving back and forth as the waves push it. This back and forth motion is converted to electrical energy through a mechanical linkage, or a hydraulic system. This technology has the benefit of being contained beneath the surface of the waves, protecting it from violent storms that can be threatening to other ocean-based energy harvesting devices. Located in regions of the ocean with highly predictable wave patterns, OSC's have a very reliable and consistent output.

Small Hydroelectric

Small hydro installations are just that; small hydroelectric plants that are often built into existing infrastructures like old mills and small retaining dams. The qualifications for an installation being small hydro varies, although it typically ranges from 2MW to 25MW with 10MW being the average international standard. Worldwide there is believed to be about 173GW of small hydropower available; only about 75GW of that is tapped. [19] Most of North America and Europe have a well-established hydroelectric infrastructure; though there are still a large number of untapped mills and dams in those regions. South America, Asia, and Africa have a lot of potential for small hydro installations and are largely underutilized. [21]

In recent years countries in South America, Asia, and Africa have been exploring small hydro as an effective way to generate power, especially in their more remote regions. In 2013, Asia held the majority of small hydro capacity, with 65% of the world's less than 10MW hydro installations. African nations have been exploring small hydro as a means of rural electrification, with varying degrees of success. South and Central America also have a high capacity for small hydro installations; Chile has an estimated 7000MW of small hydro potential alone. [19]

Small hydro installations usually utilize some variation of a turbine that transforms water pressure into mechanical shaft power. The turbines are often optimized for the available infrastructure, with current deigns and installation practices achieving efficiencies of 60% to 80%. As the technology used is often small scale and built upon existing civil works, small hydro can be installed using parts that are widely manufactured all over the world. These installations often have little to no water retention, reducing environmental impact. [21]

Unfortunately a lack of incentives has made it difficult for small hydro to compete with well-established fossil fuel plants. This is unfortunate, especially since it's a resource that could easily be implemented in many developing rural and remote regions. Small hydro is cost effective and environmentally friendly. It can be implemented in a way that benefits a local region, giving the people there more control over their resources.

A test preformed in Northern Pakistan by Dr. Williams of Nottingham Trent University is an example of a successful small hydro installation. Centrifugal pumps were used as turbines and were paired with induction motors to generate power. This process relies on the local terrain's natural high pressure head to generate power with such a small mechanism. The benefits of this system focus mainly on its size, manufacturability, serviceability, and the minimal environmental impact. It is a proven alternative to larger cross flow turbines and gas generators. [35]

Power Conversion

Pumped Hydro Storage

Pumped Hydro Energy Storage (PHES) is the principal grid level energy storage option on the market today, though compressed air energy storage and battery technologies are beginning to take hold. It is utilized mainly in the United States, Japan and Europe. The premise is to store energy in the form of gravitational potential energy. Traditionally, water is pumped uphill during periods of low power use and generation takes place during high-energy draws. [6] This is accomplished using a pump and turbine combination.

There are two main types of pumped hydro energy storage; pure PHES and pump back PHES. In pure PHES, water cycles between an upper reservoir and a lower reservoir, creating a closed loop system. In pump back PHES, the system is more like a conventional hydroelectric dam, where water is pumped up to a reservoir and then released back into a body of water to generate power. [6]

The main benefit of PHES is grid stabilization. Currently only a small amount of the world's energy is stored, with most of the energy that goes to the grid being either used or lost. To prevent losses, the current tactic is to try to predict periods of high and low usage and then throttle power plants accordingly. This negatively impacts the overall efficiency of power plants. If excess energy could be stored, it would reduce the need for power plants be cycled on and off to meet demand, therefore allowing them to be run at a steady state with increased efficiency. [6]

PHES helps manage power outages. PHES has a very fast start time and can go from blackout to producing energy in under an hour. PHES is often compared to open cycle gas turbines due to their fast start and power demand response. This offers power distributors more control and can effectively smooth out their plants' demand cycles. PHES also adds a measure of security against catastrophic blackouts, providing emergency energy when other methods of production are unavailable. [6]

Hydraulic Systems

The kinetic energy of water can be converted into usable power by means of hydraulic systems. Many wave and tidal power systems utilize hydraulic cylinders. When used in a wave energy system the function of a hydraulic cylinder is to convert the force applied to the apparatus into fluid pressure, which activates a hydraulic generator to generate electrical power. [2]

Hydraulic circuits can function either as a closed or an open loop system. In a closed loop system the power transfer fluid is continuously recycled, passing through the actuators and being collected at low pressure in a reservoir before being pumped back to pressure in a separate reservoir. Hydraulic oil is typically used in closed loop systems because it is non-corrosive and has a low viscosity. In an open loop system the power transfer fluid is open to the environment. An example of an open loop system is pneumatics, where air is compressed from the surroundings, and exhausted back to the environment. An example more applicable to hydro-power is a marine system that uses ambient water as its hydraulic fluid. Advantages to such a system include mitigation of pollution risk, elimination of return lines, and compatibility with pumped-hydro energy storage systems. [14]

A typical closed loop hydraulic system is composed of five parts:

- Pump: applies pressure to the fluid
- Reservoir: stores compressed fluid
- Control system: sends power to the desired system components using valves
- Actuator: linear or angular hydraulic cylinders
- Accumulator: returns compressed fluid to reservoir

Fluid-power systems have several advantages over other means of power transfer. They experience low losses over short distances, they are able to generate very high forces with exceptional accuracy and power density, and they can be controlled using highly robust and relatively simple components. For an ocean power generator this robustness is particularly attractive given the difficulty inherent in servicing underwater machinery. There are disadvantages such as environmental contamination from leaking fluids. [14]

Challenges to Reliability

Reliability of an ocean power system entails its capacity to operate for extended periods of time without needing frequent replacements or maintenance. Reliability is a function of design, construction, materials, and components. In marine environments, the challenges faced for each of these factors are extensive. The environment of a hydropower system tends to be highly damaging as a result of the high energy densities seen during events such as storms, the unforgiving chemistry of the ocean environments, and due to biological degradation. The first is fairly straight forward; when a complex device with floats, cables, and moving parts is caught in a storm, the heavy winds and large waves can tear it apart if it is not robust enough to withstand or avoid the weather. The ocean environment damages systems due to exposure factors ranging from salt water catalyzed corrosion and UV light, to biological degradation from seabird feces and adhering organisms like barnacles and algae.

The field of maritime technology has produced strategies for averting the destructive nature of the ocean. To mitigate destruction from rough weather there are two options: avoid the danger entirely by coming ashore or retreating to the quieter seafloor, or to improve defenses with resistant materials and sturdy construction. The latter is more often observed in the systems deployed today. Two of the most successful offshore and near shore wave generators today rely on a defense specific to power generators, and that is to throttle the power takeoff to lessen the forces experienced by the joints and increase survivability. These systems are the Pelamis and the Oyster Wave Generators, both of which rely on hydraulic cylinders, decrease power takeoff by reducing the resistance of the hydraulic fluid and thus decreasing the force needed to displace the mechanism. Both of these systems are constructed from heavy coated steel, and rely on toughness to protect their inflexible components. Systems that rely on lighter materials and constructions to reduce weight and cost will need to take full advantage of the durability in flexibility in order to survive. [3]

Additional challenges facing the reliability of a hydropower generator are environmental. In naval technology, there are several ways to avoid corrosion from salt water. The first measure that can be taken is painting the exposed surfaces. A layer of zinc based primer and an epoxy paint will impede the corrosion process and increase the life of a marine steel structure by buffering the unstable iron from the electrolytic salt water. The next method is to utilize a sacrificial metal such as zinc which, having a lower oxidation potential, will oxidize instead of the iron when placed in electrical contact. The last technology, and one that has been proven successful in maritime applications, is cathodic protection. To do this, the entirety of the structure is charged to a voltage slightly greater than the oxidation potential of iron. This process results in current flowing through the hull, which electrochemically buffers all submerged surfaces. [33]

Challenges to Efficiency

As with any power generation strategy, efficiency is key to maximizing the economic and technological benefit of marine hydrokinetic energy converters. The design of the device and the arrangement of the devices within an array can affect the efficiency of the system on a whole. In the case of tidal currents, the placement of devices in relation to one another as well as their placement in the flow relative to oceanographic features can impact the efficiency of both the device and the entire system. As the current flows through the generator array, the total energy in the flow decreases; if generators are placed too close to one another their efficiency decreases. [10] With respect to increasing the efficiency of a design in and of itself, there are many factors to consider. For example, for any device that rotates in a stream, one way to increase efficiency and prevent damage is to design the device in such a way that cavitation is completely avoided. [5]

Economic Challenges

As marine hydrokinetic energy harvesting develops as an industry it must overcome key economic challenges, particularly when it comes to ease of integration into the grid, actual versus rated power outputs, reliability of power generation, and cost efficiency of the technologies. If technologies are to be widely adopted, and accurately evaluated for their economic value, they must be optimized. In the case of tidal current technologies, evaluating a potential site for a power plant must include an accurate estimate of the amount of power, and the number of hours that power generation can be expected. Often this is done by evaluating the number of hours that the velocity of the current is sufficient to generate the rated power of a technology. To accurately predict the power generation potential at a site you must take into account the full range of velocities at which the technology can operate and determine the amount of energy that can then be harnessed. This provides a clear determination of site suitability from an economic standpoint.

Appropriate sizing of a given technology depending on site conditions optimizes the economic value of the installation. [18]

Intermittency of generation can be a challenge with many renewable energy technologies; tidal current generators are no exception. However, unlike other resources, the tides are predictable, with two ebb and two flow tides every 24 hours. This makes integration into the power grid somewhat more feasible than with technologies such as wind turbines. Though the tides are predictable, the strength of the tide between spring and neap tides produces a wide swing in the expected energy output. This must be managed by altering the characteristics of the generator to be more efficient in the more common lower velocity streams, instead of expecting it to be able to fully utilize the higher energy potential during the high spring tides. [7]

The cost of marine energy development is another key economic concern. Factors that add to cost include manufacturing, installation, maintenance and operation, and research costs to develop the technology. All of these factors must be considered when determining the cost competitiveness of a new marine hydrokinetic power plant. If the technology is not cost competitive it is highly unlikely that it will be installed on a commercial scale. The cost per installed kilowatt is determined by the upfront capital cost and the combined estimated yearly operation and maintenance costs, this number is critical when determining the total cost of a system or power plant. The cost per kilowatt hour is what ultimately matters to utility companies as it determines whether the system is a viable market option. Often, the cost of manufacturing, installing, operating, and maintaining a marine power plant can be prohibitively expensive, especially when combined with the added challenge of its intermittency. [18]

Environmental Challenges

Though marine energy undoubtedly has numerous positive environmental impacts, there are also several environmental challenges to be considered for the area surrounding any installation, marine life, and, as discussed in the durability section, for the machines themselves. In the case of tidal current power, harvesting energy from tidal streams with a turbine slows the stream velocity. If a large array of turbines is installed, the slowing of the current could impact sedimentary deposition both on shore and on the sea bed, altering the landscape. [20]

At all phases of construction, operation, and eventually decommissioning of a marine power plant, impacts on the ecology of the surrounding area can be expected. To ensure that a development has as little ecological impact as possible, designs must consider several factors. First, the area of disturbed sea bed during construction and operation must be considered because it may be several years before the effects of such disturbances can be reversed. Second, the noise generated by moving machinery may affect communication between many species of marine life, as well as their health and reproductive potential. Electromagnetic emission from submarine cables and collision risk must also be considered for their potential impact on the navigation of magneto-sensitive marine species, and mortality of wildlife as it moves through the generation area. Less direct repercussions may include changes in ecological interactions such as competition between species, predation, and food availability. [11]

Wave Resources: Location and Origin

As with most every natural resource, the power of the ocean is not distributed evenly across all coastlines and seas. There are many factors influencing both the strength and the accessibility of ocean energies. An ocean wave is an interface phenomenon; it is not solely a product of the water but is also a product of the prevailing winds, which pull on the water by way of viscous shear forces over great stretches of open ocean. Therefore it is not necessarily strong winds that generate waves, but consistent ones. As waves are excited by the winds, the energy they carry is representative of the culmination of some of the wind energy present within a region of open ocean. This means that waves theoretically offer a natural form of energy concentration for wind energy, which is typically harnessed directly and in an un-concentrated form with traditional windmill style turbines. [30]

Because of the specific set of conditions necessary to produce quality wave energy, there are places where wave energy is specifically appropriate. Some of these places include the western shores of Europe, Ireland, the Pacific Northwest, specifically Oregon and Alaska, Southern Australia, and Chile. [30]

Tidal Resources: Location and Origin

The tides experienced by the earth's oceans are an effect of the gravitational pull of the moon and to a lesser extent the sun, linking the tidal cycle to the lunar orbit. The moon rises in the east and sets in the west, and so go the tides, running off of western shores, to travel across the open ocean as a very long wave and wash up on eastern shores. The tidal changes observed on coastlines are not a direct effect of the moon's gravity; instead they are the effect of deep ocean waves flowing onto the continental shelf to dissipate their estimated two and a half terawatts of potential energy. Tidal energy assumes different behaviors as a function of the topography of a region, before ultimately being lost through viscous dissipation. [27] When water runs onto a shelf, it must move between islands, into and out of bays, and around other geographic points. The effect of which is that the tidal rise and stream are not consistent across all shores. Areas of particularly high-energy tidal flows are often those with large but well protected inlets where the flow is forced to accelerate through the natural point of constriction. Examples of locations that experience this effect include the Cook Inlet in Alaska, and the Bay of Fundy between Maine and Nova Scotia. Extensive tidal power resources are also available in the seas surrounding the British Isles due to the exaggerating effects of the continental shelf.

Design Development

Ribbon Fin

Biological systems offer inspiration to many mechanical designs. The long fin featured along the length of many eels has provided inspiration for several novel propulsive systems such as the one used by Northeastern University engineers for their GhostBot swimming robot. Our design draws on these naturally inspired propulsive systems and reverses them to create a system that is driven by the water to harness energy. This ribbon fin concept was demonstrated by artist Theo Jansen to drive the mechanism that allows his Strandbeest kinetic sculptures to walk, powered only by the wind.

Figure 8: Strandbeest [15]

Figure 9: GhostBot [17]

The physics of this mechanism can be described by several equations, derived initially to describe its propulsive applications. The equation of primary importance when discussing the potential power output of a ribbon fin design for an energy capturing device is the surge force equation. In propulsion, this surge force is the force that actually propels the object through the fluid. For our purposes, a rough estimate of the possible energy captured by a ribbon-fin is given by surge force. The following equation was derived experimentally using computational fluid dynamics by a team of researchers out of Northwestern University. [28]

$$F_{surge} = C_1 \rho f^2 L_{fin}^4 \theta_{max}^{3.5} \left(\frac{h_{fin}}{L_{fin}}\right)^{3.9} \phi\left(\frac{\lambda}{L_{fin}}\right)$$

Where *C1* is an experimentally derived constant, {ρ} is the density of water, *f* is the frequency of the wave along the length of the fin, *L* is the length of the fin, {θ_{max}} is the angle of deflection from the center plane, *h* is the height of the fin, and {ϕ (λ/L)} is a function of the specific wavelength. [28] For more information regarding the exact calculations, models, and values used in the development of our design see Appendix A.

As this equation shows, the aspect ratio of the fin (h/L) is the principle driving factor in the determination of power output. The taller the fin, the higher the power output. This is due to the increase in torque to the shaft with the lengthening of the lever arm (fin height).

Established Methods

Before new wave energy harvesting devices can connect to the grid and provide electricity, each technology must go through a design and testing process. This process begins with numerical modeling and analysis, often performed by an engineering team using computer software. Modern technology allows for rapid and accurate modeling of complex systems, allowing designers to evaluate designs without the need to build numerous early prototypes.

Design processes often begin with rough calculations to get an idea of constraints and possible results. This helps with the solution brainstorming process by providing scale and scope to the problem. Tools like MathCAD and MATLAB can help engineers quickly generate equations and manipulate variables to analyze a range of possible results, eliminating impractical ideas.

To determine the limitations of each design, a design matrix that reflects the criteria deemed important is used. When a specific approach has been selected, the designs are developed and prepared for prototyping. Solid models and refined calculations allow for effective prototyping in a short period of time for preliminary testing. Manufacturing tools like laser cutting, 3D printing and CNC allow engineers to rapidly produce models in a short period of time.

This first round of testing is a crucial step in the design process, as it will give a fairly good indication on the quality of the chosen approach. These first tests will tell the engineers whether or not to continue with their chosen approach. These tests provide great insight into either refinements to the design that will serve to optimize it, or indicates new criteria that the team can use to prepare a new approach.

As strong as modern methods of numerical modeling are, they do not preclude the need for physical testing and experimental modeling. An incredible amount of information can be gathered by placing a scale model of an energy harvester into a test environment and seeing how much power it is able to generate. Live tests like this ensure that numerical modeling is accurate and representative of real world results. Wave and flow tanks provide a very strong test bed for hydro energy generation, as the properties of the waves and flow can be precisely controlled resulting in accurate and consistent testing.

Flow tank tests have fairly established test procedures that ensures quality data. Creating a good testing environment is a crucial step in the engineering process, as an inadequate test environment will result in subpar data. Having a good flow tank with dimensions and specifications that fit the purpose of the experiment is the most important resource to the test. It is also important to ensure that the flow velocity and volume of the tank is adequate to test the range of criteria required for the design. Position of the test subject and positioning of recording and measurement instruments are also important. Recording devices like cameras allow for collection of a lot of raw qualitative data, and can be very effective in determining the behavior of the test subject in flow. Measurement tools like flow meters need to be well positioned to give an accurate assessment of the environment the test subject is in.

Test data comes from a wide number of sources in a good flow tank test and need to be collected, analyzed and synthesized. Video and photo recordings, flow measurements, sensor measurements, calibration files, sampling frequencies, test duration, and human observations all come together to make a conclusive analysis of the test subject.

There are four important points to consider when testing a physical model: the power capture, power take off, structure and stability of the device and moorings, and the hydrodynamics of prototype. In fluids there are two factors that help define what is happening in all of these points and how to scale them, the Froude number and the Reynolds number. It is desirable to keep these two quantities constant from prototype to full scale as these numbers reflect how the test subject is interacting with its environment, which can be difficult to achieve at the small scale.

When designs for full-scale implementation are in place, individual components of the final machine must be individually tested, ensuring that each piece will be able to withstand the demands while in service. If all components meet their specifications, a full-scale model can then be deployed and tested. These full tests are crucial for a new technology in order to prove itself a viable method of energy capture. The process of live testing can be very time consuming, as the machine must be exposed to its final environment for a long period of time to ensure that it is working as intended.

Calculations and Physics

Before considering the fluidic interactions involved in the fin's operation, a conceptual analysis was conducted using the application PTC Mathcad. This approach focused on the Newtonian mechanics of extracting power from a moving stream of mass by reducing its velocity within a bounded region. Mass flows into the region through the wedge shaped area swept by the leading mast and is slowed by contact with the fin along the length of the device, transmitting power to the output shaft.

Fin Waveform for Design and Production

In order to design the fin used in physical models geometric syntheses were performed, driving the size and shape of the fins. These calculations can be found in Appendix B. The fin waveform is defined by the angular displacement between masts, and the phase velocity is defined by the wavelength and the shaft speed. The phase velocity represents the speed at which the waveform of the fin propagates along the fin axis, and will be referred to as wave speed for the purposes of this study.

$$\lambda = \frac{2*\pi}{\phi*n} * d \qquad (1)$$

Equation (1) describes the wavelength (λ) which is dependent upon three variables. These variables are fixed design criteria that can vary between design iterations. Both the number of masts (n) and the distance between the masts (d) are fixed. The angular position of the masts (ϕ) was fixed for all iterations of the device that were tested in this project. However, the angular position of each mast relative to the others can be varied to produce alterations to the wavelength and wave speed over the length of the device.

$$v_p = \frac{\lambda*\omega}{2*\pi} \qquad (2)$$

Equation (2) describes the wave speed (v_p). It is defined by the wavelength (λ) and the angular velocity of the output shaft (ω), which is dependent on flow speed.

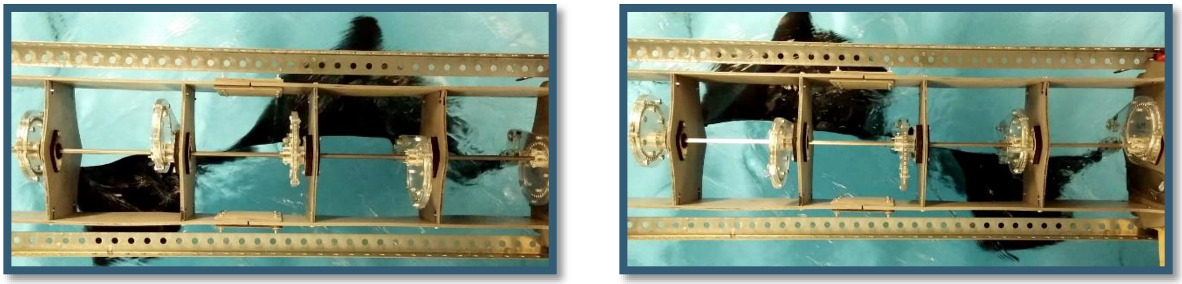

Figure 10: Propagation of the waveform on the fin.

Wave Speed Decay Model

A consequence of the wave speed dependency on wavelength and shaft speed is that a non-uniform waveform can be designed to produce a constant shaft speed that more efficiently extracts power from the flow. The advantage conveyed by a wave that slows as it propagates is that it can coincide with, and essentially govern, the deceleration of the water traveling within the control volume. The cylindrical section between the forward and aft swept areas defines the control volume. An image of the control volume and the cylindrical coordinate system used is shown in the figure below.

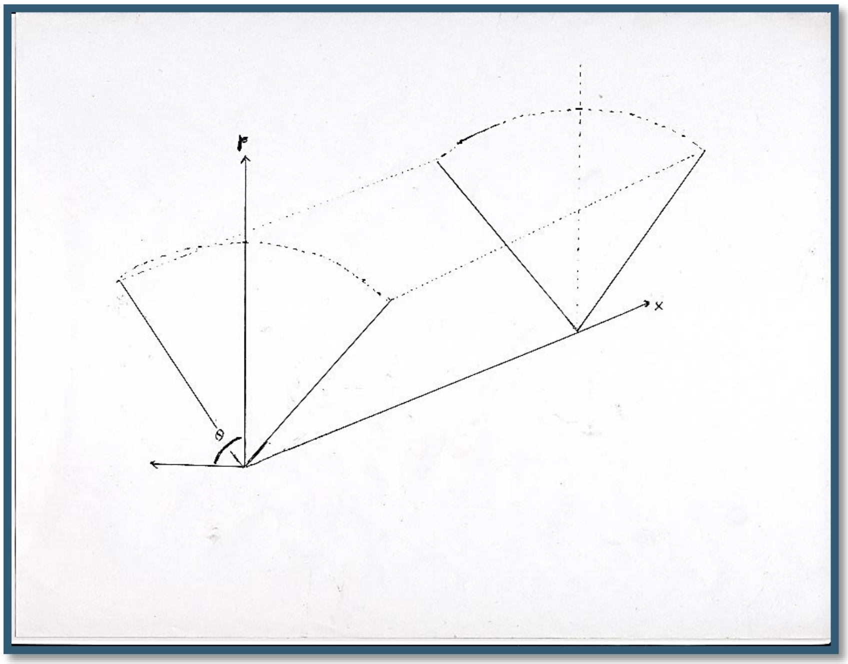

Figure 11: Sketch of Control Volume in Cylindrical Coordinates

To model and optimize for this behavior the wave is made to travel at the inlet flow velocity at the leading mast and decrease continuously as it moves along the axis. The profile of this decrease in wave speed is an inverse cubic so that the power, which has a cubic dependency on flow speed, decreases linearly. With a linear power takeoff profile each mast driver contributes uniformly to the overall shaft power. Shown below are the speed and power curves for a decreasing wave velocity. Independent variables (x) and (ϵ) correspond to axial position and the power reduction coefficient.

$$S(x,\varepsilon) = U_o * (1 - \varepsilon * \frac{x}{L})^3 \qquad (3)$$

$$P(x,\varepsilon) = \frac{1}{2} * \rho * A_o * S(x,\varepsilon)^3 \qquad (4)$$

Equation (3) describes the wave speed as it decreases along the axis. This relationship is governed by the flow velocity at the inlet (U_o), the length of the ribbon and control volume (L), the axial position (x), and the power extraction coefficient (ϵ). The power extraction coefficient represents the ratio between the power at the inlet and the power at the outlet.

Equation (4) defines the energy flux through axial sections of the control volume. In this equation, (ρ) is the density of water, (A_0) is the area of the section, and S(x,ϵ) is wave speed along the axis, as a function of axial position (x) and power extraction coefficient (ϵ).

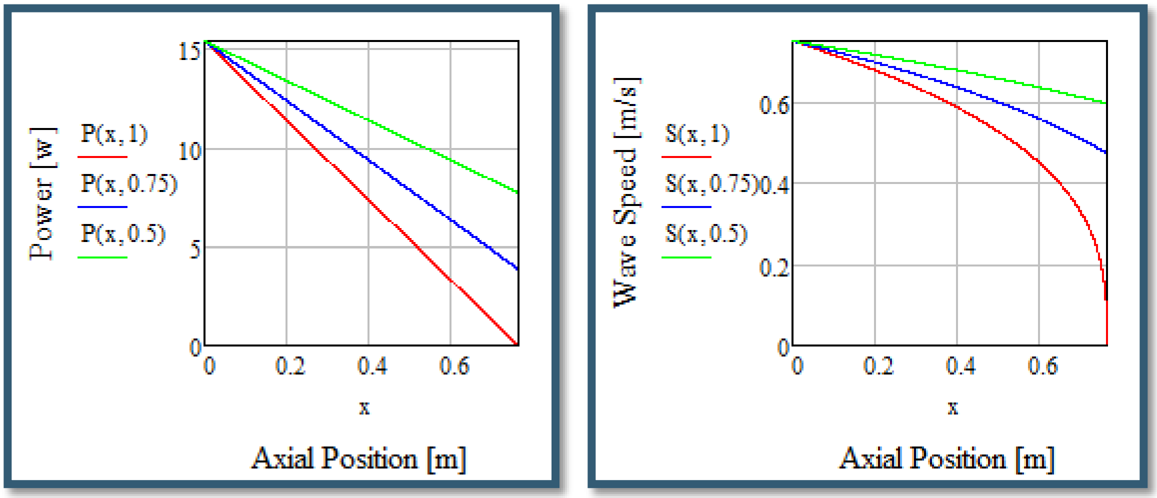

Figure 12: Power Decreasing Linearly (left) and Speed Decreasing Inverse Cubically (right)

To analyze the behavior of the water within the control volume it can be considered in wedge-shaped differential volume elements. When contacting the fin, individual differential volume elements are ejected from the control volume as new differential volume elements enter the control volume in accordance with conservation of mass. Elements enter the control volume from the front and travel in the direction of the flow. The differential elements are compressed axially and expanded radially, escaping through all boundaries of the control volume. This phenomenon reduces the amount of energy that the fin can extract from the flow. The expanding differential elements can be managed in two ways: expanding the radius of the fin along the length of the device; or maintaining a constant fin radius while decreasing the wavelength of the fin along the length of the device.

An installation of this device would have a maximum radius defined by the water depth and the structural strength of the masts. A fin with increasing radius would be able to operate on the same volume of water, capturing differential volume elements that would otherwise escape through the boundaries of the control volume. Under this design, the majority of the fin would have a radius less than the maximum allowable radius determined by its installed location, preventing the fin from accessing all of the energy available in the flow. It is likely that the advantages achieved by using a fin of expanding radius would not exceed the gains afforded by a constant maximized radius.

When adhering to the constant radius model, interesting fin geometries emerge. The following equation and figure illustrate the effect of varying the power extraction coefficient.

$$\theta(x,\varepsilon,n) = \theta_o * \sin(n * 2 * \pi * \frac{x}{L} * \frac{S(L,\varepsilon)}{S(x,\varepsilon)}) \tag{5}$$

Equation (5) describes the angular displacement (θ) of the fin relative to the leading mast at position (x), power extraction coefficient, (ϵ), and number of waves expressed (n).

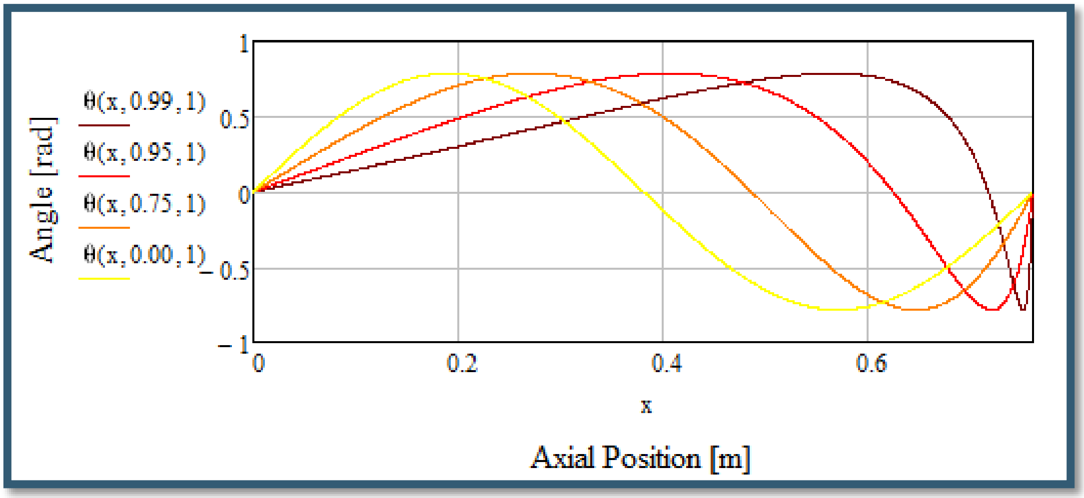

Figure 13: A one cycle wave at a selection of power extraction coefficients.

Each line on the graph above represents a top down view of the waveform as it would appear on a physical iteration of the fin. As power extraction coefficients near 1, the wave becomes very compressed as it approaches the aft face of the control volume. This is because at low speeds both the wave speed and the wavelength must drop rapidly in order to maintain a linear power extraction. Although a high power extraction coefficient is theoretically ideal, it would impose mechanical difficulties in a physical model. A balance can be found between power extraction and feasible constructions by reducing the power extraction coefficient. Even a moderate reduction in the power extraction coefficient results in a significantly more realistic waveform. The cost per unit area required to construct the fin, and the minimum stable wavelength between two masts both could limit the physical realization of this model.

The next figure shows waveforms with a 0.95 reduction coefficient at various cycle numbers ranging from half of a cycle to two cycles. The effect of cycle number on power extraction performance is related to the angle at which momentum is transferred from the water to the fin surface. As with the extraction coefficient, the optimum cycle number is dependent on practical limits like mast strength, cost of fin, and cost of masts. As the number of cycles increases, more masts are required to support the desired waveform, driving up costs.

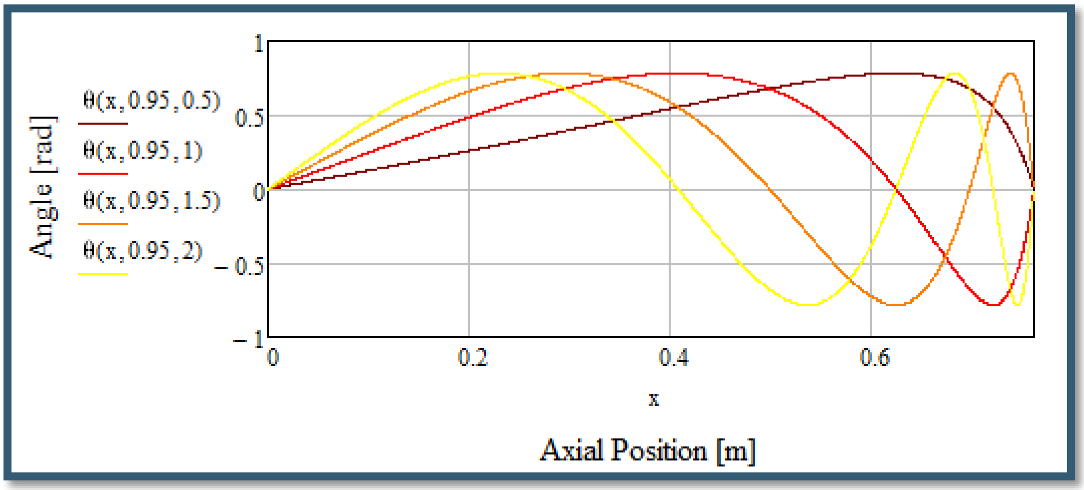

Figure 14: A 0.95 extraction coefficient fin at a selection of cycle numbers.

Beating the Betz Limit

Typical reaction foil turbines, for wind or tidal power, are subject to the Betz limit. This is a condition imposed by of conservation of mass moving through an essentially planar power extraction manifold. The propagating wave turbine uses a three dimensional, or extended, power extraction manifold. Thus it can operate continuously on a differential element of mass, slowing it from its intake velocity to the exhaust velocity, which can be near zero. The Betz limit is illustrated in the following figures. In the first, four cross sections are provided:

1. The stream area upstream.
2. The front of the turbine actuator disk.
3. The rear of the turbine actuator disk.
4. The stream area downstream.

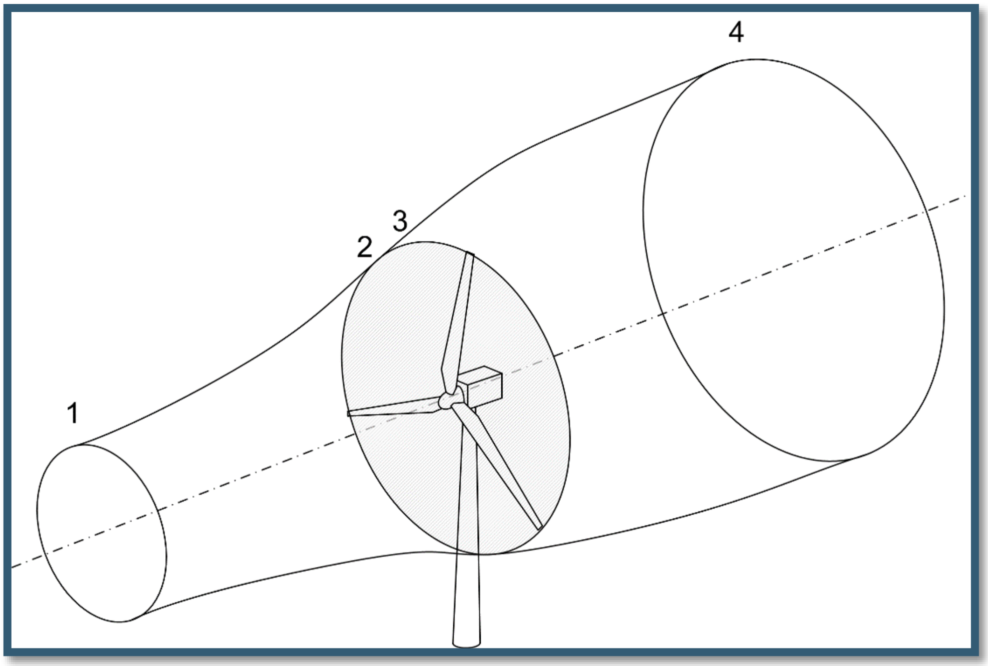

Figure 15: Stream of fluid moving through a planar turbine [37].

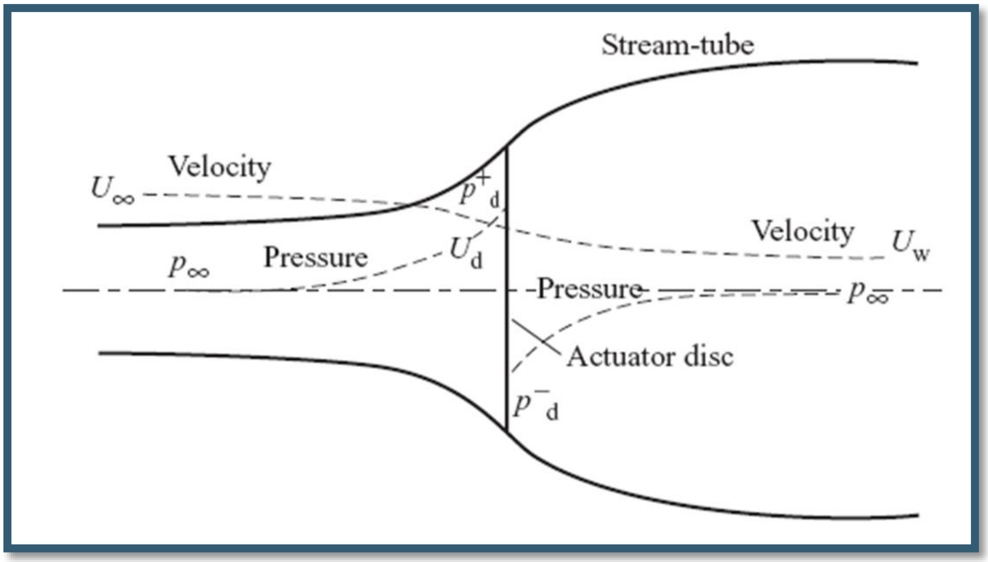

Figure 16: Velocity, pressure, and stream area changing across turbine disk [37].

In the figures above, areas 2 and 3 are compressed to a single plane. It can be seen that this lack of relative thickness forces the stream tube to expand significantly both before and after the turbine in order to conserve mass. While it is true that the propagating wave turbine must exhaust mass from its control volume, the volume is long enough relative to its intake area that there is sufficient distance to slow down the remaining mass to a small fraction of its intake velocity.

The model expressed here strongly supports the efficacy of the propagating wave turbine by suggesting that it may be capable of beating the Betz limit. However, experimentation will show if the assertion holds when transferred from the relatively simple Newtonian mechanics of the Wave Speed Decay Model to the complex domain of Fluid-Structure Interaction.

Methodology

This chapter outlines the project's constraints, design processes, manufacturing processes, and testing procedures. Decisions made are contextualized with charts, images, and written justifications.

Overview of Constraints

From the outset of the project, multiple constraints were established and fell into two main categories: logistics, and design. Each constraint imposed unique challenges on the project, forcing the team to plan and adapt to meet the goals and requirements of the project.

Key Design Constraints

Mechanism

- **Stability:** The mechanism must be structurally robust to withstand prolonged use under varying conditions.
- **Low Friction:** Frictional forces must be reduced wherever possible to maximize system efficiency and prevent wear.
- **Smooth Movement:** The mechanism must have a consistently smooth motion transfer to prevent unwanted directional forces and damage.
- **Transmission Angle Optimization:** Power transfer is maximized over a limited range of angles, the system should incorporate transmission angles within this range.
- **Modularity:** The mechanism must allow for adjustments to wavelengths of the entire system.

Fin

- **Strength:** The fin must be strong enough to withstand harsh environmental conditions, without tearing.
- **Modularity:** The design must allow for variable fin lengths and the addition of additional fin segments.
- **Flexibility:** The fin must be able to hold a sinusoidal shape and move smoothly through the full range of motion of the device.
- **Power Capture Optimization:** The fin must be stiff enough to effectively capture energy from the current and convert it into mechanical power.

Frame

- **Ease of Manufacture:** The frame must be simple to build and inexpensive.
- **Strength:** The frame must be strong enough to support the fin and mechanism with out bending.
- **Modularity:** The design should consist of few unique parts so that components can be easily modified or replaced if necessary.

Key Logistical Constraints

Time

- Entire project must be completed within 21 week time frame.
- Availability of WPI facilities limits available time to manufacture and perform tests.
- Iterative engineering design process requires the fully-realized development of several smaller prototypes.

Financial

- Pre-determined budget affects key design considerations such as size and material.
- Fabrication techniques limited to tools available on campus. Outsourcing components imposes a significant financial barrier.
- Data acquisition tools can be expensive but are vital to the evaluation of mechanism.

In order to effectively deal with these constraints the project was divided into three main phases, which corresponded with the three-term duration of the project. The first phase consisted of project definition, background research, a literature review, and preliminary prototyping. A second phase encompassed the design and manufacturing of the device to be used for testing. The final phase involved the testing, data capture, analysis, and evaluation of the project.

Design

The design process comprised three major design iterations. The first was a small scale model to test kinematics and manufacturability, and was not subjected to submerged testing. The first prototype exemplified the mechanisms that would be used in all further prototypes and established design basics that would persist through all iterations. The second model used an upgraded mechanism and was extended axially. Used in limited flow tank testing, the second model produced qualitative data that helped to determine the feasibility of the design, refine manufacturing techniques, and drive what materials would be used for the final device. The final configuration was roughly three times the size of the second iteration and was designed to be used for quantitative analysis in a flow tank. It made improvements based on the previous model and incorporated additional testing apparatuses for the quantitative analysis of the device. When discussing the design of the device, it can be divided into four major components; the mechanism, the frame, the fin, and the dynamometer.

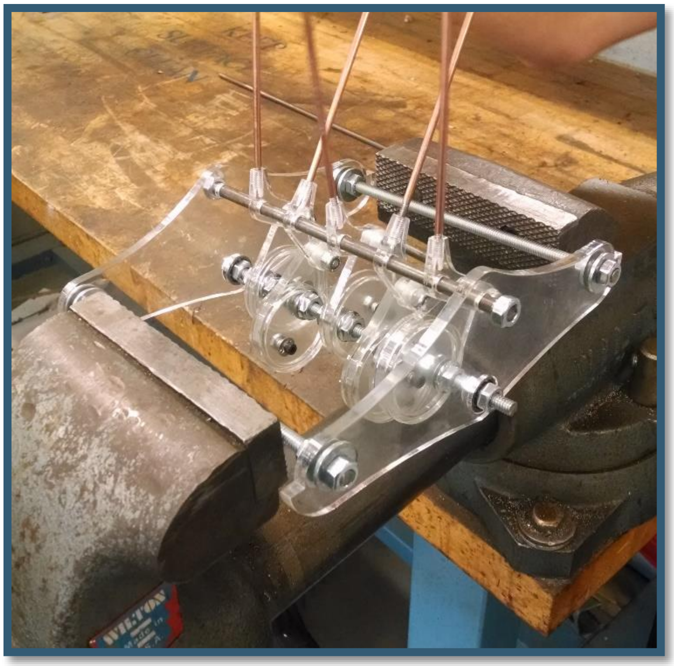

Figure 17: First prototype iteration.

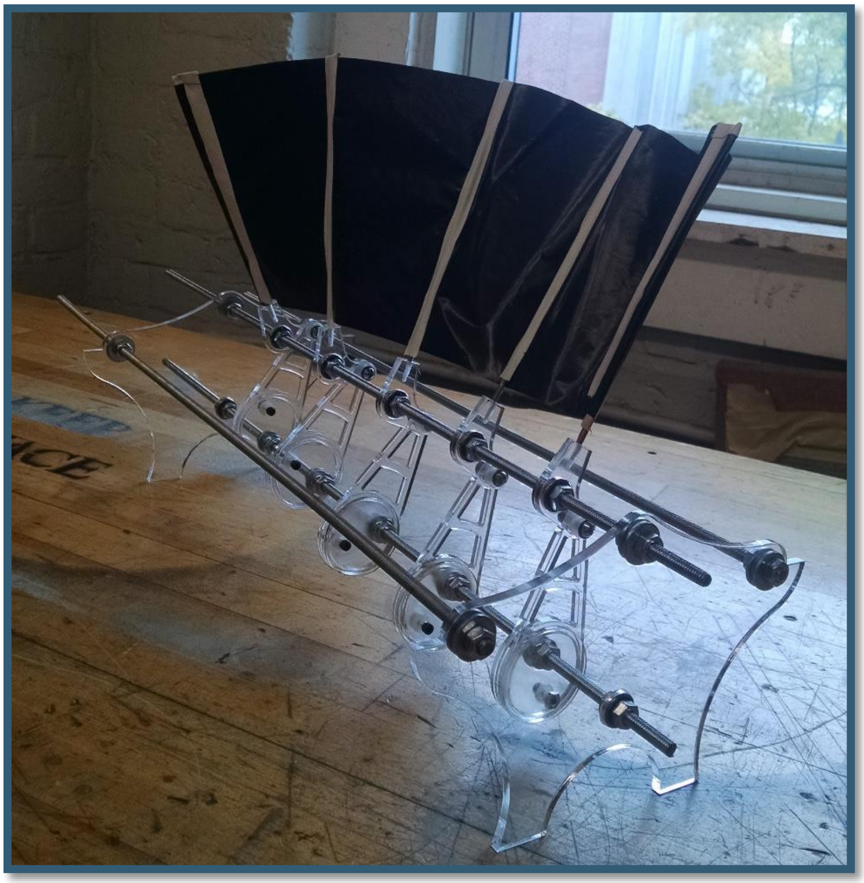

Figure 18: Second prototype iteration.

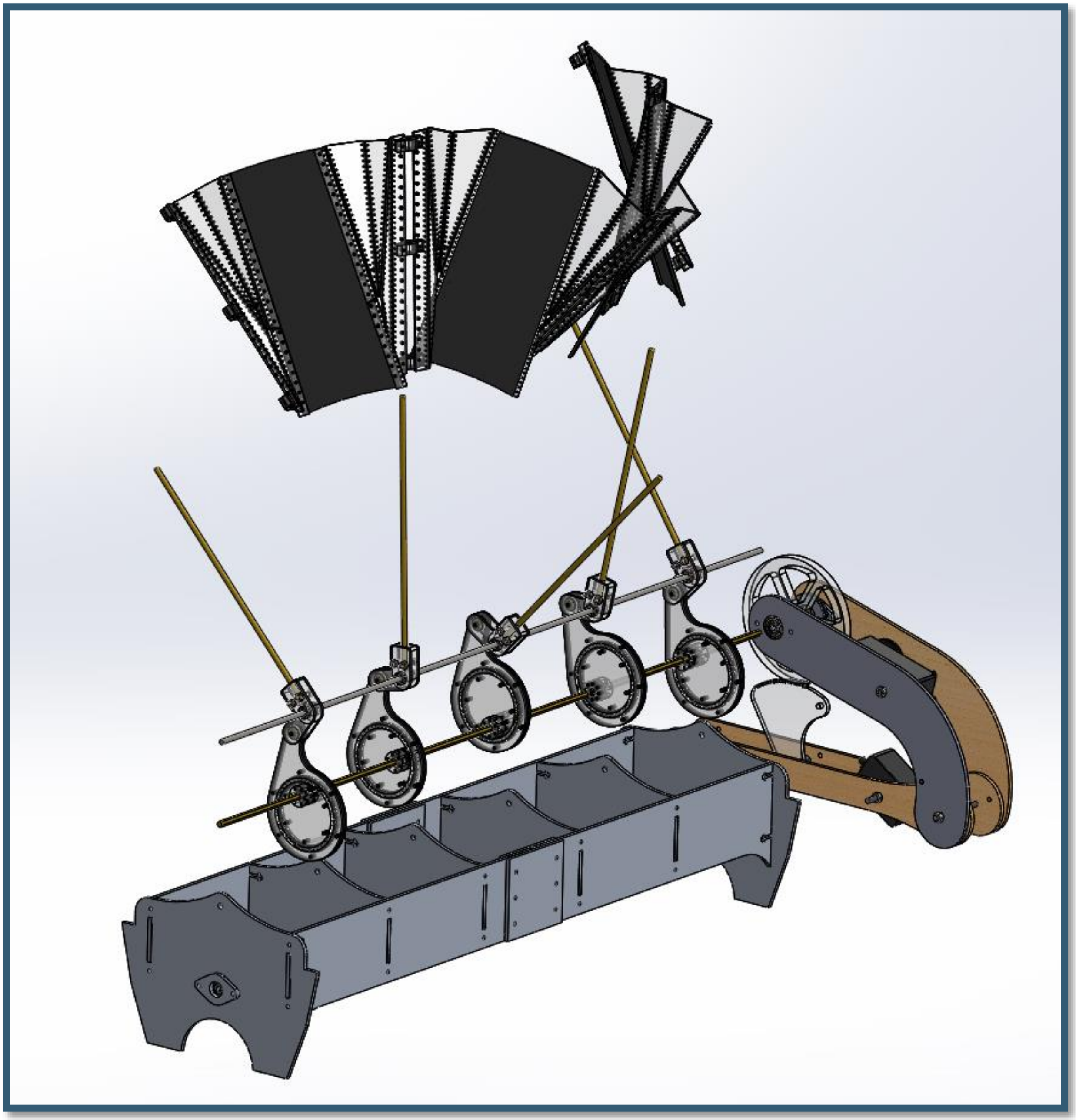

Figure 19: Exploded view of the four sections of the device assembly.

Mechanism

The mechanism in our device comprises an eccentric cam, rocker, and mast; the latter is responsible for governing the motion of the fin and converting the force exerted on the masts to torque on the shaft.

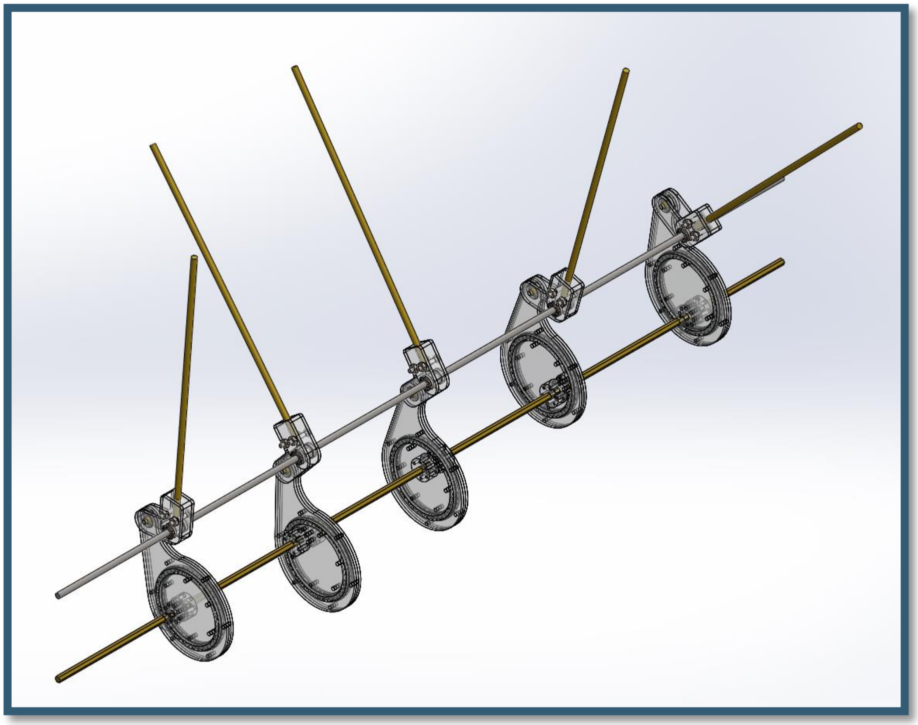

Figure 20: Solid model of mechanism.

A crankshaft is a mechanism used to convert reciprocating motion to rotational motion and vice versa. In our mechanism, a crankshaft would allow for the reciprocating motion of the ribbon fin to spin an output shaft, which is used to generate power. In a crank shaft, pins are offset from the main axis of the shaft and are attached to the connecting rods of the reciprocating device. Because the pins are not in-line with the main axis of the shaft, a linear force can induce rotation in the shaft.

Alternatively, an eccentric cam is essentially a crankshaft where the pin has been expanded to envelop the shaft, thus eliminating shaft discontinuity. By using an eccentric cam, it was possible to run a single solid shaft through all of the mast drivers. At the scale of our prototypes, the benefit of a single shaft was significant. A crankshaft would be heavier than an eccentric cam design, due to the material requirements associated with creating offset pins. The extra weight would have increased the inertia of the entire system, an effect that would be detrimental to producing power. However, there are drawbacks to an eccentric cam system. Because the length of the crank link is represented by the radius of the cam, the resulting cam design is twice as large as needed to have a comparable crank link. This in turn necessitates the use of bearings with large inner diameters. If the device were created at a larger scale a crankshaft may be more appropriate, where the inertia of the system is a smaller issue than the physical size of an eccentric cam.

The two earlier prototypes both used crude journal bearings made from laser cut acrylic. These bearings had high friction and required extensive lubrication for the models to perform well. Lengthening the distance between the output shaft and the rocker shaft decreased the stress and friction incurred on the eccentrics. Such a change was a major development and distinction between the first model and the second. The third and final model required a new technique. Friction had to be minimized, meaning that the pervious iterations of bearing had to be improved or replaced. The friction experienced in the earlier models precluded the acquisition of meaningful data, and purchasing bearings of the necessary size would be prohibitively expensive. The solution was to build bearings from scratch directly into the cam mechanism. To accomplish this, three layers of 0.125 inch acrylic were bolted together so that the outer two layers provided a slightly lesser diameter on the cam follower and a slightly greater diameter in the cam itself. This configuration created "rails" on which 0.25 inch steel balls could roll as a ball bearing assembly. The profile of the follower was designed to be asymmetrical so that it would not interfere with the pivot shaft while moving through its rotation.

The final mechanism, depicted below, had the cam resting within the follower on a track of 42 steel balls. The resulting bearing assembly caused little friction when compared to previous iterations and proved to be a viable design for the scale of the prototype.

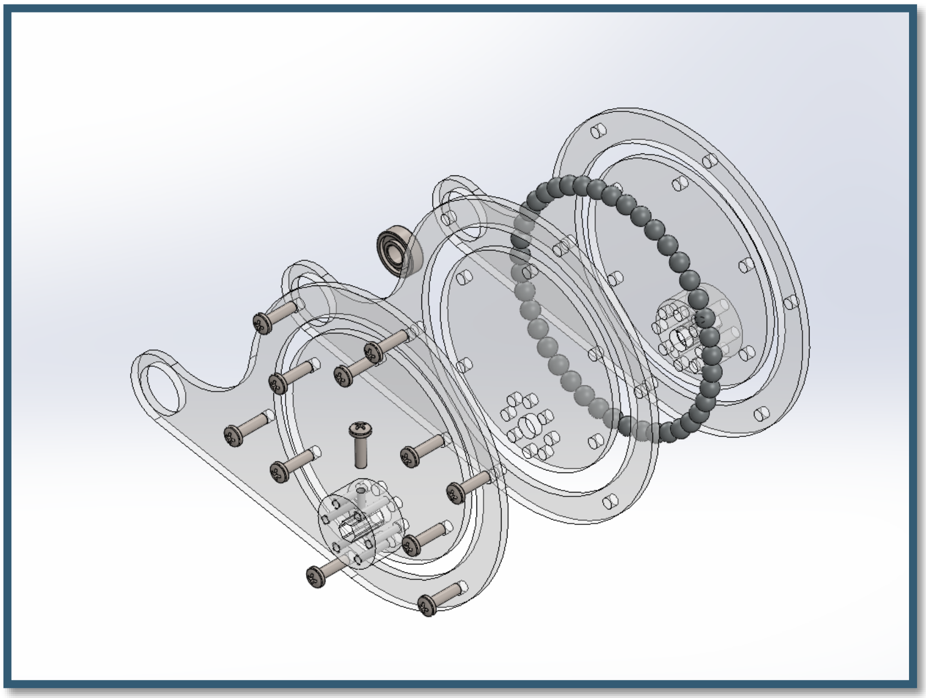

Figure 21: Exploded view of eccentric cam assembly.

Other designs existed for creating a large bearing, such as using off-the-shelf bearings to support a follower at three or more points on the cam, but these concepts did not offer the same stability or simplicity. Several lubricants were tested while using the journal bearings, and it was found that mineral oil was thick enough to remain in the bearing and inert enough to not pose a contamination threat to the testing environment. The custom bearing however did not require lubrication.

Another design feature that was retained through all levels of prototyping was the number of masts. Across all three prototypes, it was determined that five masts would be used so that a single wave could be supported at both extremes and at all three zeros. Although the mathematical model from the seminal paper suggested that a fin with between one and two cycles would be optimum, the concern was that too many masts would over constrain the flexibility of the fin and increase resistance. [28] It is possible that if the wavelength were too short relative to the number of masts, that the fin would not be able to support the desired waveform. The fin could then exhibit a folding behavior, where slack in the membrane would be pushed out of the desired waveform by the incoming flow.

Figure 22: Fin folding.

The fin and masts are connected to the four-bar linkage with a rocker assembly. The mast's rocker assembly is made of three main components: the mast base, and the two rockers. The mast base, threaded with a 1.0 inch deep 1/4-20 hole, allows for the masts to be threaded in place holding the ribbon-fin securely to the rest of the device. The mast base is placed between two identical rockers made from 0.125 inch acrylic. Each of these rockers house a single bearing, which allows the entire mast to move smoothly about the pivot shaft. By integrating two bearings into the mast-rocker assembly lateral thrusts imparted on the fin are less likely to apply unbalanced torques to the mechanism, thus reducing friction in the system.

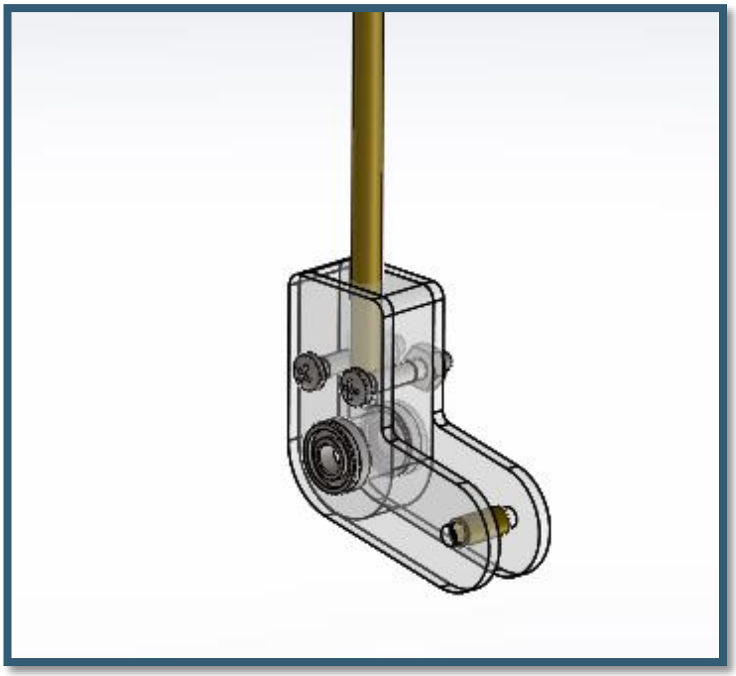

Figure 23: Rocker assembly, solid model.

Frame

For the first prototype the frame was composed of two 0.25 inch acrylic structural faces with four 1/4-20 threaded rods separating them. The two faces were designed with horizontal exposed edges to allow the fin to be suspended by the lip of the flow tank in Higgins Labs. Threaded rod was chosen for the ease with which components could be securely mounted and repositioned. All planar elements of the mechanism were secured on the rods between pairs of 1/4-20 nuts. This construction was simple and low cost, but did not provide long term stability and durability. However, durability was not an important consideration for this prototype, as its primary function was to prove that the mechanism design was feasible.

Transitioning to the second prototype represented the first time that the ribbon-fin was included on the model. To accommodate this, two changes had to be made to the frame: its overall length was increased and the separation between the output and pivot shafts was increased. The increase in length allowed for a larger distance between the eccentric cams, which was essential for sustaining the proper shape along the fin. Increasing the distance between the output and pivot shafts improved the kinematics of the mechanism, reducing the overall forces and friction. The two end faces of the frame were manufactured to include flat surfaces at its base. With this design feature, the entire device could be placed on a table to provide team members with an easy work environment.

The scale of the final prototype increased dramatically, extending the length to 38 inches and the height to 8.13 inches. With the increased length, the frame required additional strength and durability compared to the previous prototypes. To accomplish this, side faces and intermediate faces were added. Spanning the length of the entire device, the side faces had to be created from two interlocking segments, as the maximum length was limited by the table size of the laser cutter. Subjected to bending forces from the cam mechanisms, both the output and pivot shafts of the previous prototypes experienced significant warping. Intermediate faces were introduced to the frame, positioned between each of the cam-rockers. This prevented bending in the two shafts and improved the overall stability of the frame.

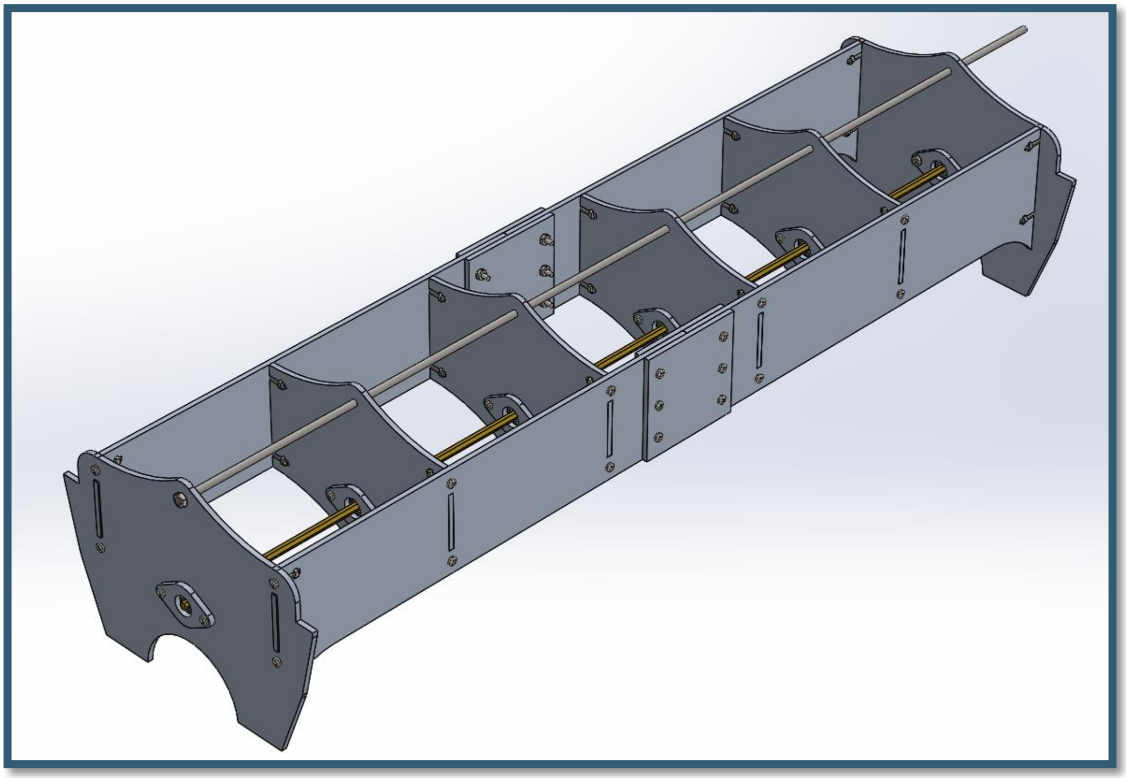

Figure 24: Frame assembly.

This iteration of frame was manufactured from 0.2 inch thick plywood. With the total area of frame increasing significantly between the second and third prototypes, plywood was chosen over acrylic to reduce material costs. Channels cut into the profiles of the plywood allow 8-32 machine screws to be passed through the planar outer faces of the frame, and secured to nuts held firm by the channels.

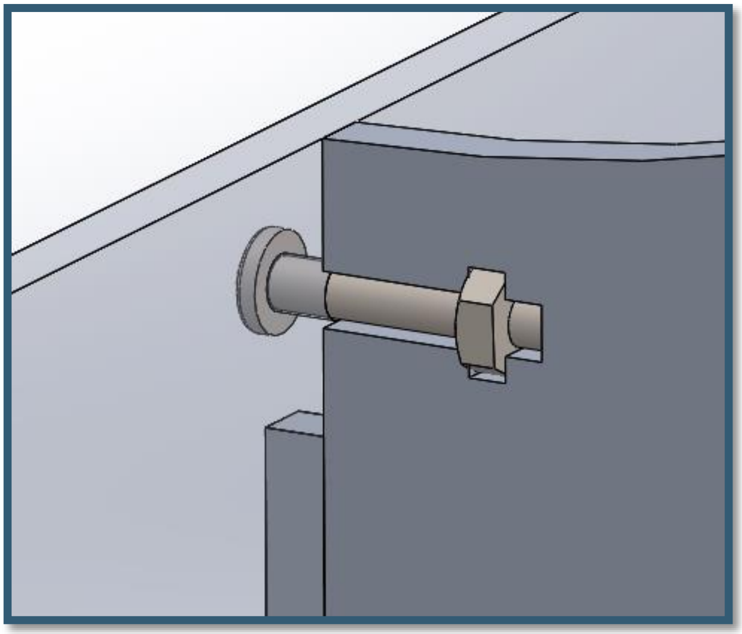

Figure 25: 8-32 Frame assembly

Measurements

Several possibilities for measuring the power being generated by the device were discussed for use during testing. These were: a fluid pump measuring the flow while modulating the pressure, an inductive motor measuring voltage and shaft speed while modulating resistance, and a friction brake to measure shaft speed while modulating torque. Ultimately the friction brake dynamometer was selected because its mechanical nature made it robust in a water environment, and controlling friction through the application of a normal force would not require calibration. The dynamometer consisted of two Vernier sensors: a rotation sensor to measure shaft speed, and a linear force sensor to measure the force applied tangent to the shaft. An acrylic wheel with a radius of 3 inches was affixed to the shaft so that the frictional force would be applied at a known radius, allowing torque to be calculated. The rotation sensor came equipped with a selection of pulley wheels which allowed it to be coupled to the shaft with an elastic belt. Shown below is the solid model of the dynamometer assembly.

The brake was an arc section which allowed the brake pad to always remain tangent to the friction wheel. The brake pad itself was a strip of neoprene connected to the brake at one end and connected to the force sensor at the other. The strip was not affixed along its entire length so that as it stretched it could roll onto and off of the brake without losing tangency. The normal force was supplied by the application of a manual force at the end of the brake arm. This allowed the torque to be effectively modulated during operation so that torque-speed curves could be generated.

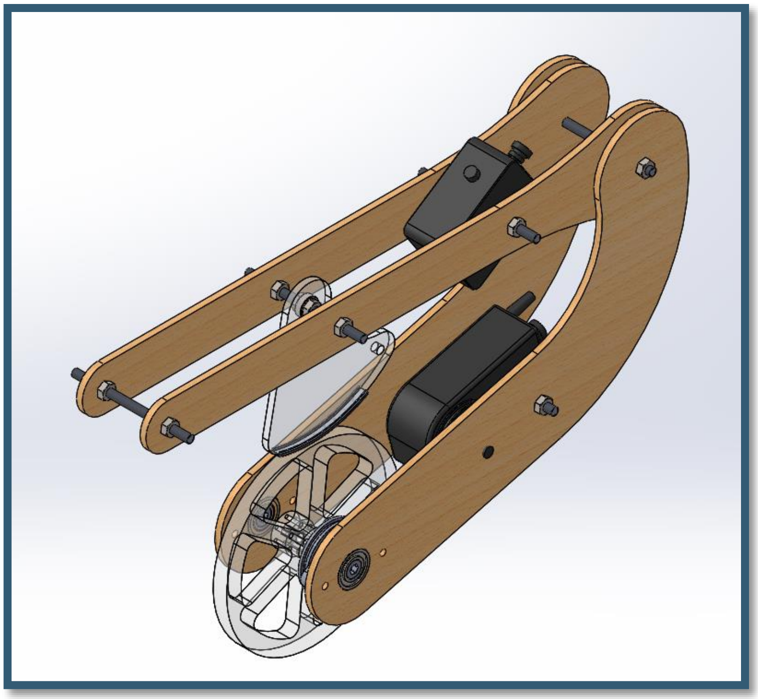

Figure 26: Dynamometer assembly, solid model.

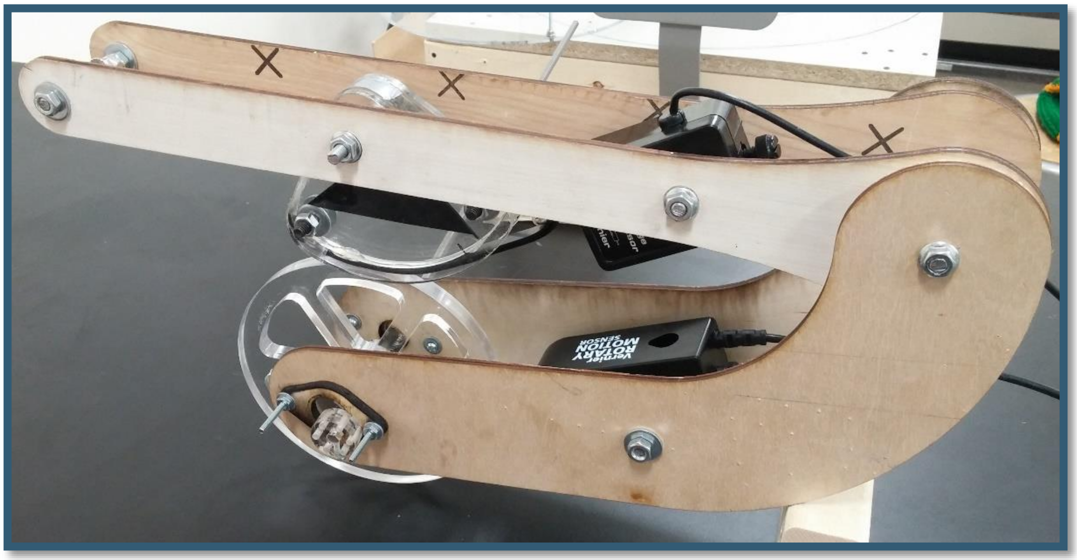

Figure 27: Dynamometer assembly.

Fin

To generate the geometry of the fin, MathCAD was used to compute the planar geometry necessary to create the three-dimensional wave surface. This planar geometry takes the form of an arc section with a width that is equal to the height of the fin, the length of the top and bottom edges of the fin define the curvature. In all cases, if the bottom edge of the fin existed exactly at the axis of rotation, it would have a length equal to the length of the device. As the radius increases, and the effects of the sinusoidal folding become more dramatically represented, the edge length increases, necessitating the aforementioned arc in the planar representation of the fin.

The fin geometry is driven by the change of angle between cams, the length of the fin, and the radius from the center axis of the bottom and top edges of the fin. The length of the fin was constrained by the size of the frame. The radius was constrained by the depth of the testing environment. The phase of the cams controls the wavelength of the fin. The planar geometry of the fin was determined using the following equations.

$$form = \theta_{max} * sin\left(2 * \pi * \frac{x}{\lambda}\right) \qquad (1)$$

$$edgeL(r) = \int_0^{len} \sqrt{1 + (\frac{d}{dl} * form(l) * r)^2 dl} \qquad (2)$$

Equation (1) represents the angular displacement from the vertical of the ribbon along its length. The peak-to-peak amplitude of the sinusoid generated is the "sweep" of the fin and was chosen to be 90 degrees so that the transmission angles at the rocker/cam-follower joint would not exceed 45 degrees, a conventional maximum. The maximum angular displacement of a mast from the vertical (θ_{max}) represents half of the total sweep. The wavelength is (λ), and (x) is the distance along the length of the fin. The actual angular displacement over the fin length curve is an imperfect sinusoid as it is driven by four-bar linkages. Equation (2) calculates the arc length along the ribbon as a function of radius and shape calculated in equation (1). This equation was used to find the length along the top and bottom of the ribbon fin, which were driving parameters in producing the planar fin geometry.

Neoprene was used for the fin because of its desirable material characteristics. A hybrid fin design was also developed, which used a combination of acrylic plates and neoprene sections that were sewn together at seams for flexibility. The fins were designed to be removable so multiple fin geometries could be tested. The full neoprene fins used lap joints over polyethylene tubing to mount the fin to the masts. The hybrid fin used acrylic clips to attach the plates to the mast.

Kinematics

To create the motion required to govern the ribbon fin, only a single four-bar linkage was needed. Unlike most applications of the Grashof four-bar, this design features the rocker driving the crank. Typically this would result in a lock point somewhere in the rotation of the crank. However, the unique angular position of each mast relative to the shaft means that the shaft is receiving torque at all times. This allows each individual linkage to be driven through its lock point without failing. Theoretically, there exist configurations in which the number of masts or the overall angular displacement along the shaft could produce lock points.

The arrangement of the links allows for the drive shaft and the rocker shaft to be oriented vertically. The arrangement of the linkage can be seen below.

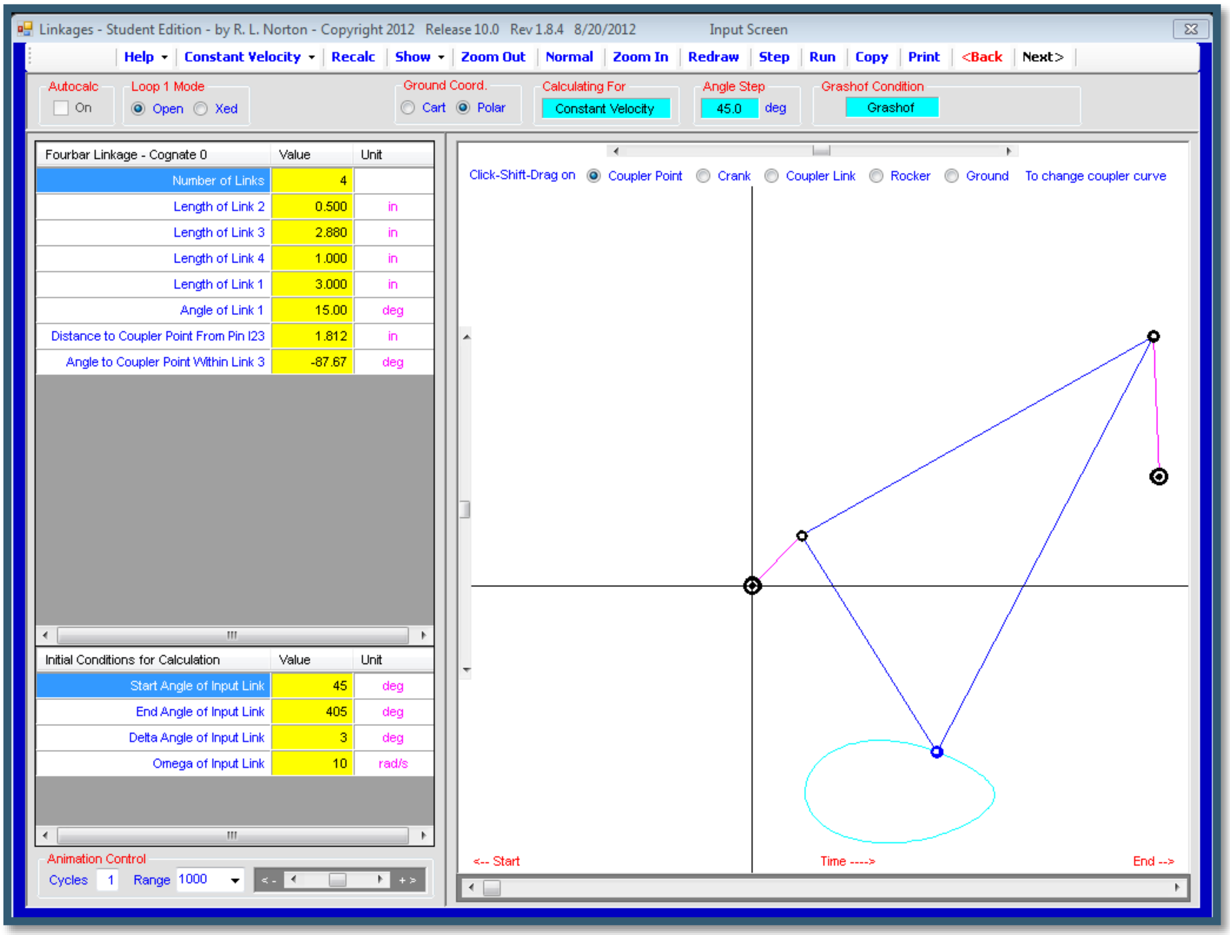

Linkages - Student Edition - by R. L. Norton - Copyright 2012 Release 10.0 Rev 1.8.4 8/20/2012 Input Screen

Autocalc: ☐ On
Loop 1 Mode: ● Open ○ Xed
Ground Coord.: ○ Cart ● Polar
Calculating For: Constant Velocity
Angle Step: 45.0 deg
Grashof Condition: Grashof

Fourbar Linkage - Cognate 0	Value	Unit
Number of Links	4	
Length of Link 2	0.500	in
Length of Link 3	2.880	in
Length of Link 4	1.000	in
Length of Link 1	3.000	in
Angle of Link 1	15.00	deg
Distance to Coupler Point From Pin I23	1.812	in
Angle to Coupler Point Within Link 3	-87.67	deg

Initial Conditions for Calculation	Value	Unit
Start Angle of Input Link	45	deg
End Angle of Input Link	405	deg
Delta Angle of Input Link	3	deg
Omega of Input Link	10	rad/s

Cycles 1 Range 1000

Figure 28: Linkage synthesis performed in LINKAGES.

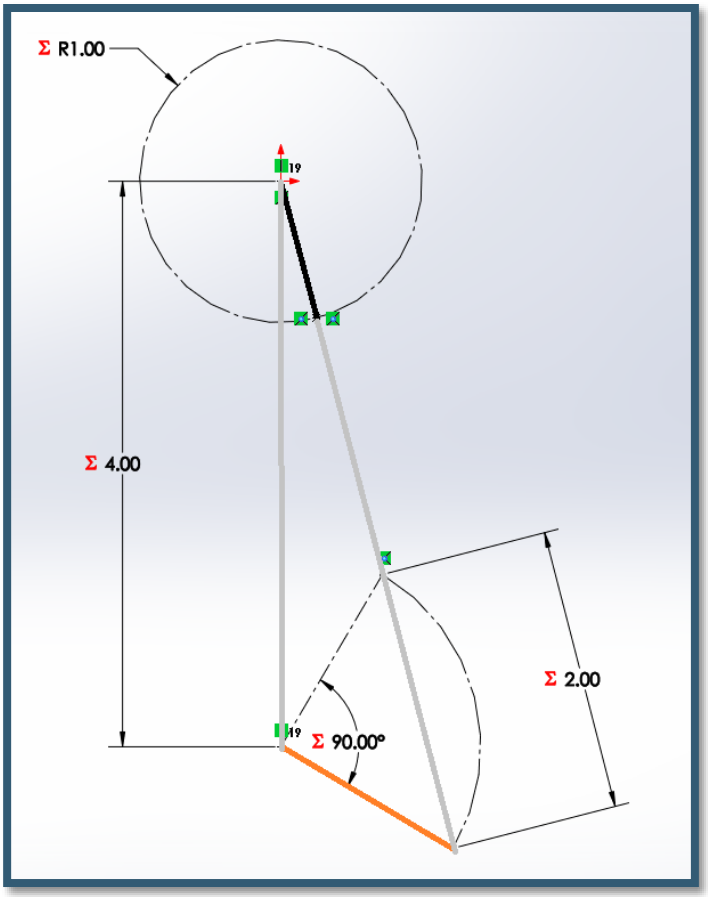

Figure 29: Linkage synthesis in SOLIDWORKS.

Modeling

Solid Modeling

Solid modeling tools were utilized consistently throughout all stages of the design and manufacturing process. Solid modeling with computer aided design software gave the team the creative power to conceptualize and evaluate new ideas in a short period of time. Preliminary models were created in SOLIDWORKS to establish the general mechanics and functionality of the mechanisms, and were used to create a prototype which confirmed that the design would function in a real-world environment.

As further iterations of the design were developed, Norton's LINKAGES was used to perform a linkage synthesis to define the four-bar mechanism which transmits power from the masts to the output shaft. The tool suite in LINKAGES creates a simple linkage synthesis platform that allows for easy modification of the linkage constraints, and the generation of the mechanism's output path. A symmetrical stroke was essential to the operation of the mechanism, and the data gathered from LINKAGES was used to govern the mechanism design in SOLIDWORKS.

SOLIDWORKS was integral to the design process at all stages of development. With dimensions for the linkages acquired from LINKAGES, eccentric cams were designed and implemented into a working solid model of the chassis. This fully realized model was examined and adapted to fit the constraints of our test environment. Material use was constrained to simple sheet products such as plywood and acrylic in order make use of a VLS 4.60 Laser Cutter. To facilitate this manufacturing process, all of the designs were converted to vector representation in DXF file format from the surfaces of the three-dimensional models. Additionally, SOLIDWORKS provided the team with a powerful collaborative workspace in which every component was accessible to all members of the team. This improved overall efficiency while ensuring that each individual contributed to the design of the entire mechanism.

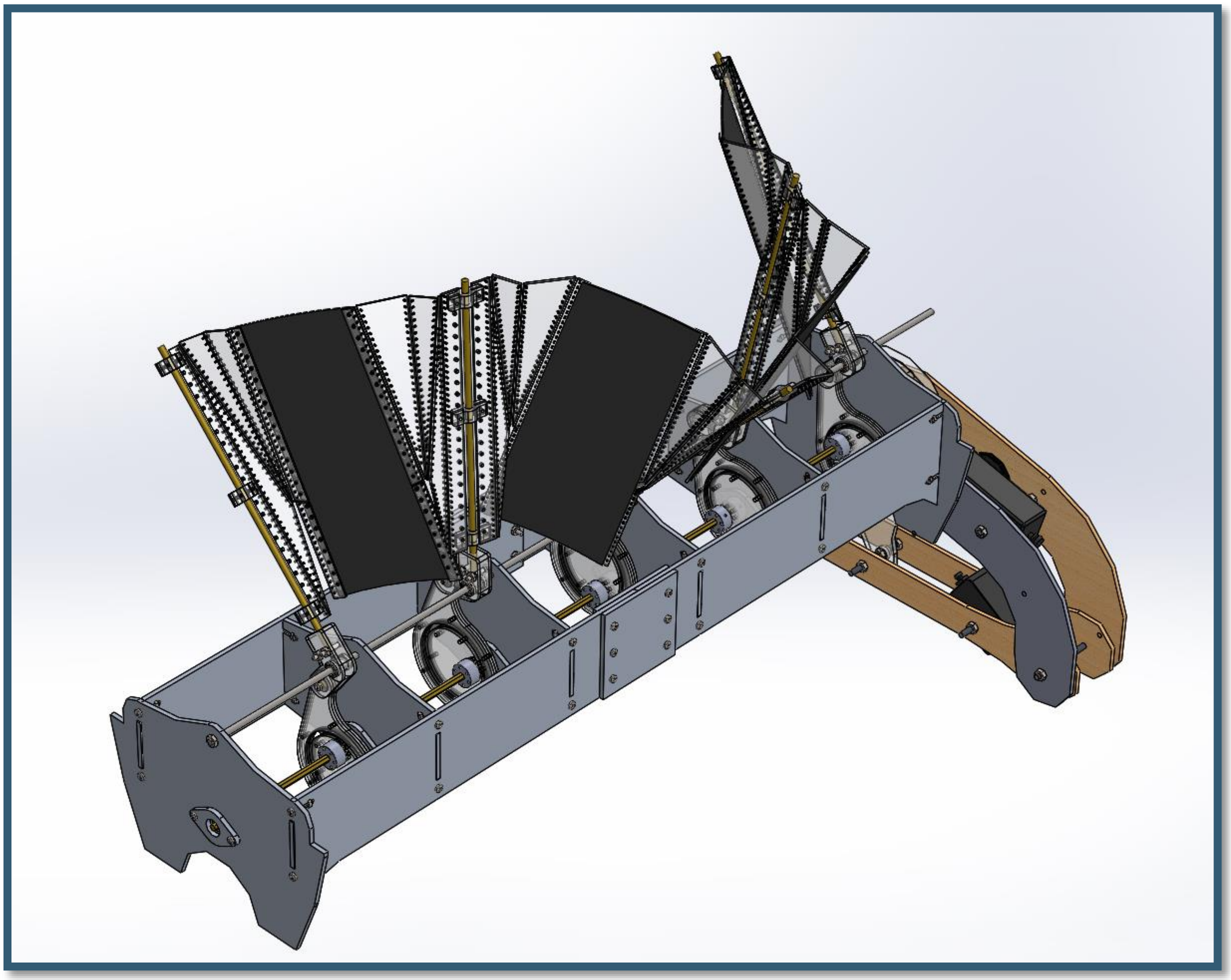

Figure 30: Solid model of the entire assembly.

Manufacturing

At each phase of manufacturing, materials were selected to be cut on a two-dimensional laser cutter. The laser cutter proved to be an invaluable tool, enabling rapid prototyping and accurate tolerances.

Materials

The principal construction materials used were extruded acrylic, plywood, and neoprene sheets due to the ease with which they can be cut with the VLS 4.60 Laser Cutter. A variety of bearings, fasteners, and shaft designs were also used. The full bill of materials is provided below. Note that all dimensions are nominal and provided by the manufacturer. Measured dimensions may vary.

Assembly Feature	**Materials**	**Quantities**
Frame	1. 0.25” Plywood	1. 5.71 Sq. ft.
	2. 1” 8-32 Machine Screws	2. 53
	3. 1.125” OD Ball Bearings	3. 6
Eccentric Cams	1. 0.125” Extruded Clear Acrylic	1. 1.53 Sq. ft.
	2. 0.5” 6-32 Machine Screws	2. 55
	3. 1.75” 6-32 Machine Screws	3. 5
	4. 0.687” Ball Bearings	4. 5
	5. 0.25” Steel Balls	5. 210
Masts	1. 0.25” Brass Rod	1. 65 in
	2. 0.5” Extruded Clear Acrylic	2. 9.55 Sq. in.
	3. 0.687” Ball Bearings	3. 10
Drive Shaft	1. 0.25” Hexagonal Steel Rod	1. 1 x 6 ft.
Pivot Shaft	1. 0.25” Threaded Steel Rod	1. 1 x 6 ft.
Fin	1. 0.0625” Extruded Clear Acrylic	1. 2.02 Sq. ft.
	2. 40 lb. Microfilament Fishing Line	2. 1 spool
	3. 0.0625” Neoprene Rubber Sheet	3. 1.59 Sq. ft.
	4. 3/8 “ ID Plastic Tubing	4. 20 ft.
	5. 0.5” 6/32 Machine Screws	5. 24
Collar	1. 0.5” Extruded Clear Acrylic	1. 6.8 Sq. in.
	2. 6-32 Machine Screws	2. 5

Table 1: Bill of Materials

Most of the mechanism was manufactured from acrylic, while the frame was made from plywood. These materials were chosen for their adequate material properties and inexpensiveness. Brass dowel was chosen for the masts, as it does not corrode and its high yield strength resists flexing. The rest of the hardware was stainless steel for strength and corrosion resistance. Both fin designs relied heavily on the use of neoprene, which was selected because it is strong, flexible, and chemically stable.

Procedure

Rapid prototyping techniques enabled easy fabrication of parts at low cost, which was empowering when testing alternate constructions. The ability to quickly build and assemble designs from parametrically driven models made adjusting designs based on test results feasible. This rapid prototyping method also facilitated prompt confirmation of design decisions and allowed the team to utilize the limited time effectively.

The primary fabrication tool used was a VLS 4.60 Laser Cutter. This enabled fast and precise production of parts from plywood and acrylic sheets. These pieces could then be quickly assembled and calibrated to operate smoothly. This manufacturing process is also relatively inexpensive and allowed for three iterations of the mechanism to be built within time and budgetary constraints. The laser cutter reads vector data from DXF files created from the geometry of the SOLIDWORKS models. This was preferable to aluminum or steel milling, because the process is both time and material intensive.

There are however a few drawbacks to using a laser cutter. The cutting process creates a draft around the perimeter of the parts. Therefore, the team performed several test cuts on each material used to determine the optimal cutting speed and power to minimize the draft angle. This process was particularly important when fabricating parts that had to fit within one another. Additionally, when fabricating the frame, cutting plywood generated a large amount of smoke and charring around the cut edges of the parts. The settings of the laser cutter were adjusted to minimize this effect.

The eccentric was designed to be constructed from three layers of sandwiched 0.125 inch acrylic pieces and held together with 6-32 machine screws. The acrylic profiles were cut using the laser cutter, and the bearing holes were cut using a drill press. To build each cam the first layer of acrylic, consisting of the exterior cam and follower component, was laid on a flat surface with the screws already inserted. The middle layer, consisting of the middle cam and follower component, was then placed. 0.25 inch steel balls were then placed around the interior perimeter of the middle follower piece and resting on the first acrylic piece. The third layer of acrylic was placed on top and nuts were tightened down on each of the screws to hold the layers in place. A steel ball bearing was pressed into the pivot point of the follower. To ensure torsional stability, two 0.5 inch acrylic collars were added to the eccentric to mount it securely to the output shaft. These collars were attached to the eccentric cam with 6-32 machines screws. A 6-32 set screw was used to fix the eccentric assemblies to the output shaft.

Figure 31: Eccentric cam assembly.

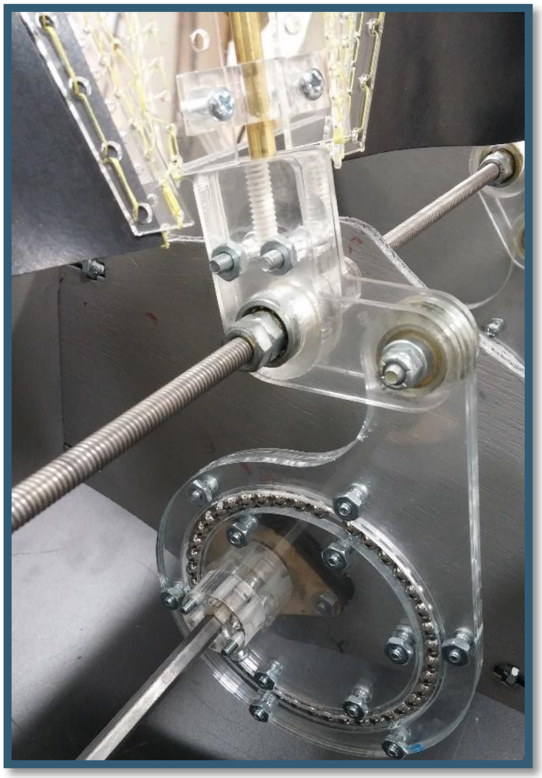

Figure 32: Cam rocker assembly.

The mast rocker was made from a piece of 0.5 inch acrylic and two pieces of 0.125 inch acrylic. The pieces are fastened together with 8-32 machine screws. The mast was fastened to the 0.5 inch acrylic piece using a 1/4-20 threaded hole. Steel ball bearings were press fit into the 0.125 inch acrylic pieces to provide support on the pivot shaft and to minimize the friction of the system.

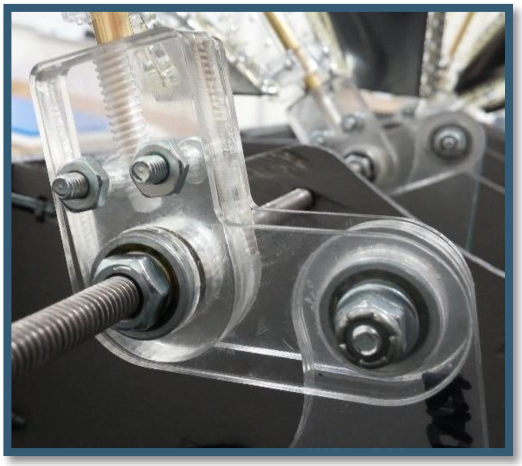

Figure 33: Mast-rocker assembly.

The neoprene fins were made from 0.0625 inch neoprene rubber sheets and polyethylene tubing. The fins were cut in sections using the laser cutter with DXFs derived from the fin geometry calculations. Polyethylene tubing was placed in the lap joints between fin sections with one inch of bonded neoprene on either side. The lap joints were formed using rubber cement and hot glue.

The hybrid fin was constructed with neoprene and acrylic plates. The acrylic plates and neoprene sections were cut using the laser cutter and then sewn together with 40lb microfilament. To attach the fin sections to the masts, clips were cut from 0.5 inch acrylic and fastened to each section using 6-32 machine screws. These clips were then slid over the masts, and held in place with 1/4-20 nuts threaded onto the ends of the masts.

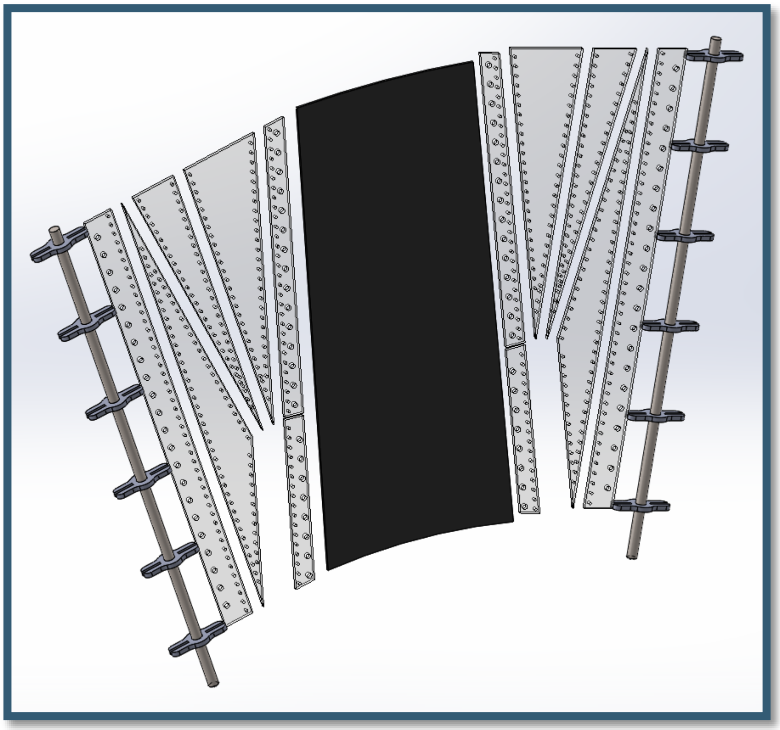

Figure 34: Exploded view of one segment of the hybrid fin assembly.

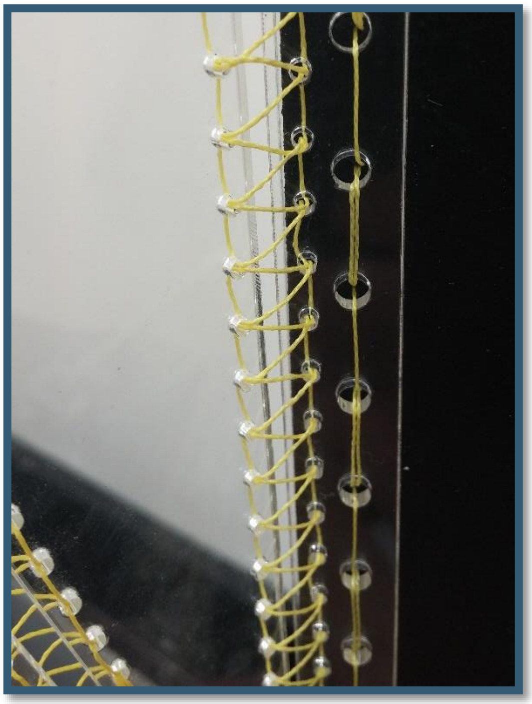

Figure 35: Detail view of seams on the hybrid fin.

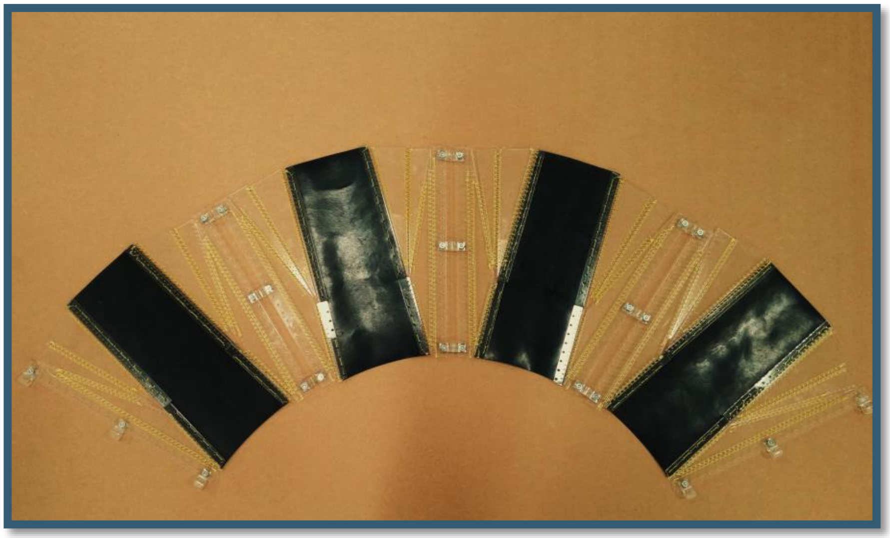

Figure 36: Full hybrid fin.

The frame was constructed from laser cut 0.2 inch plywood and 8-32 machine screws. Individual sections of the frame were cut and pressed together, fastened by 8-32 machine screws, which fit in grooves cut into the profiles of the frame. The frame was painted to help protect the wood from the water.

Testing

The testing process followed the steps delineated in the chart below. The procedure was developed to facilitate flexibility in which independent variables were tested during an individual testing session while maintaining a consistent methodology for our set up and interactions with the testing environment. The testing environment, test rig design, variables, and specific procedures for testing each variable are provided in the following sections.

Testing Procedure

1. Install test rig in rowing tank
2. Mount device on rig
3. Mount dynamometer on rear end of device
4. Install the flow-meter, rotary sensor, and dual-force sensor
5. Start LoggerPro
6. Start rowing tank
7. Run bottle flow test
8. Begin recording measurements
9. Increase flow speed gradually by increments of 100 (.1 m/s)
10. Make observations and measurements
11. Turn off rowing tank and wait for device to come to a stop
12. Remove device from the tank
13. Disassemble test rig

Environment

Two separate testing facilities were used for the testing of our various designs. For the second iteration of the design, a flow tank in Higgins Laboratories, equipped to provide exact flow velocities up to 5.6 m/s, was used. However, the channel was too narrow to create sufficient pressure on either side of the fin to drive the mechanism, which prevented the fin from moving. The Donahue Rowing Center located in WPI's Sports and Recreation Center provided a sufficiently large testing environment with variable flow speeds. Precise flow speeds were unknown and unspecified by documentation provided by the manufacturer of the rowing tank. Therefore it was necessary to manually measure the flows generated at different speed settings in order to calibrate the tank. Use of the tank required careful consideration to prevent damage to the equipment and facility. To do so, a testing rig was constructed. The methodology for the velocity testing and the design of the testing rig are described below.

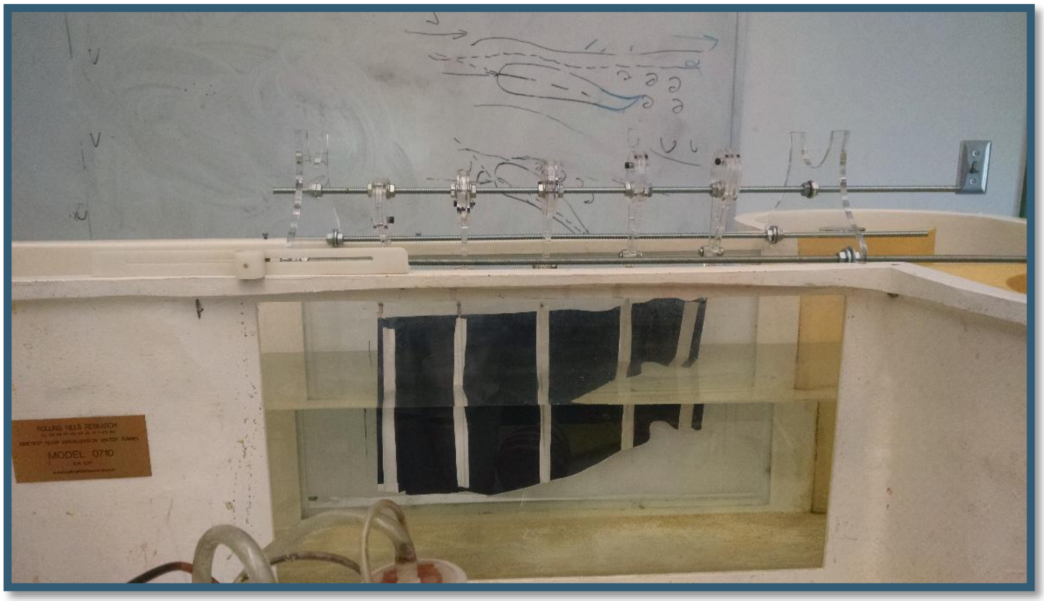

Figure 37: Second prototype iteration in the Higgins Laboratories flow tank.

Figure 38: Device with hybrid fin in Donahue Rowing Center tank.

Before the final design and dimensions for the Ribbon Fin were determined, it was necessary to accurately measure the dimensions of the rowing tank to establish the maximum size of our prototype. The depth of the tank at its deepest accessible point became a driving dimension for the design of the Ribbon Fin. Measurements of the tank were taken using a 25 foot tape measure, crucial dimensions are provided in the table below.

Dimension	
Length (L)	47 ft
Depth of water at L=0 ft (D_1)	14.75 in
Depth of water at L=25 ft (D_2)	13.00 in
Depth of water at L=47 ft (D_3)	11.00 in
Width of water filled section (W)	89.5 in
Width of tank with ledge (W_L)	100 in
Width of flat tank bottom (W_{FB})	44 in
Height of narrow ledge from bottom at L=0 ft (H_{NL})	25 in
Width of narrow ledge (W_{NL})	1.00 in
Total Height with Plexiglass (H)	52.5 in

Table 2: Dimensions of the Donahue Rowing Center tank, as measured.

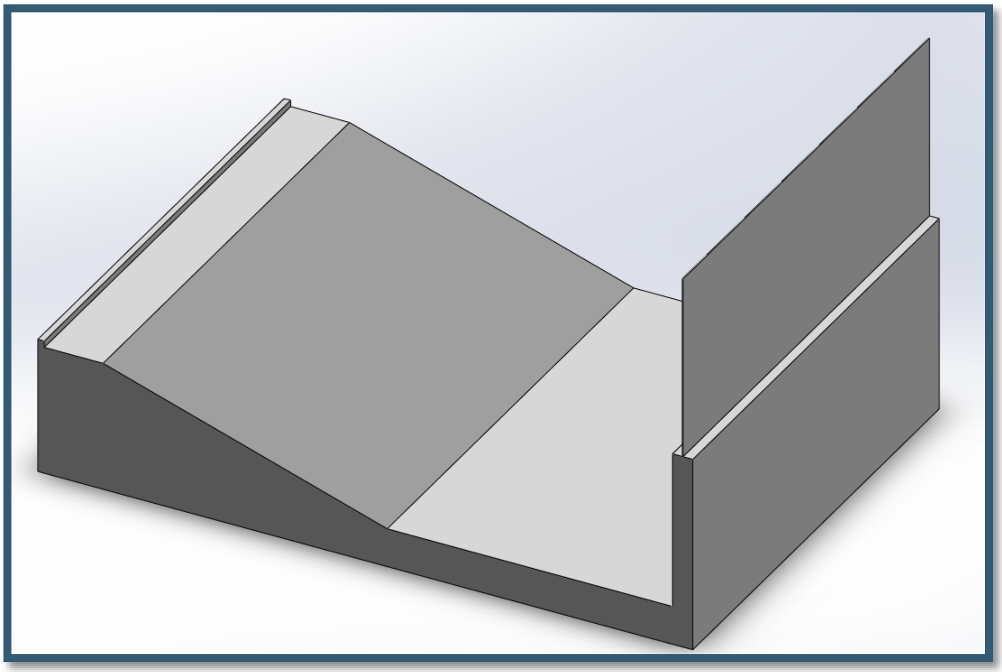

Figure 39: Cross-section of rowing tank showing the profile of the bottom of the tank.

Test Tank Calibration

Before testing could commence, the tank settings had to be calibrated. The team used a Vernier Flow Meter and Logger Pro software package to measure the velocity of the water at different speed settings. The tank machinery has arbitrary speed settings ranging from 0 (off) to 2000 (full). Velocity measurements were taken at increments of 100 speed units. Through this study it was determined that control system of the flow tank was measured in millimeters per second. It should be understood that the tank control gauge is likely the average velocity, and does not necessarily represent an accurate flow speed for any particular point in the tank.

During the testing process it was determined that the flow meter would not hold calibration. This was likely due to aging components in the sensor. This combined with the inconsistency of the gauge made it impossible to have an accurate measurement of the flow velocity. Therefore, an additional method of flow measurement was needed. To accomplish this, a 25 foot (7.62 meter) distance was marked in the tank using a strip of duct tape and a water bottle was dropped into the flow. The time it took for the bottle to travel the 25 feet was measured in seconds and the velocity was calculated and recorded for each test. This bottle test became the primary method of measuring the velocity of the flow.

Test Rig Design

The test rig was designed to meet two main criteria: suspend the mechanism over the surface of the water, and protect the rowing tank from damage due to any accidents that occur during testing. To meet the first criterion, the test rig had to hold the chassis in one position above the surface of the water while keeping the ribbon fin submerged in the flow. To achieve this positioning the rig was designed to span the width of the channel, laying parallel to the surface of the water. Resting one end of the rig on the pool deck, and the other on a ledge opposite the deck allowed for every component of the test rig and the model aside from the fin to be held above the water.

Meeting the second design criterion meant ensuring that any piece of hardware that falls from the mechanism does not enter the pump system of the rowing tank, which could cause severe damage. To accomplish this, the team used a net made from window screen mesh and a heavy steel chain. The screen was wrapped around the chain, which was then submerged to the bottom of the tank. The screen was hung at the rear of the tank in front of the outlet.

Additional considerations for the design were weight, cost, portability, and functionality. It was crucial that the test rig fully support the Ribbon Fin assembly and testing equipment. It was also necessary that it be easy to transport to and from the tank facility, and that it be easily assembled and disassembled at the tank as tank access was limited. Wood and steel brackets were chosen as primary construction materials due to their availability, low cost, and ease of assembly.

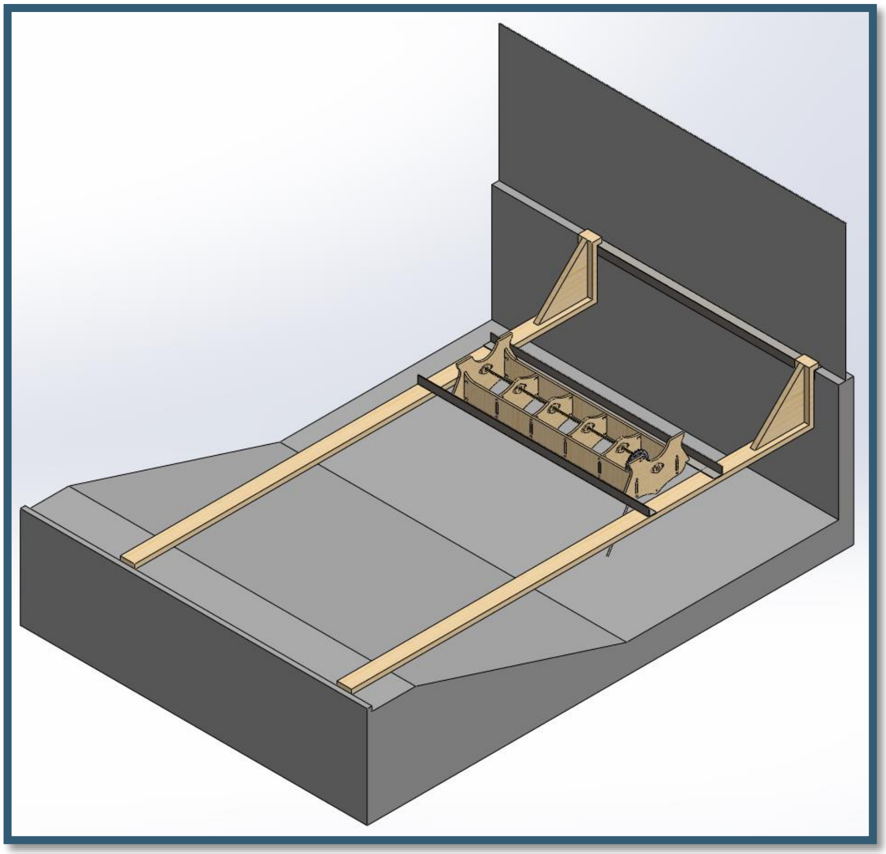

Figure 40: Test rig model with ribbon fin assembly. Positioned in the tank as intended for testing.

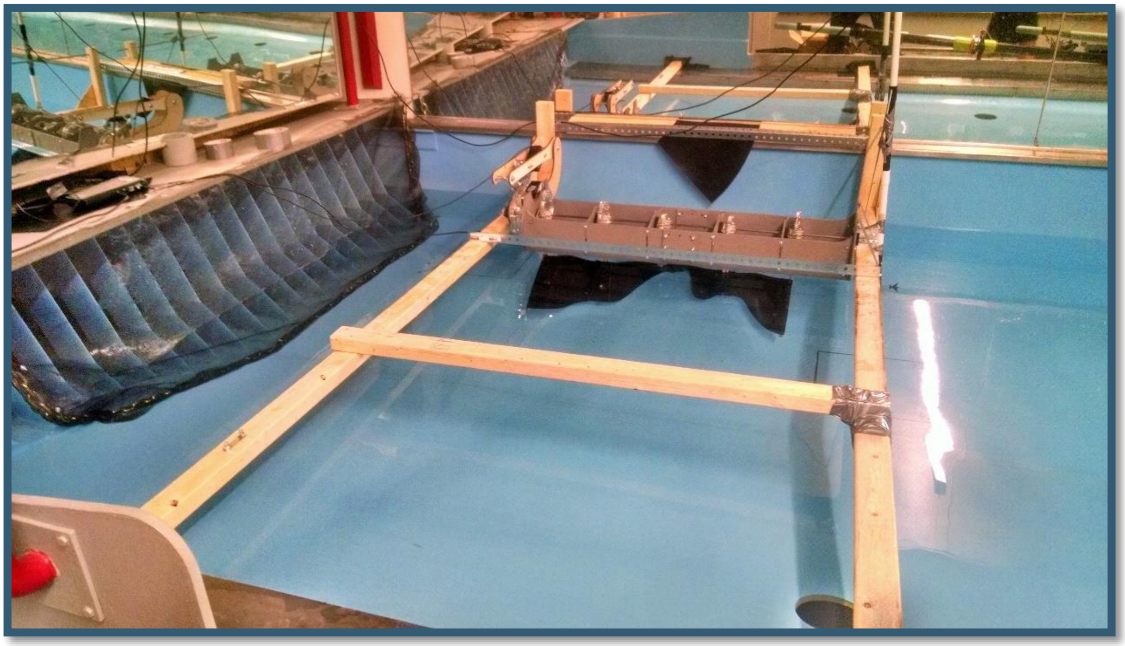

Figure 41: Test rig and testing setup in Donahue Rowing Center tank.

Variables

Independent Variables

To get a clear indication of performance the team manipulated several characteristics of the testing rig, the device, and the testing environment. The independent variables, the materials needed to measure or create them, the procedure for measurement, and the justification for each variable is provided in the table below.

Variable	**Materials Used**	**Procedure**	**Justification**
Torque	Dynamometer with dual-force sensor and rotary sensor attachments.	The torque on the shaft was adjusted by adding or removing mass at the end of a lever arm. This lever applies frictional forces to a 6 inch diameter wheel attached to the drive shaft.	Varying the torque represents different loads attached to the shaft, such as a pump or an electrical generator. The goal of testing the device at varying torques is to find the upper and lower ranges of operation for our prototype.
Flow Velocity	Vernier Flow Meter, Logger Pro software, Water Bottle.	Flow velocity was varied at increments of 100 velocity units. Velocities were approximate and verified using the bottle test.	Varying the velocity of flow allowed us to test the functionality of the mechanism under different conditions in order to create a power curve over the range of operation.
Fin Configuration	Fin 1: Composite Fin made of acrylic plates and neoprene. Fin 2: Fin made of neoprene only.	Fins were swapped and mechanism performance was tested once optimal wavelength was determined, to reduce material use and manufacturing time. Fin 1 was tested first followed by Fin 2.	Altering the fin design allowed us to determine if a stiffer fin or a more flexible fin would be more desirable. Power output was expected to change with different fin designs.
Fin Height	Neoprene only fins at heights from base of: Fin 2: 12 inches Fin 3: 8 inches Fin 4: 4 inches	The height of the neoprene fin was adjusted from 12 inches down to 4 inches at the optimal wavelength.	Fin height was adjusted to determine the impact of fin height on the power output of the mechanism. Initial calculations showed fin height to be a driving factor.

Table 3: Independent Variables

Dependent Variables

The sole dependent variable that was measured was rotations per minute (RPM) of the output shaft. This variable is the most indicative of mechanism performance as it is directly related to power output when combined with applied torque. RPM was measured using the Vernier rotation sensor, which gave instantaneous measurements of the shaft rotation in radians per second.

Results and Analysis

For each iteration of the ribbon fin, torque-speed curves and flow speed vs RPM graphs were produced. Through analysis of these graphs, the aspects of the design that had the most significant effect on performance were determined. The data also provided insight into the potential of the device as a method of power generation.

Torque-speed curves serve to evaluate the capacity of the device and its power output characteristics. This relationship can be used as a metric to accurately compare the device to other power generators. Additionally, torque speed curves can be compared against rated loads from pumps or generators to determine how to best extract power from the rotation of the output shaft. Torque speed curves take the form of a line connecting the stall torque with the speed of the unloaded shaft. Shaft power is defined by the product of torque and shaft speed, therefore a power-speed curve can be calculated with the following equation. The power curve shows how the shaft can be optimally loaded to output its maximum power. Power (P) is a function of torque (τ), and angular velocity (ω).

$$P = \tau * \omega$$

Graphs to compare flow speed and shaft RPM were also produced. These plots illustrated the proportionality between the angular rate of the shaft and the flow speed of the water. The angular rate of the shaft is directly proportional to the wave speed along the fin, which must be slower than the free stream flow velocity. Through conversion of the angular rate of the shaft to phase velocity of the fin, the velocity that best extracts power from the stream can be determined.

With these data sets, efficiency analyses were made. This was done by normalizing the output power of the device with respect to the power contained in the flow. These analyses resulted in graphs that can be used to compare the mechanism to other forms of power generation.

Four iterations of the ribbon fin were tested: the 12 inch hybrid fin, the 12 inch neoprene fin, the 8 inch neoprene fin, and the 4 inch neoprene fin. All tests were performed with a fin wavelength of 28.8 inches, which provided the closest approximation of a single wave cycle being expressed on the fin with 75 degrees of angular displacement between each mast, for a total of 375 degrees of rotation. Although the device was designed in such a way that would allow for the testing of different fin wavelengths, time constraints prevented such tests.

Testing Results

A large amount of data was collected. With hundreds of samples being taken over the course of testing, the effects of noise in the readings was compounded and became a significant detriment to the results. The data needed to be efficiently and effectively organized and compiled into a format that best represented the results observed, to lay a solid foundation for future testing.

The sensors used were developed by Vernier Software and Technology. The Logger Pro data collection program was used to collect and store data from the Vernier sensors. Samples were taken at three samples per second, with a typical data collection period of one minute. Logger Pro data analysis tools are limited; therefore the data was exported from Logger Pro into CSV files.

The data collected was analyzed using MATLAB, which provides a number of tools to effectively create meaningful graphs from large data files created by sensors. These tools help filter out noise and outliers to provide a good visual representation of the physical phenomena.

Three major graph sets were plotted to describe what was observed during testing: shaft speed verses flow speed, shaft speed versus torque, and power versus torque. These plots were then analyzed to determine wave speed and efficiency metrics.

The shaft speed-flow speed relationship was fairly easy to define. The averages were taken of the collected angular velocity data. Each average became a singular data point related to a specific flow velocity.

Torque-power speed curves were more complicated as they were constructed from calculations performed on the collected data. The force measured by the dual force sensor was multiplied by the radius of the output wheel to obtain the torque of the mechanism. The torque was then related to the angular velocity of the shaft to get power. The torque (τ) was calculated by multiplying the measured force applied (F) and the radius of the dynamometer wheel (r), which was 3 inches.

$$\tau = F \times r$$

Procedure for Generating RPM vs Flow Speed:

1. Import angular velocity (ω) and flow speed data from CSV files into MATLAB
2. Angular velocity was averaged.
    a. $\omega_{avg} = \frac{\sum \omega_{measured}}{samples}$
    b. Standard deviation was determined using the standard deviation function, std(A), in MATLAB.
3. ω_{avg} was then plotted against specific flow speeds
    a. scatter(flowspeed, ω_{avg})
4. Best fit was applied to the scatter plot using the polyfit and polyval functions in MATLAB.

Procedure for Generating Torque Speed Curve:

1. Import force and angular velocity data from CSV files into MATLAB.
2. Torque determined from force sensors and radius of dynamometer wheel (3 inches)
    a. $\tau = F \times r$
3. Power is determined from Torque and ω
    a. $P = \tau * \omega$
4. Generate Plots

   a. scatter(τ,ω)
   b. scatter(τ,power)

5. Best fit curves applied using the polyfit and polyval functions in MATLAB.

For further information about MATLAB scripts refer to Appendix E. To best present the data that was collected most of the plots were of best fit lines. To see best fit lines in relation to original scatterplots, refer to Appendix D.

Due to the nature of our sensor design, and the testing rig itself, significant vibration was introduced into the system. This caused a lot of noise in the data sets. As explained in the future considerations section, use of tools like an inductive generator and better damping of the rig would improve data collection.

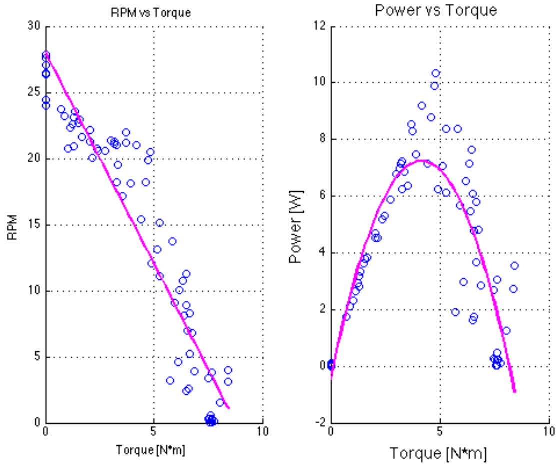

Figure 42: Example of decent curve fitting.

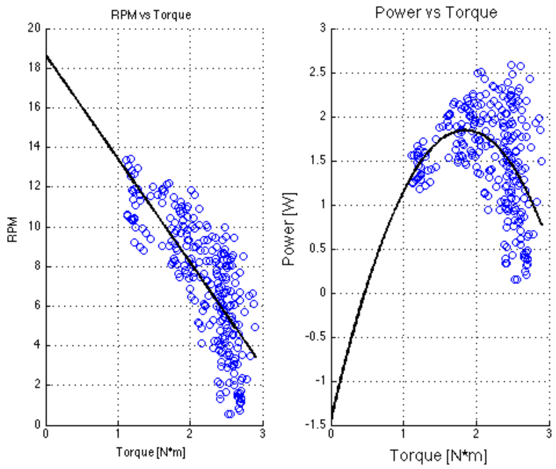

Figure 43: Example of a curve fit with more error.

The graphs above represent two different data sets, one where the curve fitting has a high degree of correlation to the data point scatter plot, and another where this is not the case. To manage noise, polynomial curve fitting was applied to the data points to describe the general behavior of how power and shaft speed relate to various loads. It should be noted that these polynomial curves show the general trend of the data. They do not describe the extreme points measured by the sensors. The figures above demonstrate the variability of best fit lines when using noisy data sets. Scatter plots for all data sets are provided in Appendix D.

Hybrid Fin

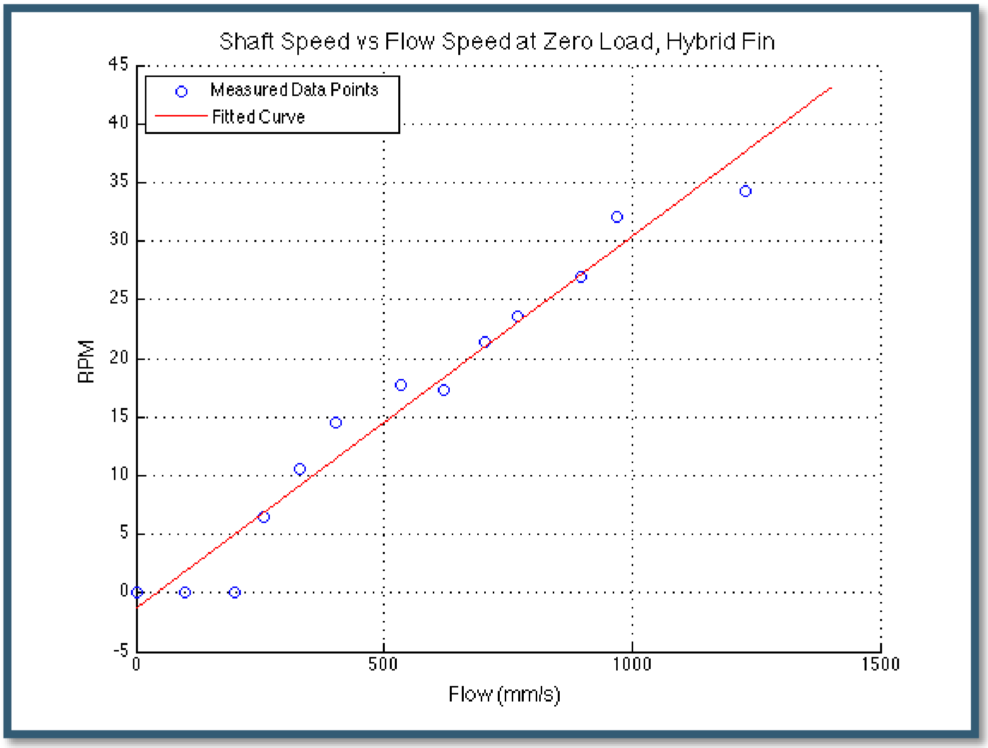

Figure 44: Shaft Speed versus Flow Speed at zero load for hybrid fin.

The graph above describes the relation between the velocity of the water in millimeters per second and the rotation of the output shaft in rotations per minute. The minimum shaft speed was 0 rpm at flow speeds between 0 and 200 mm/s. The maximum shaft speed was approximately 35 rpm at a flow speed of 1230 mm/s. The cut-in speed was between 200 and 300 mm/s. The line of best fit for this data is given by the equation:

$$RPM = 0.0317x - 1.336$$

The graphs presented on the following page illustrate the relation between applied torques in Newton-meters and the rotation of the output shaft in rotations per minute, along with the applied torques and the power output. The curves represent the best-fit for each data set. At the lowest operational speed the maximum applied torque was approximately 2 N*m. At the highest flow speed tested (1230 mm/s), the maximum applied torque before stall was approximately 11 N*m, it should be noted that this was slightly exceeded by the torque achieved at a flow speed of 970 mm/s. The maximum power output did not coincide with the maximum applied torque. Instead, the power output was maximized with approximately 6 N*m of applied torque. This generated a power output of approximately 14 watts when the flow speed was 1230 mm/s.

The mean standard deviation for the angular velocity versus flow speed graph is 0.0195 rad/sec.

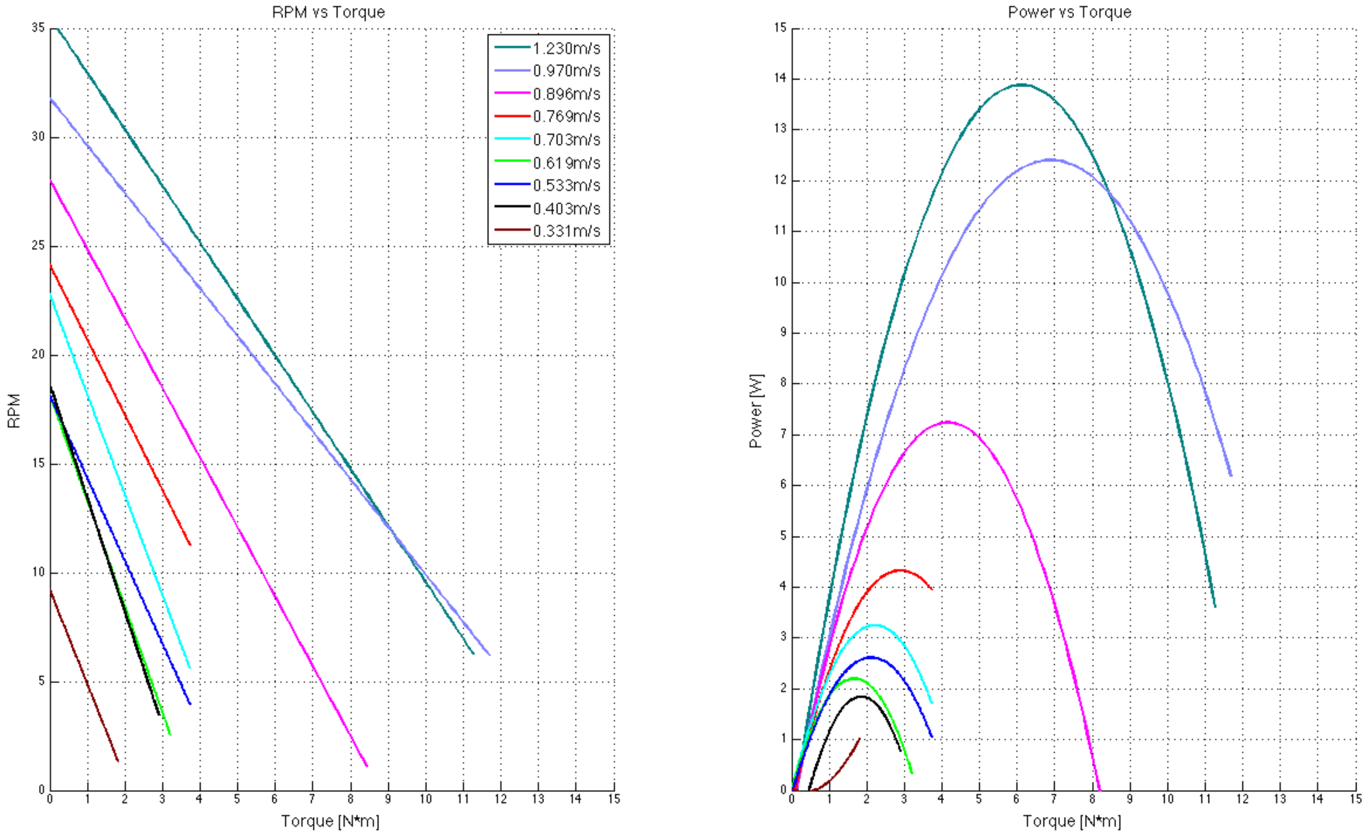

Figure 45: Torque Speed and Power Curves for hybrid fin.

Neoprene Fin- 12 inches

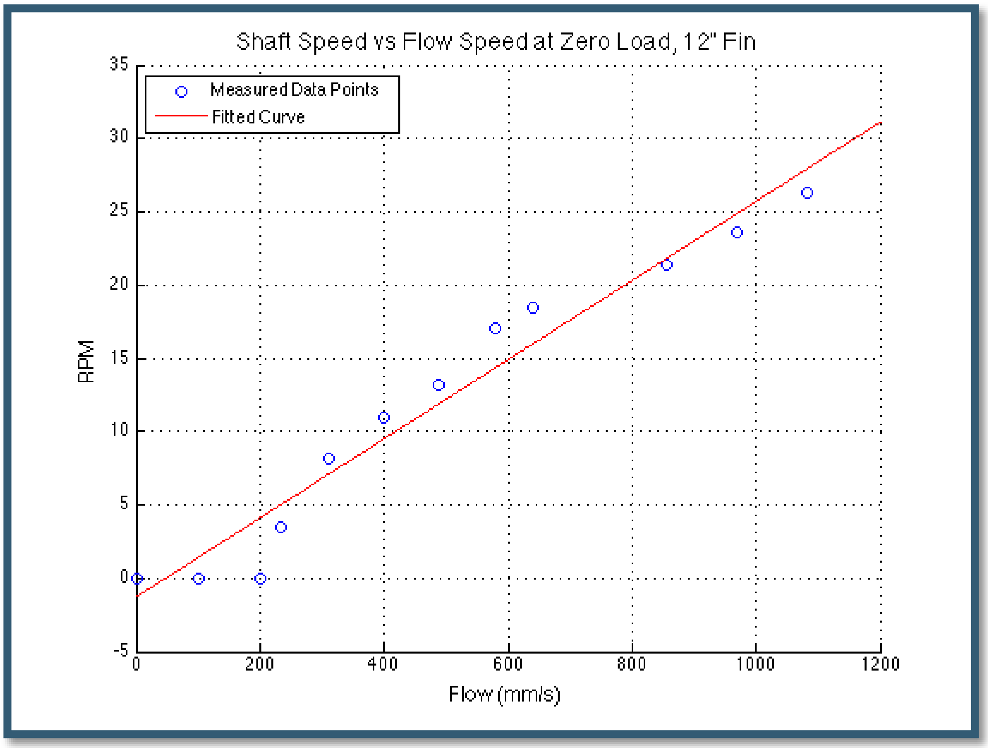

Figure 46: Shaft Speed versus Flow Speed at zero load for 12 inch neoprene fin.

The graph above describes the relation between the velocity of the water in millimeters per second and the rotation of the output shaft in rotations per minute. The minimum RPM was 0 rpm at flow speeds between 0 and 200 mm/s. The maximum RPM was approximately 27 rpm at a flow speed of 1080 mm/s. The cut-in speed was between 200 and 250 mm/s. The line of best fit for this data is given by the equation:

$$RPM = 0.02699x - 1.302$$

The graphs presented on the following page illustrate the relation between applied torques in Newton-meters and the rotation of the output shaft in rotations per minute, along with the applied torques and the power output. The curves represent the best-fit for each data set. At the lowest operational speed the maximum applied torque was approximately 1 N*m. At the highest speed tested (1080 mm/s), the maximum applied torque before stall was approximately 11 N*m, it should be noted that this was exceeded by the torque of 14 N*m achieved at a flow speed of 969 mm/s. The maximum power output did not coincide with the maximum applied torque. Instead, the power output was maximized with approximately 10 N*m of applied torque. This generated a power output of approximately 11 Watts when the flow speed was 969 mm/s.

The mean standard deviation for the angular velocity versus flow speed graph is 0.0801 rad/sec.

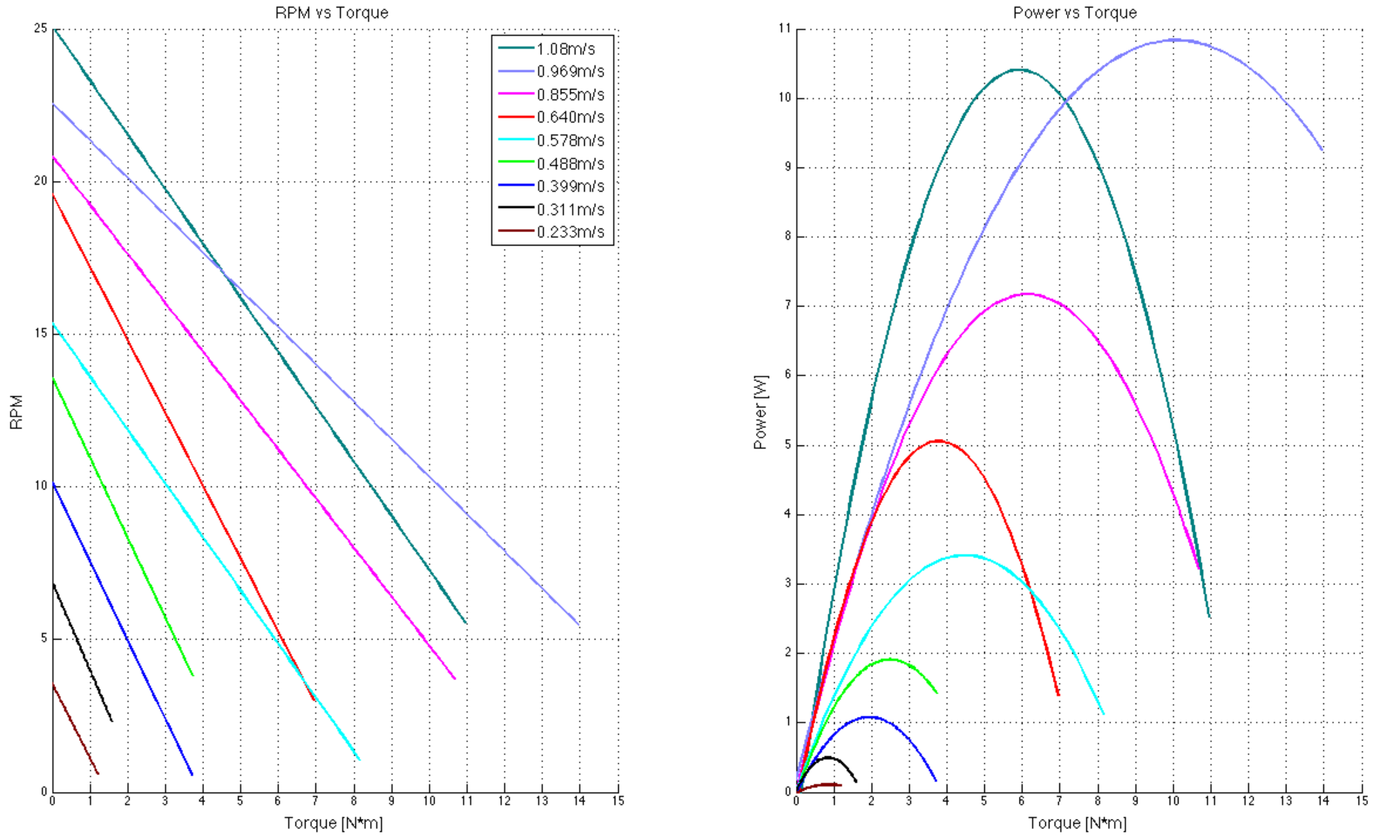

Figure 47: Torque Speed and Power Curves for 12 inch neoprene fin.

Neoprene Fin- 8 inches

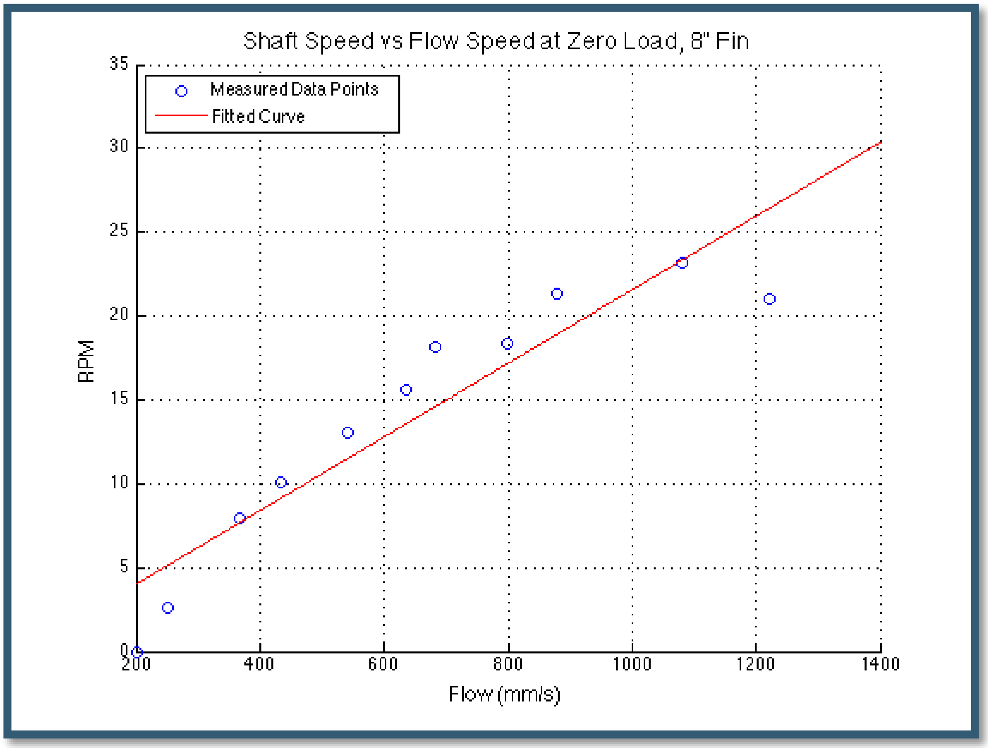

Figure 48: Shaft Speed versus Flow Speed at zero load for 8 inch neoprene fin.

The graph above describes the relation between the velocity of the water in millimeters per second and the rotation of the output shaft in rotations per minute. The minimum shaft speed was 0 rpm at flow speeds between 0 and 200 mm/s. The maximum shaft speed was approximately 23 rpm at a flow speed of 1080 mm/s. The cut-in speed was between 200 and 300 mm/s. The line of best fit for this data is given by the equation:

$$RPM = 0.02196x - 0.3964$$

The graphs presented on the following page illustrate the relation between applied torques in Newton-meters and the rotation of the output shaft in rotations per minute, along with the applied torques and the power output. The curves represent the best-fit for each data set. At the lowest operational speed the maximum applied torque was approximately 1 N*m. At the highest speed tested (1080 mm/s), the maximum applied torque before stall was approximately 6 N*m. The maximum power output did not coincide with the maximum applied torque. Instead, the power output was maximized with approximately 2.5 N*m of applied torque. This generated a power output of approximately 3.5 Watts when the flow speed was 880 mm/s.

The mean standard deviation for the angular velocity versus flow speed graph is 0.2253 rad/sec.

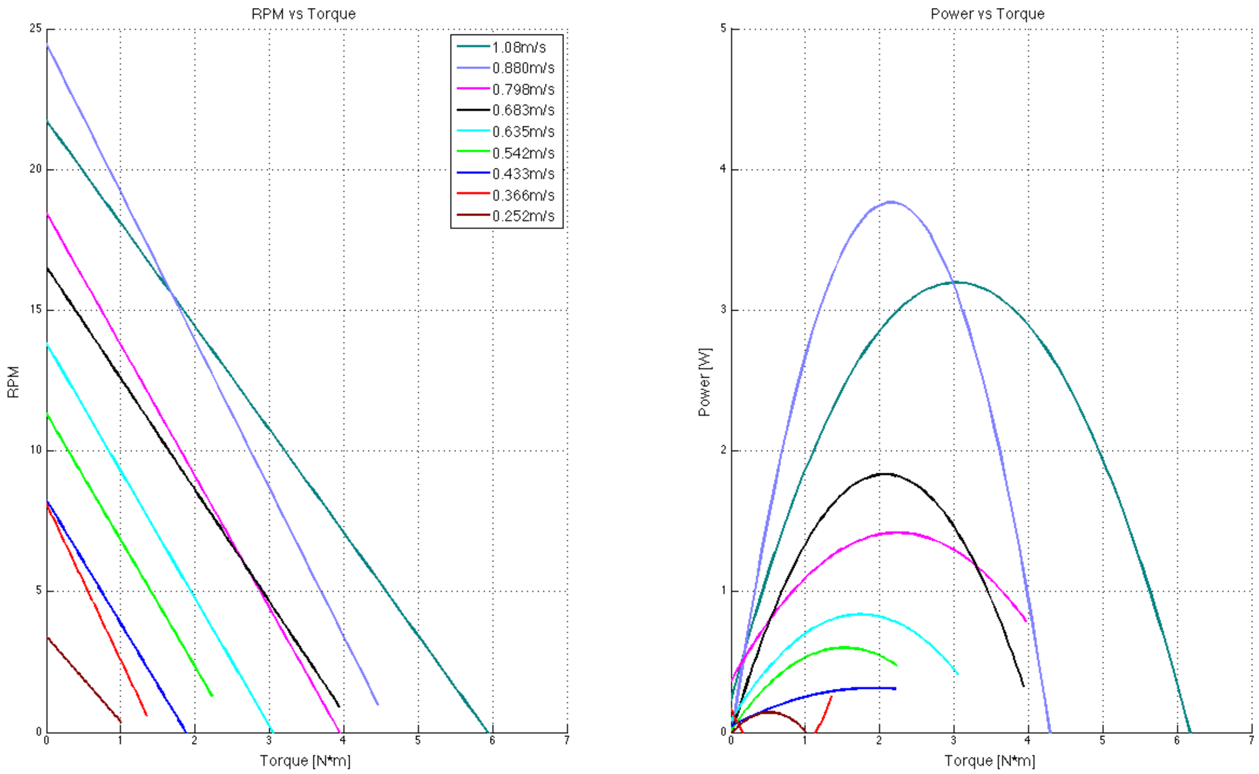

Figure 49: Torque Speed and Power Curves for 8 inch neoprene fin.

Neoprene Fin- 4 inches

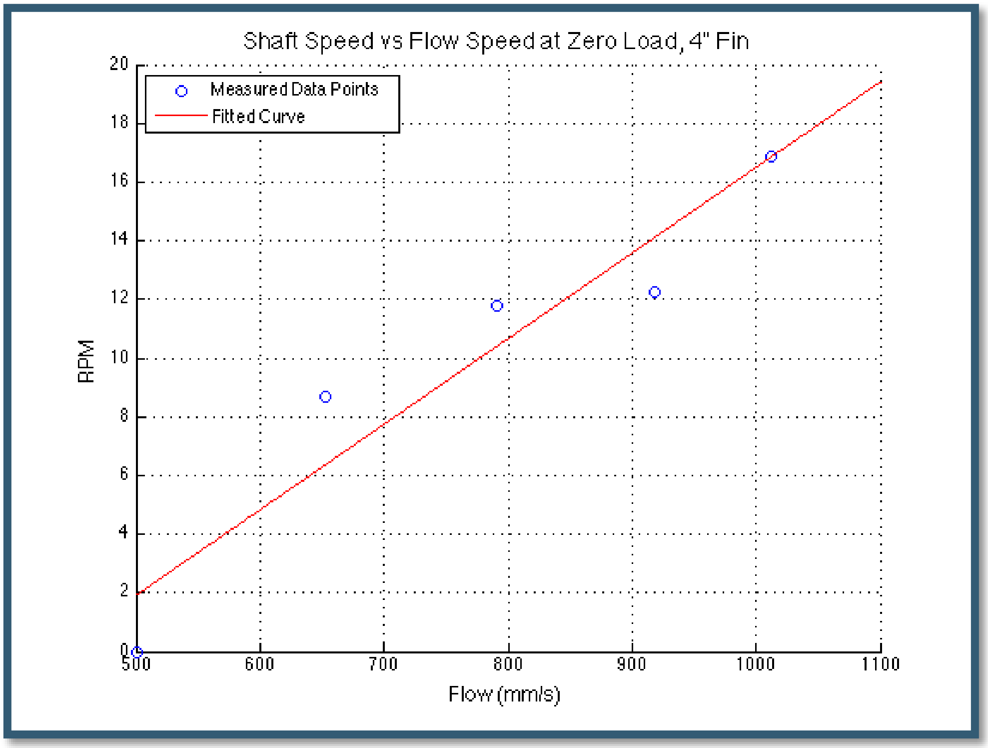

Figure 50: Shaft Speed versus Flow Speed at zero load for 4 inch neoprene fin.

The graph above describes the relation between the velocity of the water in millimeters per second and the rotation of the output shaft in rotations per minute. The minimum shaft speed was 0 rpm at flow speeds between 0 and 500 mm/s. The maximum shaft speed was approximately 17 rpm at a flow speed of 1012 mm/s. The cut-in speed was between 500 and 700 mm/s. The line of best fit for this data is given by the equation:

$$RPM = 0.02917x - 12.68$$

The graph presented on the following page illustrates the relation between applied torques in Newton-meters and the rotation of the output shaft in rotations per minute. The curves represent the best-fit for each data set. At the lowest operational speed the maximum applied torque was approximately 1.2 N*m. At the highest speed tested (1012 mm/s), the maximum applied torque before stall was approximately 1.4 N*m. Reliable power curves were not able to be generated due to limited, poor quality data. The small surface area of this fin poorly extracted power from the flow and had difficulty driving cams through their lock points, leading to the poor data.

The mean standard deviation for the angular velocity versus flow speed graph is 0.2323 rad/sec.

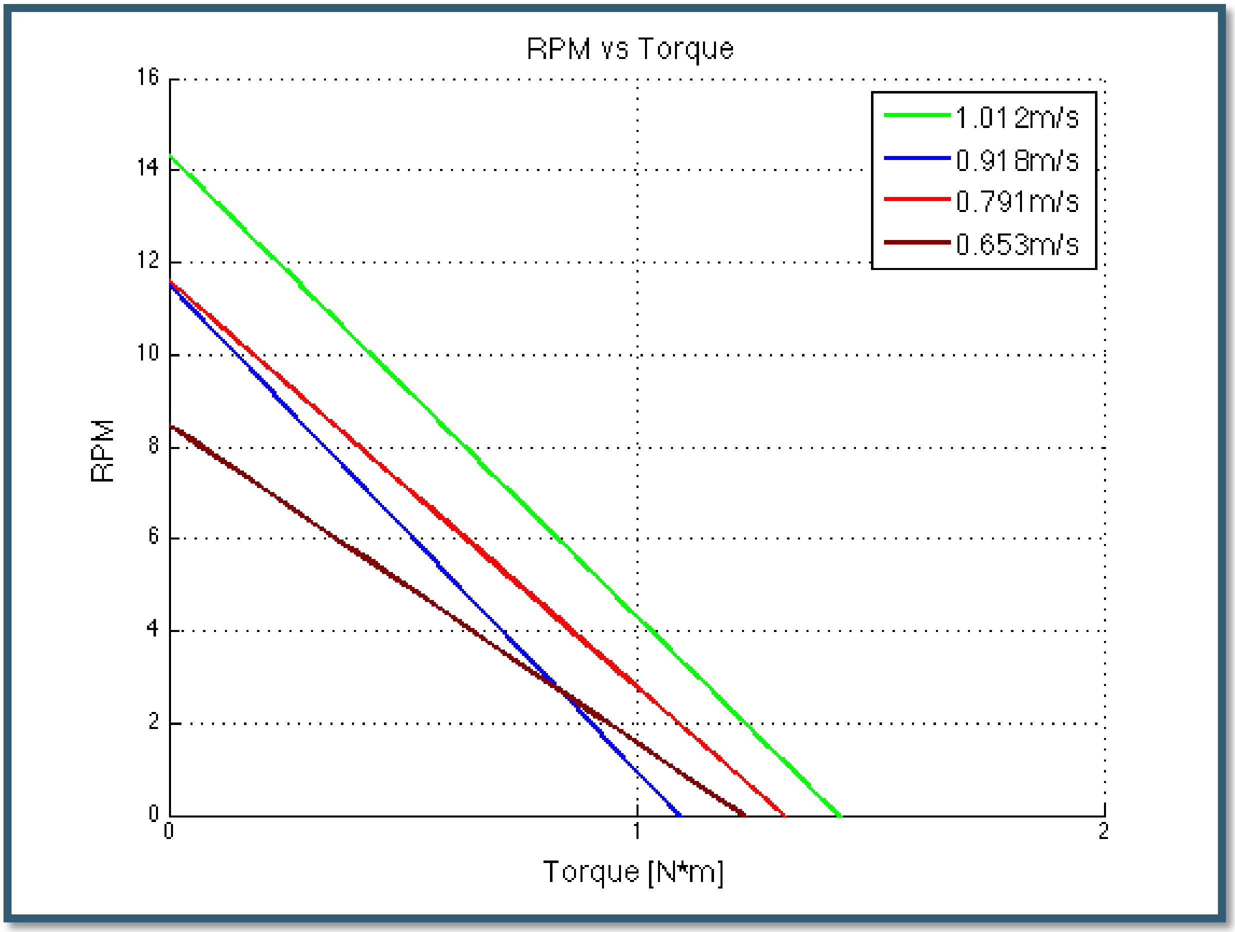

Figure 51: Torque Speed curve for 4 inch neoprene fin.

Analysis

In this section an in-depth discussion and analysis will be presented related to: mechanism efficiencies, interpretation of quantitative results, qualitative observations, and areas for further work and research.

Analysis of Quantitative Results

Wave Speed Optimization

A key metric for assessing the performance of the fin is the ratio of the speed at which the wave propagates along the fin to the flow speed. When the shaft speed that produces the maximum power at a given flow rate is converted to wave speed along the fin using the wavelength and angular frequency, it illustrates the speed at which the traveling wave best retards the flow of water through the control volume. If the power takeoff is under-loaded, the wave on the fin will coast with the flow and although it will travel faster with respect to the flow speed it will be extracting less power. If the power takeoff is overloaded, the wave on the fin will travel slowly with respect to the flow but the pressure of water impinging upon the fin will be large, corresponding to the large torque produced on the shaft.

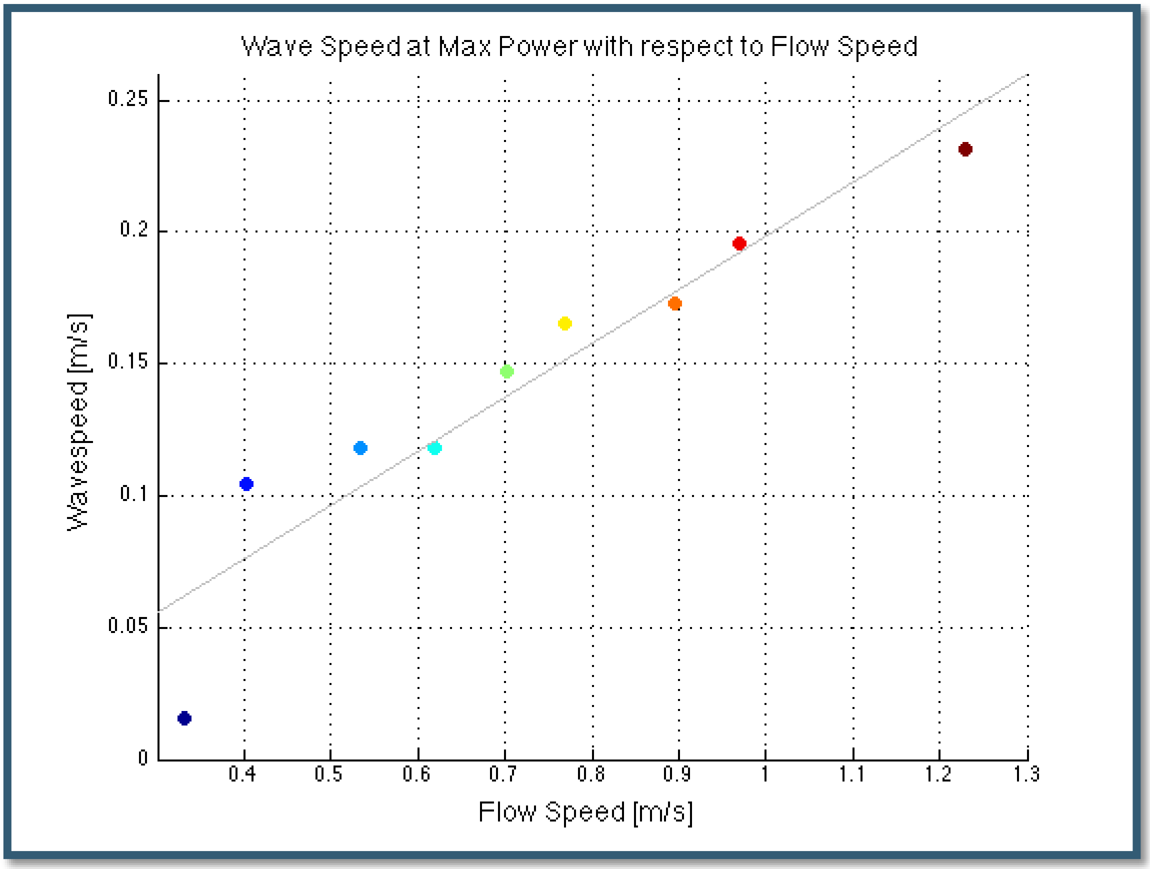

Figure 52: Wave speed at maximum power with respect to flow speed, for hybrid fin.

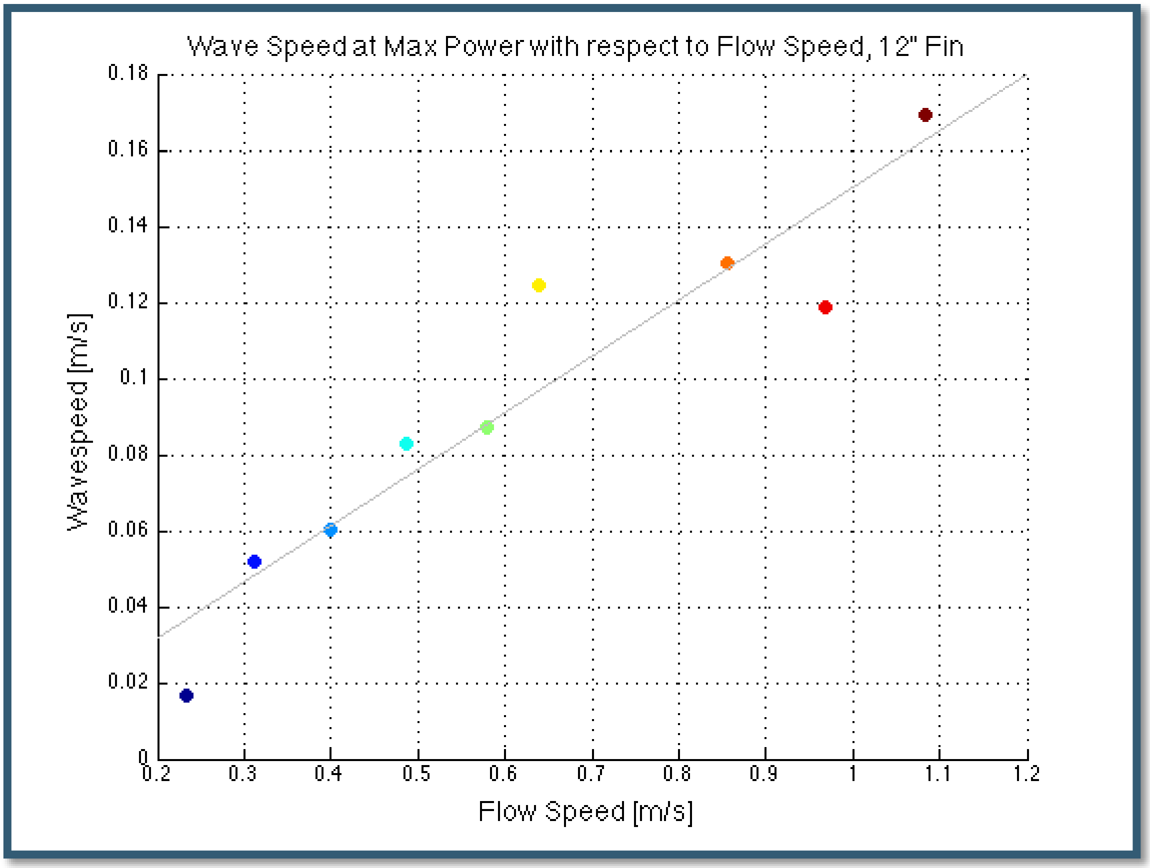

Figure 53: Wave speed at maximum power with respect to flow speed, for 12 inch neoprene fin.

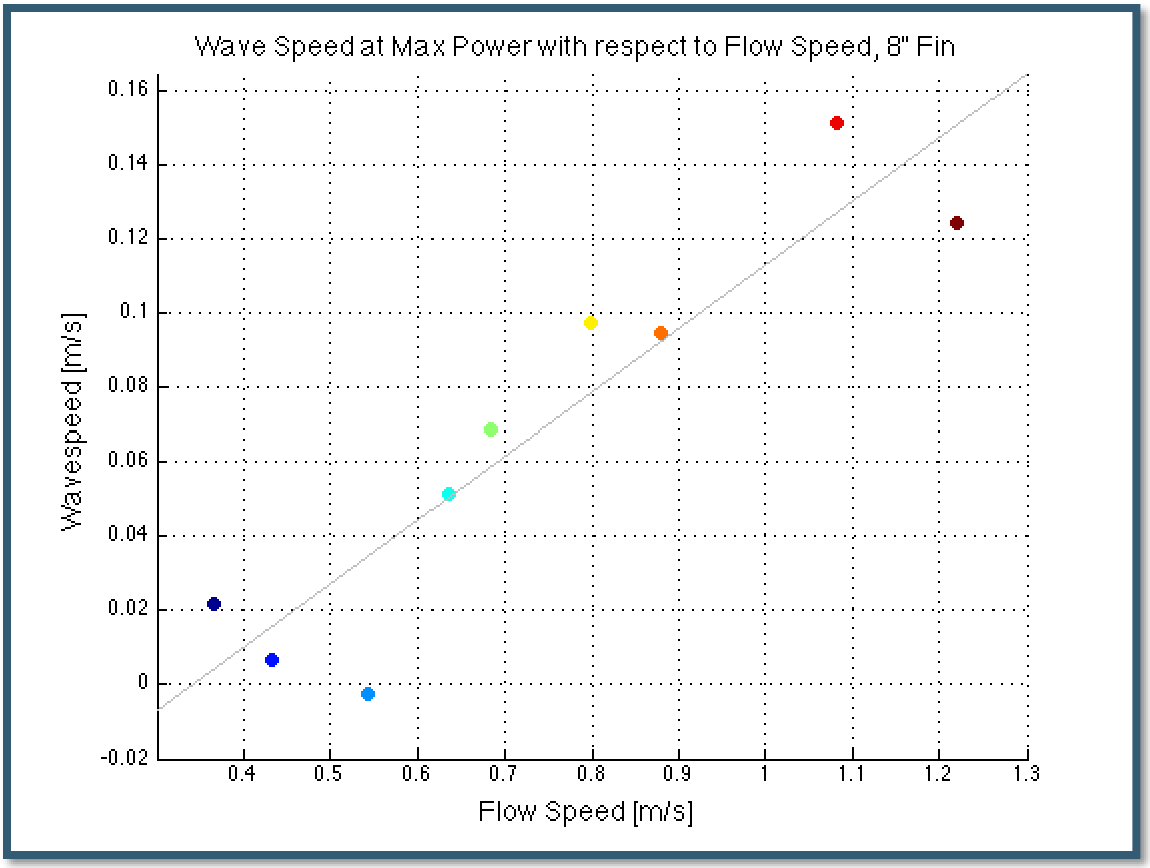

Figure 54: Wave speed at maximum power with respect to flow speed, for 8 inch fin.

The above figures can be used to compare the fluidic behavior of the different fins. The apparent linearity suggests that there is a consistent optimum ratio of wave speed to flow speed at this wavelength. In each fin iteration tested this ratio was consistently around 0.15. Therefore, for any fin exhibiting the overall length and wavelength used here the optimum speed for the wave to propagate will be around 15% of the flow speed. This will be important for evaluating any physical models of this system, as it gives a dimensionless solution to be used as a point of comparison between the experimental model and an analytical model.

Normalized Torque Speed Curves

These graphs provide a non-dimensional comparison of torque versus a speed ratio. This is a common metric used to match systems dependent upon torques. The analysis provided here could be used to find a suitable pump or generator to pair with the device. Through dimensional analysis, the following equations can be derived:

$$v_p = \frac{\omega}{2\pi}\lambda$$

$$C = \frac{\omega * \lambda / 2\pi}{U} = \frac{v_p}{U}$$

$$k = \frac{\tau}{\rho * U^2 * A * r}$$

The non-dimensional speed (C) is a function of the wave speed (v_p), and the flow velocity (U). The torque coefficient (k) is given in terms of torque (τ), fluid density (ρ), the square of the flow velocity (U), the swept area (A), and the fin height (r). When reading the graphs C=1 represents the free-running speed of the device, or when there is no applied external load on the system. At C=0, the device has stalled due to the applied external load. An individual data point represents a certain applied torque as a percentage of the available energy, and the wave speed as a percentage of flow speed.

Measurement techniques used in the testing procedure resulted in a high degree of noise in the data, which can be seen clearly in Figure 55. Dense clusters of data at the stall speed and free-running speeds imply higher accuracy at these important locations. Future testing procedures would implement a more reliable system of measurement and torque application, likely using an induction motor, which would produce more accurate results.

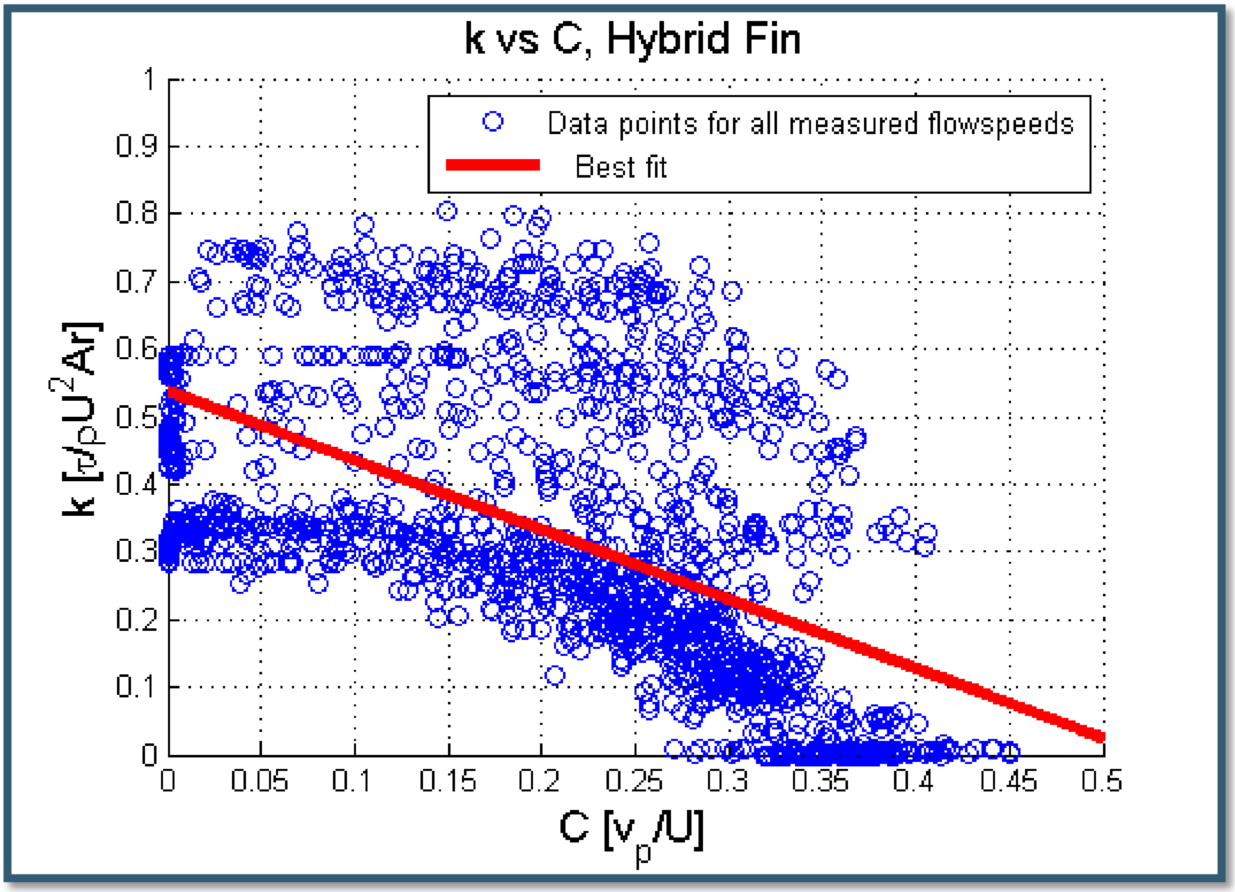

Figure 55: Torque Coefficient versus Non-Dimensional Speed for the hybrid fin.

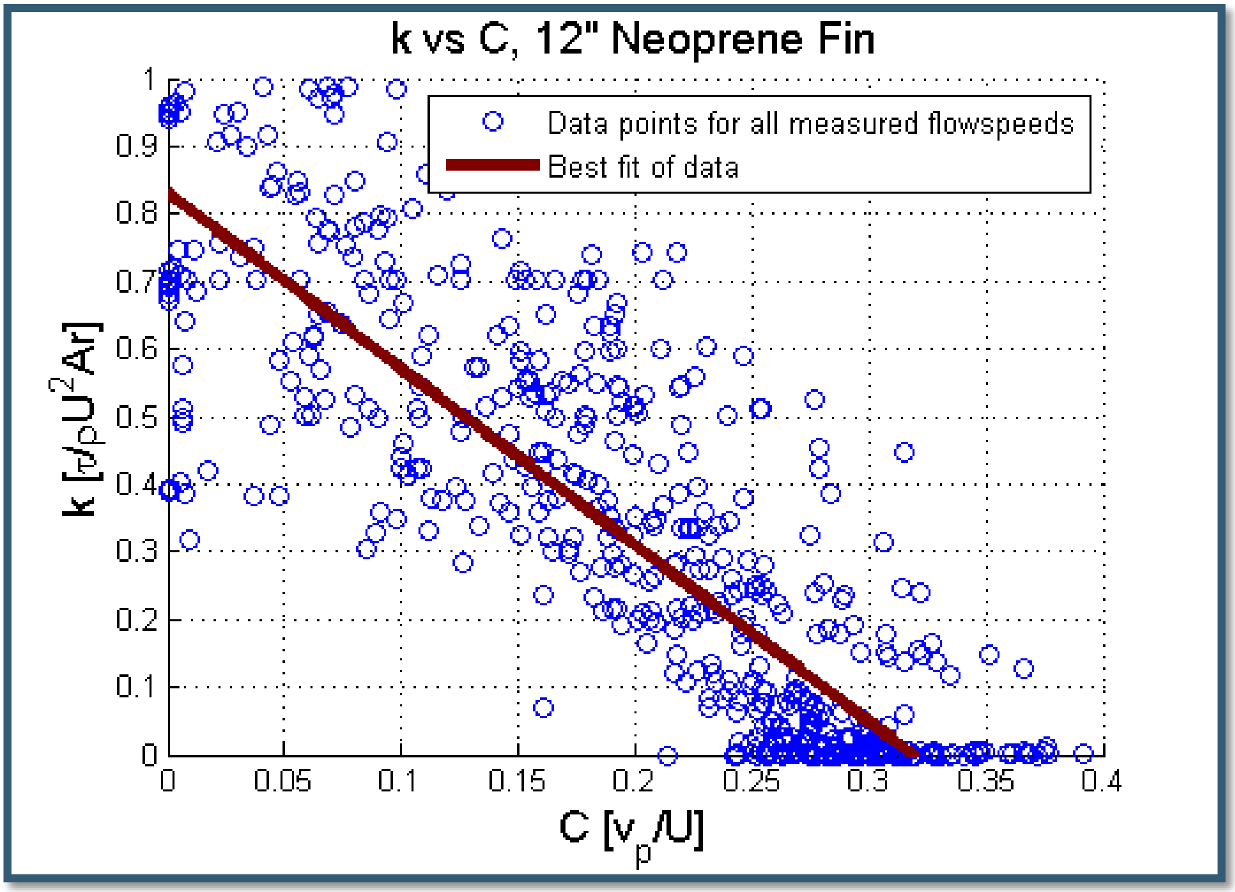

Figure 56: Torque Coefficient versus Non-Dimensional Speed for the 12 inch neoprene fin.

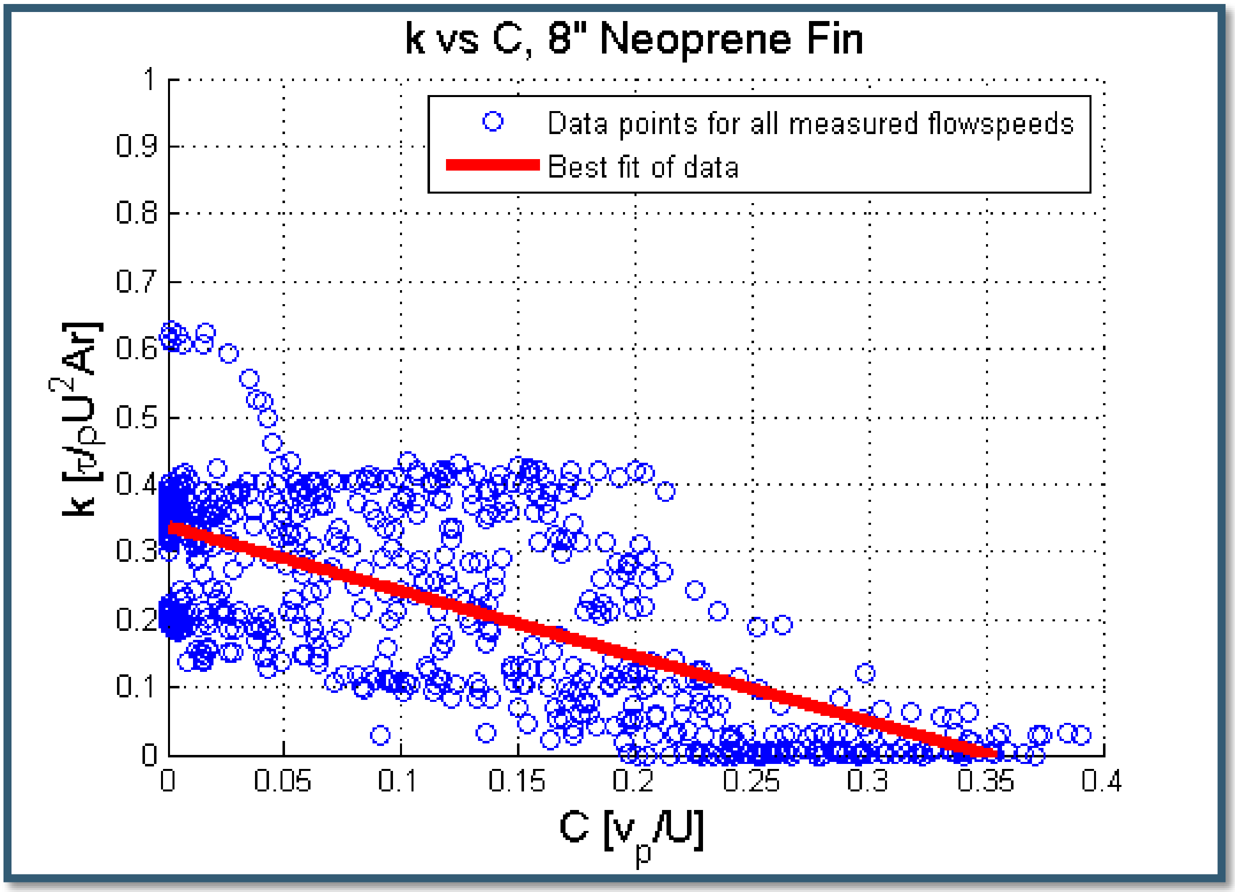

Figure 57: Torque Coefficient versus Non-Dimensional Speed for the 8 inch neoprene fin.

Efficiency Graphs

The efficiency of the device represents the ratio of the power extracted from the flow by the device compared to the power available in the flow volume at each speed. The efficiency (n) is calculated with the equation below. The numerator is the power output of the shaft, calculated by multiplying the torque (τ) and the angular velocity of the shaft (ω). The denominator is the power in the flow, dependent upon the density of the fluid (ρ), the swept area (A), and the cube of the flow speed (U).

$$n = \frac{\tau * \omega}{\frac{1}{2}\rho * A * U^3}$$

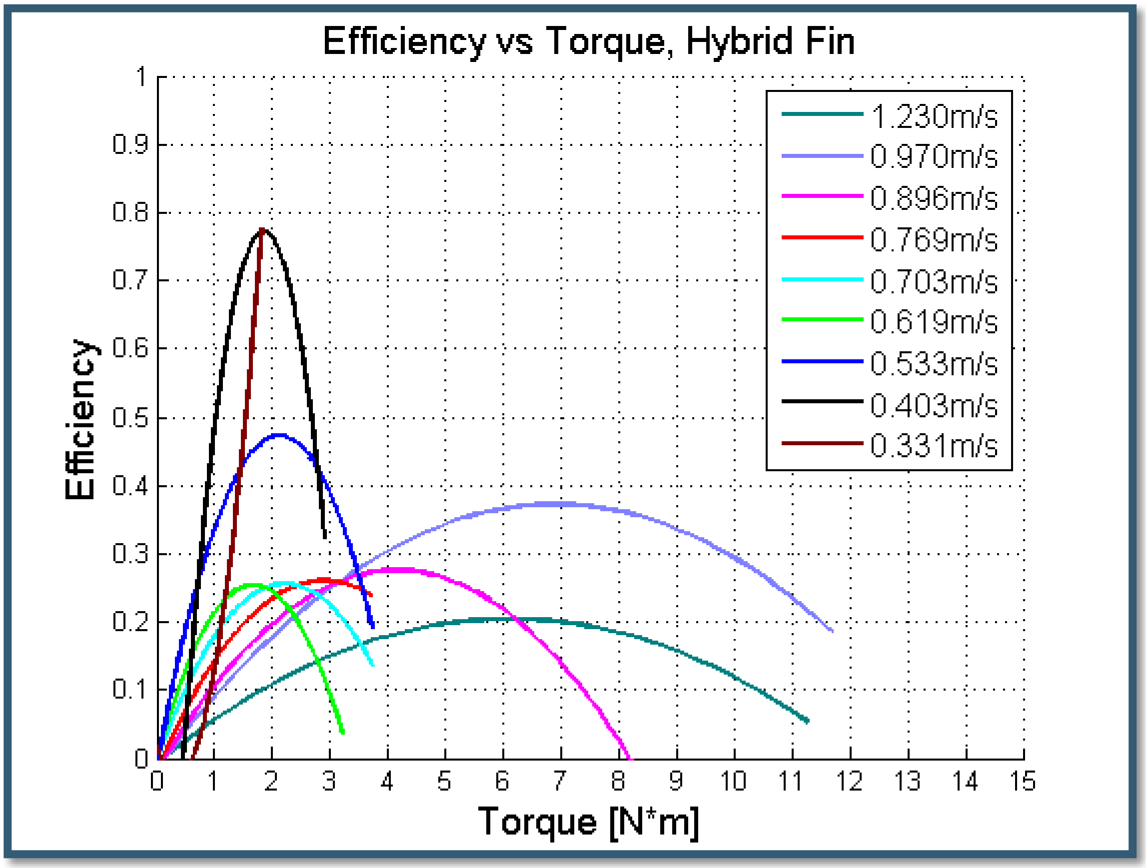

Figure 58: Torque versus Efficiency of the hybrid fin.

The efficiency of the device versus the applied torque at the flow speeds tested for the hybrid fin is presented above. The hybrid fin was very efficient at low flow speeds with low applied torques. The efficiency of the device in this configuration reached 78% when the flow speed was 403 mm/s and the applied torque was approximately 2 N*m. The efficiency was substantially less at the higher flow speeds, though the power output was significantly higher. At a flow speed of 970 mm/s and applied torque of 7 N*m the maximum efficiency was approximately 38%. At the highest speed tested, the efficiency was minimized with a value of 20%. The average peak efficiency under all conditions was approximately 41%.

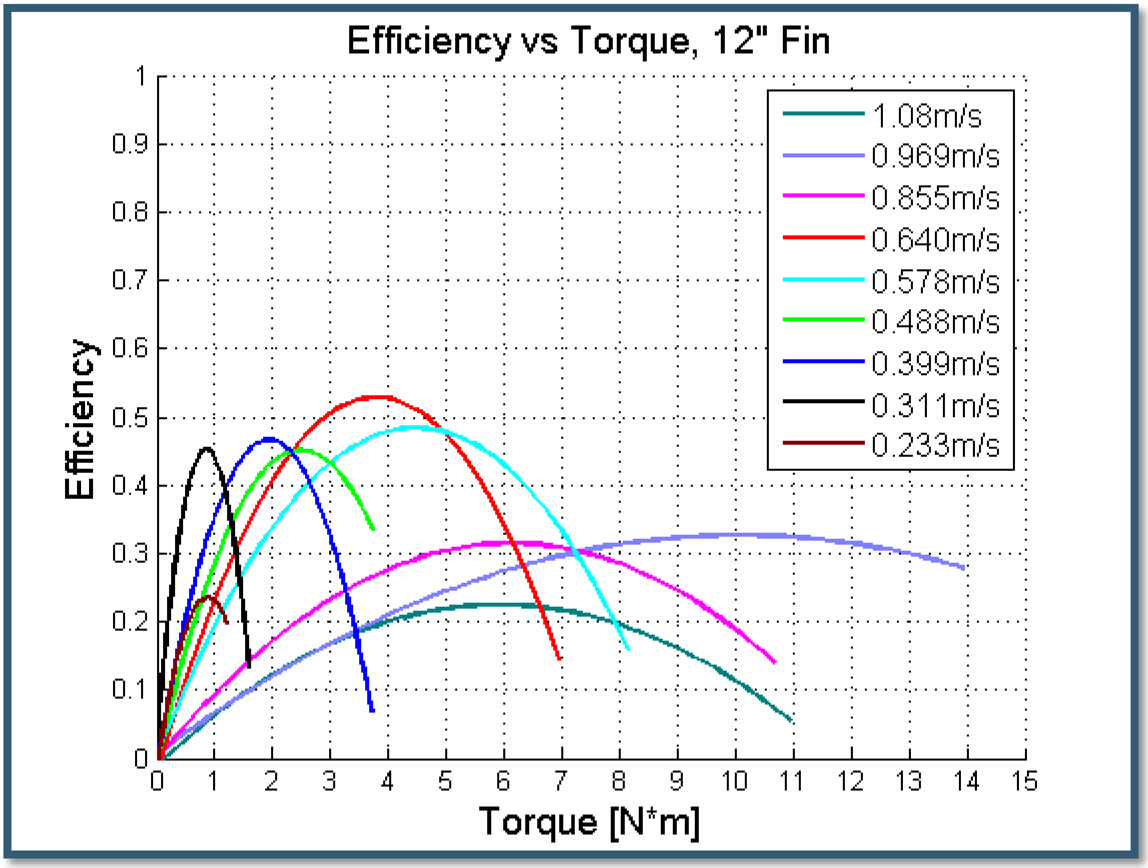

Figure 59: Torque versus Efficiency of the 12 inch neoprene fin.

The 12 inch neoprene fin was, again, most efficient at lower speeds, with low applied torques. The highest efficiency was 53% at a flow speed of 640 mm/s and an applied torque of about 3.5 N*m. The lowest peak efficiency was 22% when the flow speed was 1080 mm/s and the applied torque was 6 N*m. The average peak efficiency for this configuration was 34%. Again, the speeds and torques at which highest power was captured do not correspond with the highest operating efficiencies.

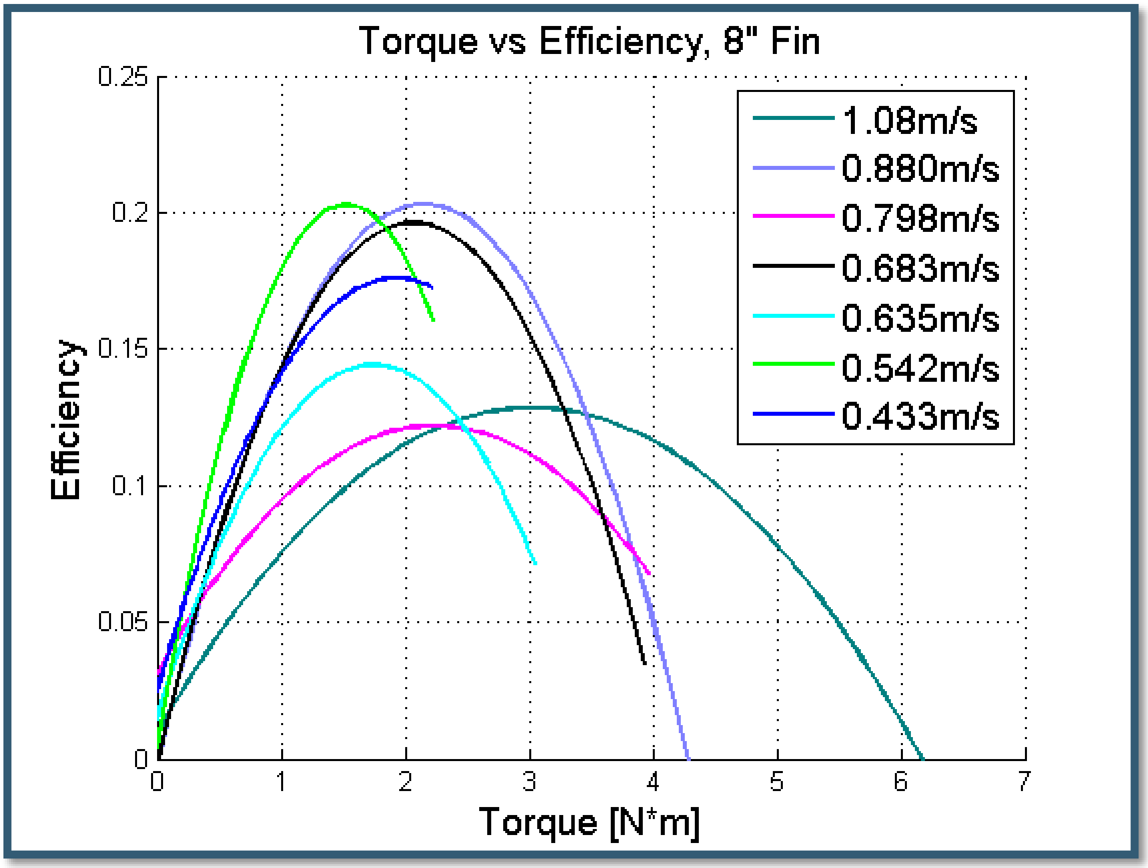

Figure 60: Torque versus Efficiency for the 8 inch neoprene fin.

The efficiency graph for the 8 inch neoprene fin has much more noise than the graphs for the hybrid and 12 inch neoprene fins. Consequently, the lower speed efficiency curves do not provide reliable information and were not included. Additionally, the efficiency of the 8 inch fin at all speeds is much lower than the other two fins discussed thus far. The highest efficiency, 19%, was attained when the flow speed was 683 mm/s and the applied torque was 2 N*m. The efficiency at the highest flow speed was 7%, when torque was 3 N*m. The highest power output was obtained at a flow speed of 880 mm/s with a torque of 2.25 N*m. The peak efficiency for this curve was about 11%. The average peak efficiency for all usable curves was 11.9%.

The 4 inch neoprene had very low overall efficiencies and due to the high cut in speed there was little usable data. The efficiencies under all conditions for this configuration were between 0 and 1.1%.

Figure 61 below provides an overview of the optimal efficiencies for different flow velocities on each respective fin. Each fin experiences a drop in efficiency as the flow speed increases. Larger fins were able to achieve much better efficiencies at low flow speeds and had better efficiencies over all. Smaller fins appear to have a more predictable, nearly linear trend. The lines were generated using a smoothing spline fit.

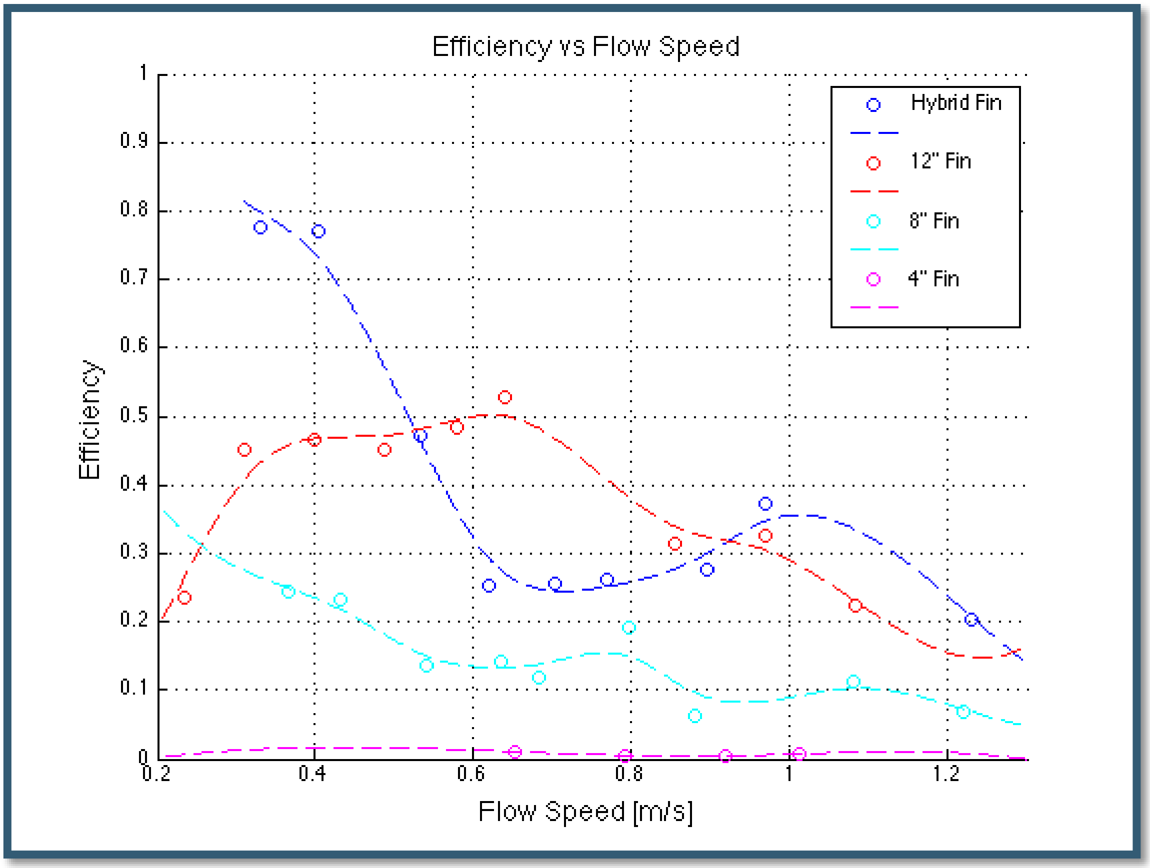

Figure 61: Optimal efficiencies with respect to flow speed for different fin configurations.

Each fin design reached its maximum efficiency between 0.4 m/s and 0.6 m/s. This indicates that at this scale, the device is best suited for flows in this speed range, with the hybrid and neoprene fins reaching efficiencies of 50%. This is remarkable for an early prototype and indicates that additional optimization of the device could lead to higher efficiency across all flows.

When examining the efficiency versus torque graphs, it can be observed that the peak efficiency for a given flow speed occurs at an applied torque that is 50% of the stall torque at that speed. This information is relevant when considering the relationship between the device and an attached power takeoff unit. An electrical generator attached to the output shaft would need to be loaded to apply torque at this percentage of stall torque to ensure that the fin is harvesting energy optimally.

The next three graphs demonstrate the relationship between fin efficiency and non-dimensional speed ratio. This curve allows for the direct comparison between fin iterations, and other fluid based energy extractors.

These graphs adhere to the following equations:

$$C = \frac{\omega * \lambda / 2\pi}{U} = \frac{v_p}{U}$$

$$n = \frac{\tau * \omega}{\frac{1}{2}\rho * A * U^3}$$

C is the non-dimensional speed in terms of the wave speed (v_p) and the flow velocity (U). The efficiency (n) is in terms of torque (τ), shaft speed (ω), density of the fluid (ρ), swept area (A), and the cube of the flow velocity (U).

As in previous efficiency analyses, hybrid fin had the highest efficiency. The average peak efficiencies for the hybrid was around 42% and 12 inch neoprene fin was between 30 and 35%. Both 12 inch fins had significantly higher efficiencies than the 8 inch fin, which had an average peak efficiency of 16%. Note that these maximum values are in the range of C = 0.15 to 0.2, which lends support to the optimal flow speed ratio of 15% found previously. The data points that lie far off of the best fit curve are primarily calculated from data at low flow speeds.

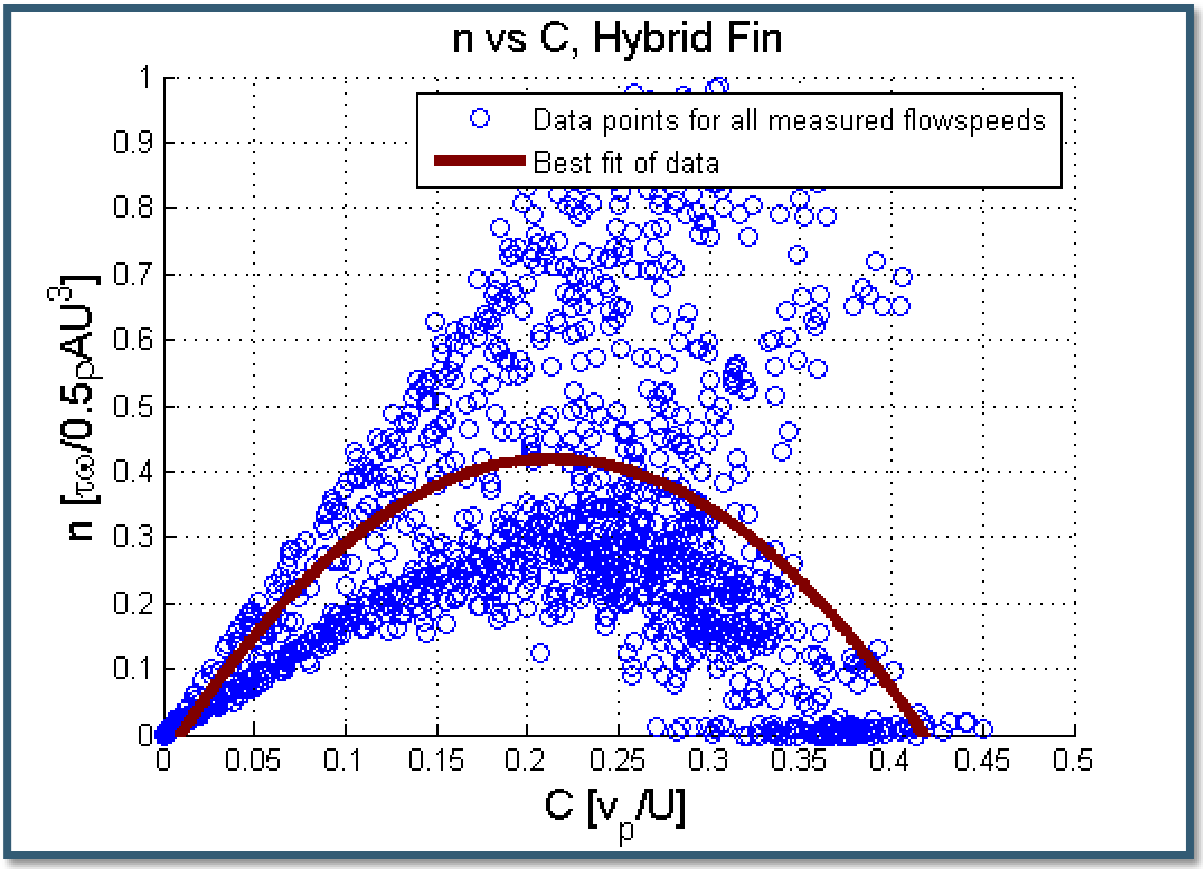

Figure 62: Efficiency versus Normalized Speed for the hybrid fin.

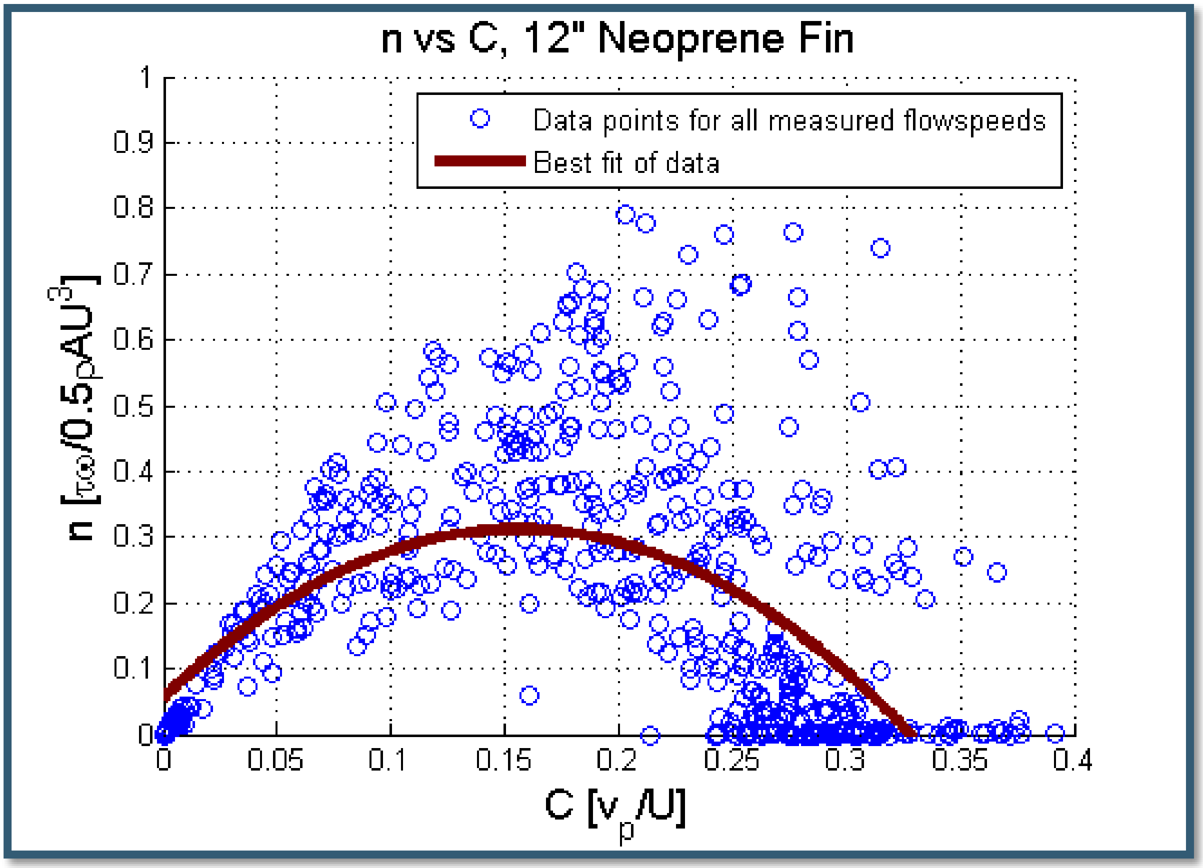

Figure 63: Efficiency versus Normalized Speed for the 12 inch neoprene fin.

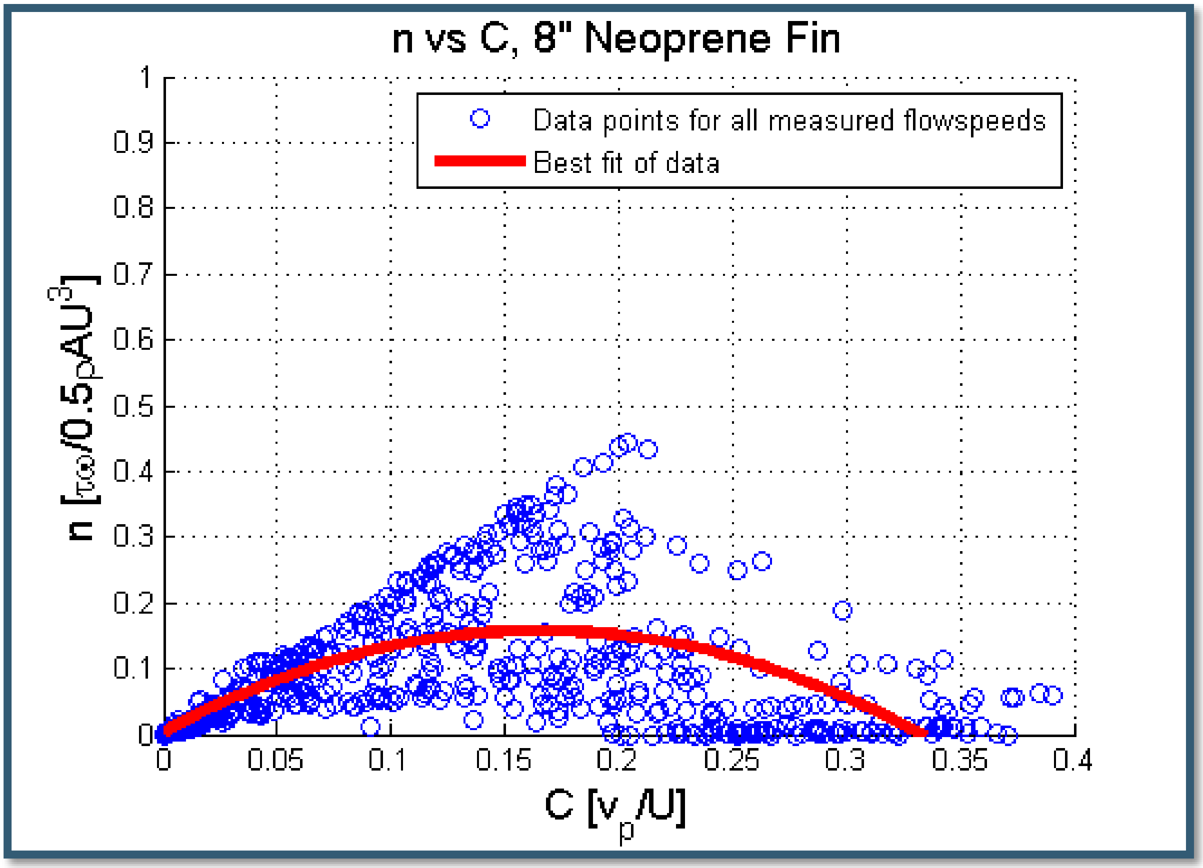

Figure 64: Efficiency versus Normalized Speed for the 8 inch neoprene fin.

Fin Performance Comparisons

The hybrid fin provided the highest power output at flow speeds of approximately 1 m/s, the highest efficiency at low speeds, and the highest average peak efficiency. This is likely due to the increased stiffness in the fin associated with the use of acrylic plates. Originally assumed by the team to be a detriment to energy harvesting, the increased stiffness of the hybrid fin compared to other iterations may have improved it effectiveness by offering more resistance to the impingent flow. The high efficiencies may also be attributed to lack of wear in the mechanism. As the hybrid fin was the first fin tested, this meant that friction in the bearings and cams was at its lowest.

The 12 inch neoprene fin was the second best performing iteration, producing a maximum of nearly 11 watts compared to the 14 watts produced by the hybrid fin. Before testing, the team hypothesized that the 12 inch neoprene fin would be more effective than the hybrid fin. This conclusion was based on a few factors. It was assumed that the more flexible nature of the full neoprene fin would allow it to better hold a waveform down the length of the device. However, the fin proved to be too flexible, and experienced significant folding due to unbalanced wave forces. Additionally, it was assumed that the gaps between plates in the hybrid fin would contribute negatively to the capture of water, reducing its efficiency.

The 8 inch neoprene fin was much less effective than either 12 inch fin, producing a peak power of 3.75 watts, which is only 35% of the power produced by the 12 inch neoprene fin. This decrease in power is caused by a 44% decrease in fin surface area. In addition to reducing the entire surface area of the fin, the remaining fin acted at a shorter lever arm than the taller fins, transmitting a lower force to the output shaft.

The 4 inch fin was completely ineffective, with a cut-in speed between 500 mm/s and 700 mm/s. The reduced surface area and acting lever arm of the fin proved incapable of producing an appreciable power output.

Confounding Factors

During the testing process, sources of error were introduced that may have influenced the quality of the data collected. Potential confounding factors are described in the following paragraphs.

When torque was applied to the device via the dynamometer, two different strategies were employed. During testing of the hybrid fin, a water bottle was gradually filled as it sat on the end of the dynamometer arm. This method did not apply adequate torque at higher flow speeds. To apply sufficient torque, the water bottle method was abandoned in favor of manually applying torque to the arm. This was less consistent and prone to slight oscillation in the load applied, due to movements of the individual applying the load. However, better torque curves were achieved using this method, so the team determined that it was the preferable method for torque application. Because the water bottle method was used for only some of the torque testing on the hybrid fin, it may have confounded the data. This may have inhibited a truly accurate comparison between the hybrid and 12 inch neoprene fins.

The dynamometer also confounded the data due to its construction. The wheel of the dynamometer was not perfectly round and the interface between the force sensor and the wheel was not ideal. This increased frictional forces and induced skipping between the wheel and brake pad, which caused noise in the data. The wheel also had a significant draft on the outer surface, preventing the force sensing assembly from making level contact with the wheel in all positions. Additionally, the dynamometer caused vibration in the mechanism due to its unbalanced nature and its coupling with the device, which may have introduced additional error.

The sensors used to collect data had certain limitations. The flow meter was prone to losing calibration which rendered it ineffective in the highly turbulent environment of the rowing tank. The water bottle flow test, as described in the methodology, was used to overcome the ineffective flow sensor. This method was inherently less accurate than a functioning flow meter would have been, because there were more opportunities for human error. Sources of human error could include the operation of a stopwatch, placement of the bottle in the flow, and inconsistent bottle weight. The force sensor and the rotary sensor were both suitably accurate with the exception that the sensitivity of the force sensor introduced extra noise to the data. Vibrations from other sources in the room including other users of the facility were picked up by the sensor.

While the rowing tank provided decent conditions for testing there were a few key concerns. First, the flow was highly turbulent. This in itself is not a problem as the device would be subject to turbulent flow in any real-world applications. However, the turbulent flow was a significant source of vibration that may have contributed to noise in the data. Second, when flow speeds reached approximately 800 mm/s, standing waves were established down the length of the tank. It is likely that this phenomena impacted the performance of the device.

Partway through testing, the orientation of the cams was reversed. The cam position that had been at the front of the fin was accidentally reoriented to the back of the fin along with the rest of the sequence. While the device theoretically works effectively in both directions, there was a noticeable increase in stalling behavior when the reorientation occurred. This maintenance period may have introduced many operational discrepancies that cannot be isolated from one another. This means that the increased stalling behavior cannot be reasonably attributed to any individual factor.

Qualitative Observations

Vibrations

During testing, significant vibrations were induced in the device, particularly as the flow velocity increased. The team determined that there were several causes for the observed vibrations, these included: instability of the dynamometer, mechanical vibrations inherent within the device due to frictional forces and rotation, and turbulence in the flow.

The dynamometer seemed to be the greatest source of vibration. The design of the dynamometer allowed for few support points, with the entire fixture secured to the device with two screws through the frame and a support on the shaft. This caused the dynamometer to both apply force to the shaft and vibrate significantly as the angular velocity of the shaft increased with flow velocity.

Vibration was also a consequence of frictional forces acting within the cams and the bearings combined with vibrations inherent in a rotating mechanism. The structure of the cams inadvertently allowed for shifting of the steel balls within them, causing jerk and vibrations due to sticking as the cams were twisted by the forces acting on the fin, particularly at higher flow velocities. Furthermore, whenever a mechanism rotates, vibrations are induced, intensifying with increasing angular velocity.

As flow velocity increased, vibrations intensified, with particularly noticeable vibration beginning when the flow velocity reached approximately 800 mm/s. This was partly due to the causes discussed above and partly due to the increasing turbulence of the flow.

Wave quality on the fin

The geometry of the ribbon fin dictates that when two adjacent masts are in the same angular orientation, the distance between each point on the mast is the same regardless of their relative heights from the base. When adjacent masts are at a maximum angular displacement from each other, the distance between any points at the same height along the masts is different. At this maximum displacement orientation, the distance between two points increases with height along the mast. The effect of this geometry means that the length of the fin at its base and top changes depending on the angular displacement between two masts.

At the mechanism's maximum angular displacement, the distance between the tips of the masts is 14 inches. When the masts align in closest proximity to each other, this distance decreases to 6.85 inches.

The changing distance between points on the masts had a significant impact on the quality of the wave sustained by the fin. The arc length of each section of fin was driven by the distances of points on the masts at maximum angular displacement to ensure that the fins were taut. When the masts moved into an orientation where distances were less than this maximum, the excess material of the fin would fold. These minimum distances occur at either extent of the fin's motion, where it changes direction. In this orientation the folding fin section is exposed to the unbalanced forces in the flow, causing the fin to be pushed backwards. As a fin section folds it is less able to harvest energy from the flow, and friction is added to the system. This folding behavior was observed across each iteration of the fin.

Material performance

As testing progressed, the strengths and weakness of the materials chosen for the construction of the device became apparent. The qualities of the materials impacted the performance characteristics of the device. The wood used for the frame was thin relative to its length, and experienced some vibration during testing. Additionally, the wood tended to flex laterally.

The use of 0.0625 inch thick neoprene caused the fin to suffer folding effects, as discussed previously. Without suitable resistance, the neoprene did not hold its shape and thus removed power less efficiently. The acrylic plates in the hybrid fin offered decreased flexibility, which may have contributed to its better performance.

Though the acrylic used for the majority of the mechanism performed well, problems arose when excessive force was applied. During one test, a collar holding the cam in place on the shaft cracked in half because the set screw had been over-tightened during tuning prior to testing. The acrylic parts also presented issues in the way in which they were manufactured. The laser cutter created draft angles along the edges of the cut parts. The draft angle was problematic in the cams because the uneven edge sizes allowed the steel balls to slip and bunch up along the track because there was insufficient material to hold them in place.

The steel hex shaft used tended to bend under certain loads. While this did not present a problem during testing procedures, it was noticeable during transportation of the device to and from the testing facility. The method for transportation was quickly altered as soon as the bending was noticed; however residual bending may have impacted machine performance.

Unwanted cam and pivot torsion

The alignment of the cams and pivots is crucial to the successful function of the device. The original configuration of the device placed the cam rocker assembly half way between the intermediate faces of the frame. As testing proceeded, the thrust force experienced by the masts due to the incoming flow was strong enough to cause significant torsion in the cam-rocker assemblies. This force displaced the rockers on the pivot shaft, which induced torque in the cams, bending them out of plane. When this torsion was applied, the balls within the cam caught on the rails and each other, which added a high amount of friction to the entire system.

At one point during testing, the torsion in the cams reached a level where the steel balls popped out of the cams. Testing was halted immediately and repairs to the mechanism were required. Additional support had to be added to the cam-rockers to ensure that the device would be able to withstand the effects of continued testing. To address this, each cam-rocker was repositioned as to be adjacent to an intermediate face of the frame. With this configuration the thrust force was resisted by the frame, keeping the cam and rocker aligned and preventing additional friction. With this improvement, tests became more reliable and effective.

Additional Observations

As the fin moves through its swept area it experiences a pressure which necessarily acts normal to the fin's surface. This vector can be decomposed into three orthogonal vectors: a thrust force which that acts axially, a lateral force acting normal to the medial plane of the fin, and a lift force that acts radially and vertically. The local curvature of the fin affects which of these forces is dominant.

The thrust and lateral forces are the principal forces in driving the oscillation of the fin. The forces in these directions act on the greatest percentage of the fin's surface area at any given time. Guided by the wave held on the fin, the thrust and lateral forces push fin segments through the cycle. The thrust force had the additional effect of pushing the entire device in the direction of flow. When pushed far enough, the dynamometer was pressed against the mounting rig, introducing an unbalanced torque to the system. Tape was used to secure the device in place and to counteract the thrust force.

The lift force plays a lesser role in inducing output shaft rotation. Not designed to extract energy in this direction, the fin was ill-equipped to deal with this force. As flow velocity increased the lift force became significant enough to act against the force of gravity and lift the device from the testing rig. This force compresses the entire device, and could cause problems in models of a larger scale.

As flow speeds increased and the standing waves were established in the tank, water began to enter the eccentric cams and bearings at the pivot points. Additional friction was incurred at these points as the water caused parts to stick. This is likely due to the material selection. The interface between the steel balls in the cam and the acrylic of the rest of its body was particularly susceptible to sticking due to the water introduced.

Further Investigations

An important design aspect that could likely be improved upon in future work is the stiffness of the fin material. In both the hybrid and the solid neoprene fins a folding effect was present, where slack in the fin was pushed back by the flow so the fin failed to hold the critical sinusoid shape. This phenomenon could be reduced by using a stiffer material for the fin membrane, one that would better hold the desired shape. This could be achieved by constructing a fin with either a thicker cast rubber fin, or a fully plated fin with sprung joints. Sprung joints would allow a plated fin to adjust its length to accommodate changes in mast position and prevent folding.

The decision to use an eccentric cam shaft in place of a crankshaft offered reasonable advantages for construction at this scale. However, it seems that at a larger scale it may be preferable to use a crankshaft. Manufacturing large bearings would become increasingly expensive as size increased, and the relative advantages in compactness and reliability of a crankshaft would quickly offset the construction costs.

A phenomenon discussed by Shirgaonkar et al [28] is the heave force, previously described as the lift force, which acts vertically due to fluid that is pushed out of the swept volume radially. This force produces unfavorable torque on the frame of the device, and would be a major design hurdle for the installation of any large scale iteration of this concept. The heave force could be offset in a number of ways, the simplest being building the frame to withstand the force. Other ways could include adding a foil perpendicular to the fin at its outer edge to reduce spill from the swept area; similar to the way a plane improves its lift and efficiency by employing winglets that inhibit spill induced vortices. In a deployed version of this device, the heave force could be offset by shifting buoyant ballast within the hull that contains the mechanism.

In a deployed version there could be numerous possibilities for fin orientation and mounting fixtures. These include: a downward oriented fin protruding from a floating hull at the water's surface, or an upward oriented fin protruding from a hull anchored to the seafloor or riverbed. Most tidal stream generators in production currently are bottom mounted, as this isolates them from the waves and weather at the surface and keeps them out of the way of surface activity such as shipping. The advantages of surface mounting are accessibility and ease of deployment. A device that protrudes from the bottom of a buoyant hull would be serviceable in a dry environment and deployable in a variety of situations. Although the device would restrict the area for use by surface vessels, it would have access to the highest flow velocity and be able to naturally yaw with the flow by trailing its mooring point.

Bottom mounting could be accomplished in a variety of ways including sinking the hull into the sediment, pivoting about a piling, or floating in tension against a mooring. Pivoting about a piling presents the least complexity with the least compromise to functionality, retaining the ability to yaw but mitigating the need for a costly tether system. Ultimately the mounting type would be case specific with high traffic and high weather areas warranting bottom mounting while high current smaller deployments warrant surface mounting.

Full scale implementation of this device would necessitate a watertight enclosure to protect the interior components from the environment. If the device were deployed a skirt could be used to enclose the mechanism and power takeoff machinery. Secured to the surface of the frame, a skirting would be stretched across the cam-rocker assemblies, attaching to the base of the masts, allowing the mast to actuate while maintaining a sealed environment within. Even the limited exposure to a wet environment had a negative impact on the prototype, proving the necessity of a sealed hull for future developments.

Although wavelength variations were not tested on this device, it was designed to accommodate fins of varying wavelength. Research and initial calculations suggest that power extraction can be optimized by exploring additional wavelength configurations. It is critical for future iterations to explore the effect of varying wavelengths on performance so that a deployed device would be best suited to its environment.

Fin Height and Power Output

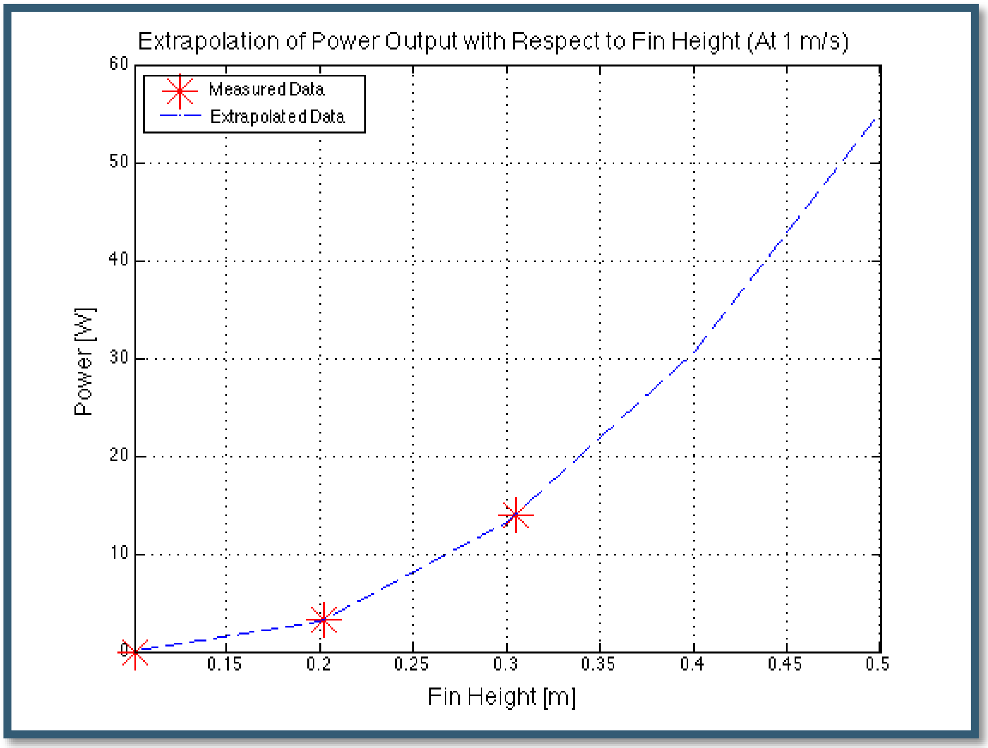

Figure 65: Extrapolation of Power Output with respect to Fin Height at 1 m/s. Up to a fin height of 0.5 m.

The above graph provides a rough estimate of possible power output if the height of the fin were increased to 0.5 meters. The team is reasonably confident that the extrapolation up to 0.5 meters provides a valid representation of the potential power output based upon the fully neoprene fin designs at heights of 4, 8, and 12 inches. Inaccuracies in the extrapolation may be present due to the limited number of data sets and the poor quality of data from the 4 inch neoprene fin tests. Based on this extrapolation it is reasonable to expect that a 0.5 meter fin, operating in a flow of 1 m/s at 30% efficiency, would output 55 watts.

Further extrapolation to a fin height of 1.0 meter can be done with less confidence. The graph below illustrates that a fin height of 1.0 meter may produce up to 275 Watts under the same conditions described above. Lack of good data sets does not provide a high degree of certainty in this estimation. It is congruent, however, with initial calculations predicting a strong correlation between fin height and power output. More accurate extrapolations could be made if at least one additional data set was collected, with a fin height in excess of 12 inches.

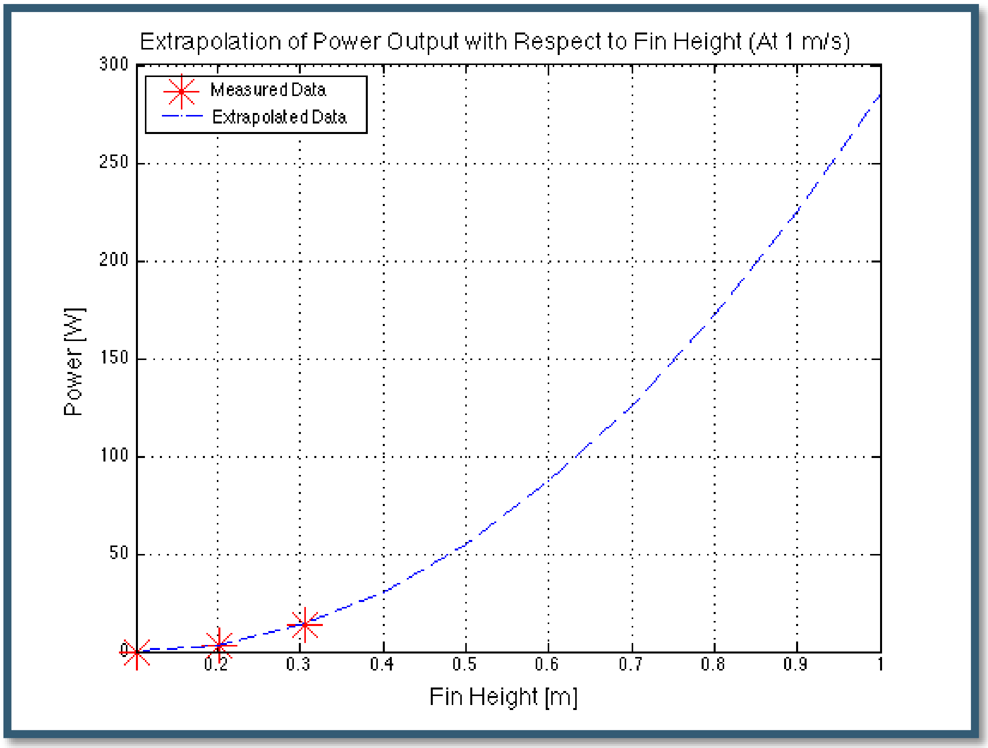

Figure 66: Extrapolation of Power Output with respect to Fin Height at 1 m/s. Up to a fin height of 1.0 m.

Discussion

The results and analysis show two major points. The device is a novel and viable technology, especially with the contemporary return of low density power generation. The initial results are promising. However, the data also shows that much more work needs to be done before the device is directly competitive with current technologies.

The efficiency curves suggest good power generation at low flow speeds, an important niche that needs to be filled. Many modern hydropower systems require either high velocity streams or large gravitational potential to generate significant power. The device could potentially allow power extraction from many untapped sources.

Due to the noise in data collection, the results were presented conservatively. Future optimizations of design and improved testing procedures should lead to more promising results and a better understanding of the physics of this new power generation device.

Conclusion

This project, spread out over a five month time frame, exhibited numerous constraints on both design and testing methodologies. With only so much time to perform research, design, manufacturing, and testing, limits on what was to be accomplished had to be established. Beginning with an interest in harnessing tidal energy, a unique and effective method of harvesting the kinetic energy of water was created.

A great deal of promise has been shown by the ribbon fin power capture concept. The prototype developed for this study has shown that a ribbon fin mechanism can indeed extract power from a stream of water; and that it can do so at a variety of flow speeds while remaining stable and relatively efficient. From the origin of the concept to its application as a power generator, a number of physical and mechanical concepts have been investigated both experimentally and analytically. The mechanical design of a device that can govern a propagating wave in a flexible ribbon of material was key. In this regard, success was largely achieved, with the device constructed holding the sinusoidal fin shape effectively and ensuring that the masts followed the desired angular displacement with minimal friction.

The device performed surprisingly well for a small scale prototype. It achieved average efficiencies of up to 41% with the hybrid fin and 35% for the 12 inch neoprene fin. The maximum power output was 14 watts from the hybrid fin. This power output is sufficient to light a few LED lightbulbs if converted to electrical power. Extrapolations up to a fin height of 0.5 meters (approximately 20 inches) indicate that at least 55 watts of power could be expected, even with modest efficiencies of 30%.

Two fin construction concepts were tested in the interest of establishing possible designs for later iterations of the technology. The hybrid fin construction, composed of jointed acrylic plates and neoprene rubber sheets, performed better than expected. It followed the flow without significant resistance and exhibited no more folding than the full neoprene fin. Contrary to initial expectations, the neoprene fin performed less well than the hybrid fin. Future iterations of the device could include a fully plated fin with spring joints to increase rigidity and prevent folding behavior.

Though the eccentric cams incorporated in the prototypes worked well at the small scale, further models would likely need to use a crankshaft. Use of a crankshaft would provide greater stability and the issues created by torsion in the cams due to imperfect alignment and forces from the fin would be eliminated. The eccentric cam design was originally selected for its ease of manufacture with the tools available. With further time and development, a crankshaft would provide better mechanical movement.

If developed further, this device could be deployed in a variety of locations and conditions. Small scale models, of no more than a meter in fin height, could be easily deployed in rivers. Larger models, of up to several meters in height, could be deployed at sea for tidal current energy capture. At small scales, the cost to manufacture and deploy this technology could be very low, making it ideal for use in developing countries, rural communities, or remote regions.

This design has several advantages over traditional hydro turbines. The most unique benefit is that it captures energy from a swept volume as opposed to a swept area. This enables it to work efficiently at low flow speeds and capture energy from the flow even as it is decelerated down the length of the fin. Further, because the device captures energy through a volume, it is not bound to the Betz limit for efficiency.

This project developed a novel device for hydrokinetic energy capture. With further research and development, this device has the potential to be implemented in a variety of settings and under various flow conditions. Energy captured could be used to pump water for integration into a pumped hydroelectric plant or for domestic use. It could also be used to generate electricity for household or grid level production. The scalability of the design gives it a variety of potential uses and applications and the expected low cost to manufacture, combined with high efficiencies, make it a potential competitor in the developing hydrokinetic energy field.

Bibliography

[1] Atlantis Resources Ltd., 2014, http://atlantisresourcesltd.com/turbines/ar-series/ar1500series.html.

[2] Aquamarine Power Ltd., 2005, http://www.aquamarinepower.com/.

[3] Birkholz, D., 1997, "Preservation of Iron Ships in the Marine Environment," http://www.maritime.org/conf/conf-birkholz.htm.

[4] Boake, C. B., Whittaker, T. J., Folley, M., and Ellen, H., "Overview and initial operational experience of the LIMPET wave energy plant," Proc. Proceedings of the 12th international offshore and polar engineering conference, pp. 26-31.

[5] Bureau of Ocean Energy Management, 2014, “Ocean Current Energy,” http://www.boem.gov/Renewable-Energy-Program/Renewable-Energy-Guide/Ocean-Current-Energy.aspx.

[6] Deane, J.P., O Gallachoir, B.P., McKeogh, E.J., 2010, “Techno-economic review of existing and new pumped hydro energy storage plant,” Renewable and Sustainable Energy Reviews, 14(4), pp. 1293-1302.

[7] Denny, E., 2009, "The economics of tidal energy," Energy Policy, 37(5), pp. 1914-1924.

[8] The Engineering Business Ltd., 2002, “Stingray: the Tidal Stream Generator,” http://www.see.ed.ac.uk/~eeto/Modules%20-%20do%20not%20use/45-07/Handouts/tidal/Stingray/The%20Stingray%20Generator.pdf.

[9] The Engineering Business Ltd., 2005, http://www.esru.strath.ac.uk/EandE/Web_sites/05-06/marine_renewables/technology/oschydro.htm

[10] Garrett, C., Cummins, P., 2005, “The power potential of tidal currents in channels,” Proceedings of the Royal Society, Proceedings A.

[11] Gill, A. B., 2005, "Offshore renewable energy: ecological implications of generating electricity in the coastal zone," Journal of Applied Ecology, 42(4), pp. 605-615.

[12] Haas, K.A., Fritz, H.M., French, S.P., Smith, B.T., Neary, V., 2011, “Assessment of Energy Production Potential from Tidal Streams in the United States,” U.S. Department of Energy.

[13] Hagerman, G., 2011 “Mapping and Assessment of the United States Ocean Wave Energy Resource,” 1024637 EPRI, Palo Alto, CA.

[14] Hitchcox, A., 2012, “Water Hydraulics: Benefits and Limitations,” Hydraulics & Pneumatics.

[15] Jansen, T., 2015, Strandbeest, http://www.strandbeest.com/photos.php.

[16] Jayashankar, V., Anand, S., Geetha, T., Santhakumar, S., Jagadeesh Kumar, V., Ravindran, M., Setoguchi, T., Takao, M., Toyota, K., and Nagata, S., 2009, "A twin unidirectional impulse turbine topology for OWC based wave energy plants," Renewable Energy, 34(3), pp. 692-698.

[17] Kinea Designs, 2010, Ghostbot, http://www.kineadesign.com/portfolio/fish/

[18] Leijon, M., Skoglund, A., Waters, R., Rehn, A., and Lindahl, M., 2010, "On the physics of power, energy and economics of renewable electric energy sources – Part I," Renewable Energy, 35(8), pp. 1729-1734.

[19] Liu, H., Masera, D., Esser, L., 2013, “World Small Hydropower Development Report 2013,” United Nations Industrial Development Organization, International Center on Small Hydro Power.

[20] Neill, S. P., Litt, E. J., Couch, S. J., and Davies, A. G., 2009, "The impact of tidal stream turbines on large-scale sediment dynamics," Renewable Energy, 34(12), pp. 2803-2812.

[21] Paish. O., 2002, “Small hydro power: technology and current status,” Renewable and Sustainable Energy Reviews, 6(6), pp. 537-556.

[22] Ocean Power Technologies, 2015, http://www.oceanpowertechnologies.com/powerbuoy/.

[23] Ocean Renewable Power Company, 2014, http://www.orpc.co/.

[24] Pelamis Wave Power, 2012, http://www.sciencespacerobots.com/pelamis-wave-power-sea-snake-wins-saltire-prize-32820124.

[25] Pelamis Wave Power, 2014, http://www.pelamiswave.com.

[26] SDE ltd., 2015, https://wavesinchile.wordpress.com/possible-solutions-and-technologies/

[27] Shields, M.A., Woolf, D.K., Grist, E.P.M., et al., 2011, “Marine renewable energy: The ecological implications of altering the hydrodynamics of the marine environment,” Ocean & Coastal Management, 54(1), pp. 2-9.

[28] Shirgaonkar, A. A., Curet, O. M., Patankar, N. A., and MacIver, M. A., 2008, "The hydrodynamics of ribbon-fin propulsion during impulsive motion," The Journal of Experimental Biology, 211, pp. 3490-3503.

[29] Stansell, P., Pizer, D.P., 2012, “Maximum wave-power absorption by attenuating line absorbers under volume constraints,” Cornell University.

[30] Tester, J.W., Drake, E.M., Driscoll, J., Golay, M.W., Peters, W.A., Sustainable Energy: Choosing Among Options, 2nd Edition, MIT Press, Cambridge, MA.

[31] Thorpe, T.W., 1999, “A Brief Review of Wave Energy,” http://people.bath.ac.uk/mh391/WavePower/limpet.html

[32] Torre-Enciso, Y., Ortubia, I., López de Aguileta, L., and Marqués, J., "Mutriku Wave Power Plant: from the thinking out to the reality," Proc. Proceedings of the 8th European Wave and Tidal Energy Conference, pp. 319-329.

[33] UC Davis ChemWiki, 2015, “Sacrificial Anode,” http://chemwiki.ucdavis.edu/Analytical_Chemistry/Electrochemistry/Case_Studies/Corrosion/Sacrificial_Anode.

[34] Energy, U. S. D. o., "Marine and Hydrokinetic Technology Database."

[35] Williams, A.A., 1996, “Pumps as turbines for low cost micro hydro power,” Renewable Energy, 9(1-4), pp. 1227-1234.

[36] World Energy Council, 2013, “World Energy Resources: 2013 Survey,” World Energy Council.

[37] http://emmanuel.branlard.free.fr/work/papers/html/2008ecn/actuatordiskb.png

Appendix A: Analysis of Concepts

The 'Feathering Oar' is a concept wherein a plate is attached to the end of an arm and is positioned normal to the flow of water. The arm is deflected angularly until it lies nearly flat. At this time, the plate is "feathered," or turned a quarter turn so as to face the flow edge on. When this is done the plate returns to the vertical position, feathers back to a high drag orientation, and repeats the power stroke. During the power stroke there are two contributing forces, the form drag that creates a horizontal force, parallel to the flow, and the lift force, which contributes a downward force when the plate leaves the 'stall' condition near horizontal. There is a skin drag force during the power stroke, but it only creates tension in the arm and not torque.

Oar Parameters:

$$\text{oar\_h} := 2\text{m}$$

height of the plate

$$\text{oar\_w} := 1\text{m}$$

width of the plate

$$\text{mast\_L} := 3\text{m}$$

length of the arm to which the plate is affixed

$$\theta := 0, \frac{\pi}{200} .. \frac{\pi}{2}$$

angular range through which the arm or 'mast' travels (full vertical to horizontal; plate is pushed over by flow)

Flow Parameters:

$$\rho := 1025 \frac{\text{kg}}{\text{m}^3}$$

density of water

$$\mu := 1.07 \cdot 10^{-3} \frac{\text{kg}}{\text{m} \cdot \text{s}}$$

viscosity of water

$$U := 1 \frac{\text{m}}{\text{s}}$$

velocity is held at 1 m/s for concept validation

$$\text{Re\_L} := \frac{\rho \cdot U \cdot \text{oar\_h}}{\mu} = 1.916 \times 10^6$$

Reynolds number (at longest plate dimension)

Pressure drag:

$$\text{h\_prj}(\theta) := \sin(\theta) \cdot \text{oar\_h}$$

The pressure drag component is strictly horizontal, thus the plate height is projected onto the plane normal to the flow.

$$\text{Cpd}(\theta) := 1.11 + 0.02 \cdot \left(\frac{\text{oar\_w}}{\text{h\_prj}(\theta)} + \frac{\text{h\_prj}(\theta)}{\text{oar\_w}} \right)$$

the coefficient of pressure drag for a flat plate

$$\text{drag\_pressure}(\theta) := \frac{1}{2} \text{Cpd}(\theta) \cdot \rho \cdot U^2 \cdot (\text{oar\_w} \cdot \text{h\_prj}(\theta))$$

force of pressure drag for a given angle

Lift Force:

$$\text{Clo}(\theta) := \cos(\theta) \cdot 2 \cdot \pi \cdot \theta$$

the coefficient of lift for the plate as provided by NASA; the equation is only valid outside of the stall condition, thus a cosine term is added to approximate the force cutting in at lower angles

$$\text{lift}(\theta) := \frac{1}{2} \cdot \text{Clo}(\theta) \cdot \rho \cdot U^2 \cdot (\text{oar\_w} \cdot \text{h\_prj}(\theta))$$

the lift force for a given angle

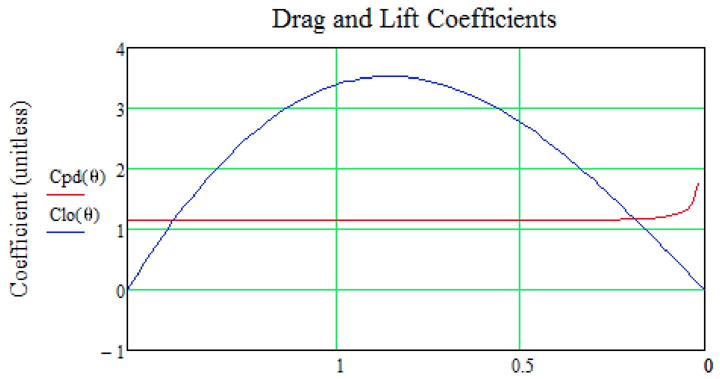

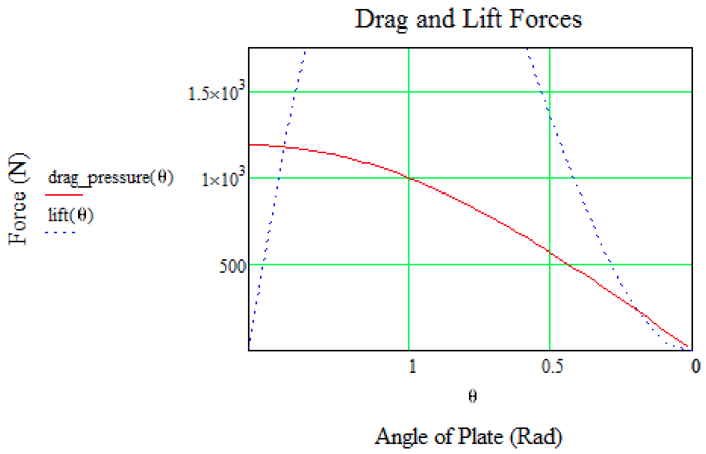

Torque and Energy:

Torque is calculated for angular position by combining both force equations and multiplying them by the lever arm supplied by the distance from the pivot point to the center of the plate.

$$T(\theta) := drag\_pressure(\theta)\cdot\sin(\theta)\cdot\left(mast\_L - \frac{oar\_h}{2}\right) + lift(\theta)\cdot\cos(\theta)\cdot\left(mast\_L - \frac{oar\_h}{2}\right)$$

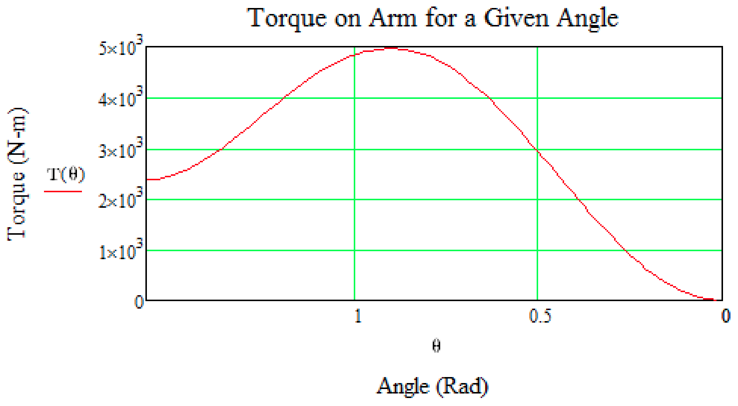

Determining the dynamic torques (Those present as the arm is deflected) would necessitate the consideration of relative velocities produced by the plates movement relative to the water moving over it. For the purpose of these calculations it will be sufficient to integrate the static torque over the angular sweep to find the "Energy in a Stroke." This metric will suffice only for the purpose of comparing this and the next concept as they will use the same equations and make the same, although to some extent unrealistic, assumptions.

Being a wave, the ribbon has properties such as:

$n := 0, 0.1 .. 10$ number of waves on the length

$\lambda(n) := \frac{L}{n}$ wavelength (as a function of n)

$f(n) := \frac{U}{\lambda(n)}$ frequency (also as a fuction of n, but defined by wave length and flow speed)

Ribbon-Force Equations as provided by Shirgaonkar et al.

$$\Phi(n) := \frac{1 - e^{-\left(\frac{\frac{\lambda(n)}{L}}{0.6}\right)^2}}{\frac{\lambda(n)}{L}}$$

specific wavelength approximation

$C1 := 86$ experimental constant (86 in their study. For ours it will be reduced to 1, which, although confounding for quantitative results still affords qualitative study.)

$$F(n) := C1 \cdot \rho \cdot f(n)^2 \cdot L^4 \cdot \theta max^{3.5} \cdot \left(\frac{h}{L}\right)^{3.9} \cdot \Phi(n)$$

the force equation

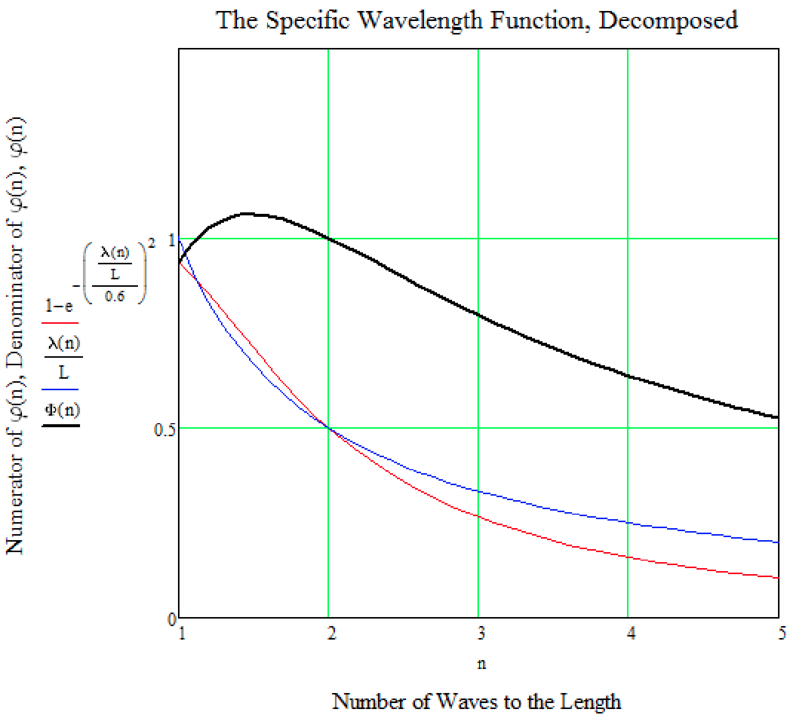

When other aspects of the equation are held constant, it is the specific wavelength that becomes the term of interest, and it would appear to reach a maximum on the high side of 1.

Appendix B: Geometric Parameters Governing Ribbon Dimensions

Inputs:

$len := 30in$	overall length of the ribbon
$x := 0in, 0.01in .. len$	range from 0 to total length, 100 steps per inch
$n := 5$	number of 15degree steps of displacement between each mast
$\lambda := \frac{360}{15 \cdot n} \cdot 6in = 28.8\,in$	length of a single wave on the ribbon
$\rho := 1000 \frac{kg}{m^3}$	density of water
$r_{tip} := 13in$	radius of apparatus, essentially the height of each mast
$r_{base} := 1in$	
$\theta max := 45deg$	extent of angular displacement from vertical
$form(x) := \theta max \cdot \sin\left(2 \cdot \pi \cdot \frac{x}{\lambda}\right)$	function showing the angular displacement of the ribbon along it's length

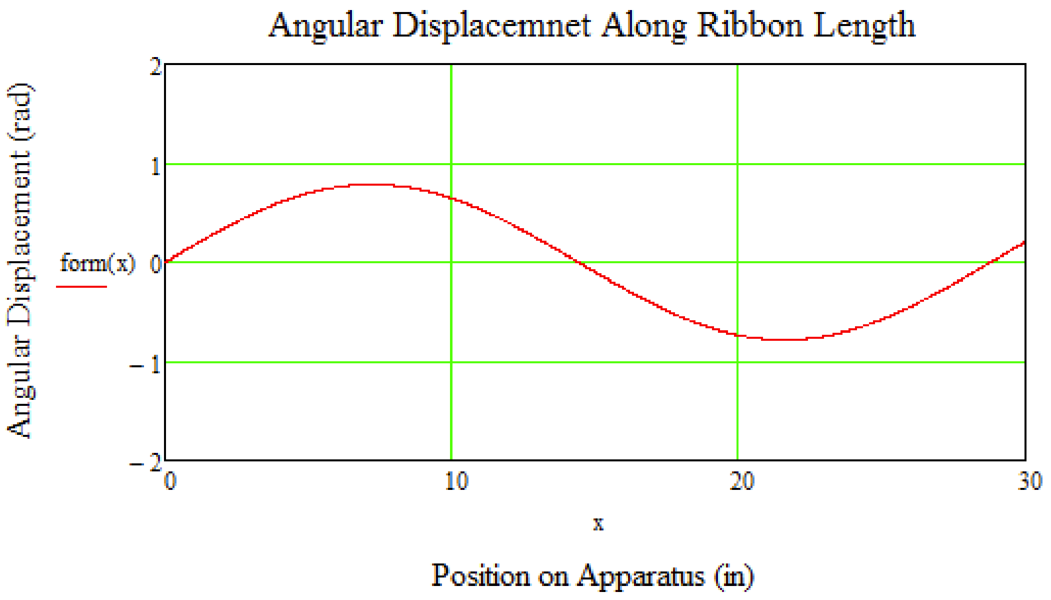

Geometric Calculation for Prototyping Ribbon:

$$\mathrm{edgeL}(r) := \int_0^{len} \sqrt{1 + \left(\frac{d}{dl}\mathrm{form}(l)\cdot r\right)^2}\, dl$$

arc length along ribbon at any distance from axis

$L_{base} := \mathrm{edgeL}(r_{base}) = 30.227\,in$ length along bottom of ribbon

$L_{tip} := \mathrm{edgeL}(r_{tip}) = 54.662\,in$ length along top of ribbon

Given

$r_1 := 1in$ inner radius of pattern

$r_2 := 1in$ outter radius of pattern

$\theta := 1rad$ angle needed for pattern

$L_{base} = \theta\cdot r_1$ Arclength at radii considering common angle

$L_{tip} = \theta\cdot r_2$

$r_2 - r_1 = r_{tip} - r_{base}$ The relationship between the pattern radii and the mast radii

$$L_{base}\cdot(r_{tip} - r_{base} + r_1) = L_{tip}\cdot r_1$$

$$\frac{L_{base}\cdot(r_{tip} - r_{base})}{(L_{tip} - L_{base})} = r_1 \qquad r_1 := \frac{L_{base}\cdot(r_{tip} - r_{base})}{(L_{tip} - L_{base})} = 14.845\,in$$

$$r_2 := r_{tip} - r_{base} + r_1 = 26.845\,in$$

$$\theta := \frac{L_{base}}{r_1} = 116.665\cdot deg \qquad \theta := \frac{L_{tip}}{r_2} = 116.665\cdot deg$$

The ribbon is cut from a thin planar sheet of polyethylene and fits fairly taught to the masts having a rectangular profile but a longer top edge than bottom edge.

Appendix C: Wave Speed Decay Model

Inputs:

$len := 30in$ overall length of the ribbon

$x := 0in, 0.01in .. len$ range from 0 to total length, 100 steps per inch

$\rho := 1000 \frac{kg}{m^3}$ density of water

$r_0 := 12in$ initial radius of apparatus

$\theta_0 := \frac{\pi}{4} = 0.785$ angular amplitude, from vertical

$n := 1$ number of cycles expressed in the fin

$U_0 := 0.75 \frac{m}{s}$ range of flow velocities from 0 to 2 m/s with 10 steps per m/s

Power take-off by Wave Speed Decay

$A_0 := \theta_0 \cdot r_0^{\,2} = 0.073 \cdot m^2$ the 'inlet' or swept sector area

$P_0 := \frac{1}{2} \cdot A_0 \cdot \rho \cdot U_0^{\,3} = 15.391\,W$ power available from stream that passes through swept area

$$S(x,\varepsilon) := U_0 \cdot \left(1 - \varepsilon \cdot \frac{x}{len}\right)^{\frac{1}{3}}$$

Wave speed as it decreases along the length of the axis, assuming that the water in the control volume follows an inverse cubic relationship to create a linear decrease in power.

$$P(x,\varepsilon) := \frac{1}{2} \cdot \rho \cdot A_0 \cdot S(x,\varepsilon)^3$$

Energy flux through sections of the control volume. A linear decrease in power would entail an even distribution of power taken by each mast.

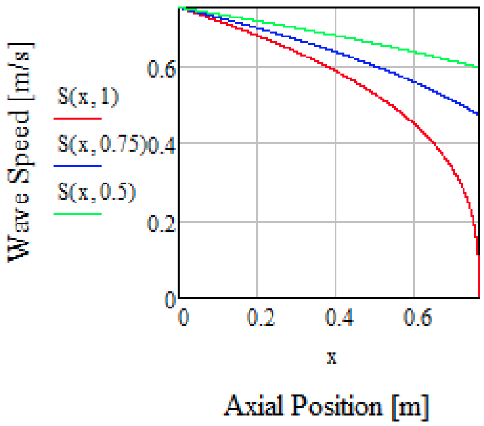

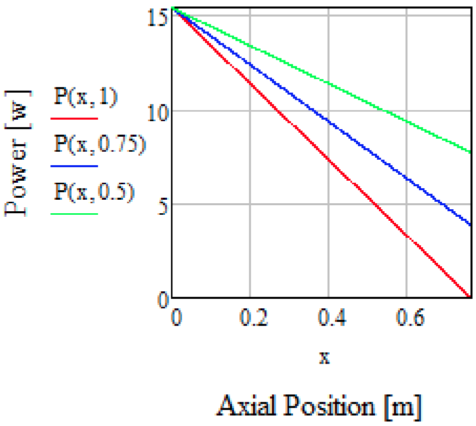

$$\theta(x,\varepsilon,n) := \theta_0 \cdot \sin\left(n \cdot 2\pi \cdot \frac{x}{len} \cdot \frac{S(len,\varepsilon)}{S(x,\varepsilon)}\right)$$

Fin angular displacement relative to leading mast as dictated by wavelength decay.

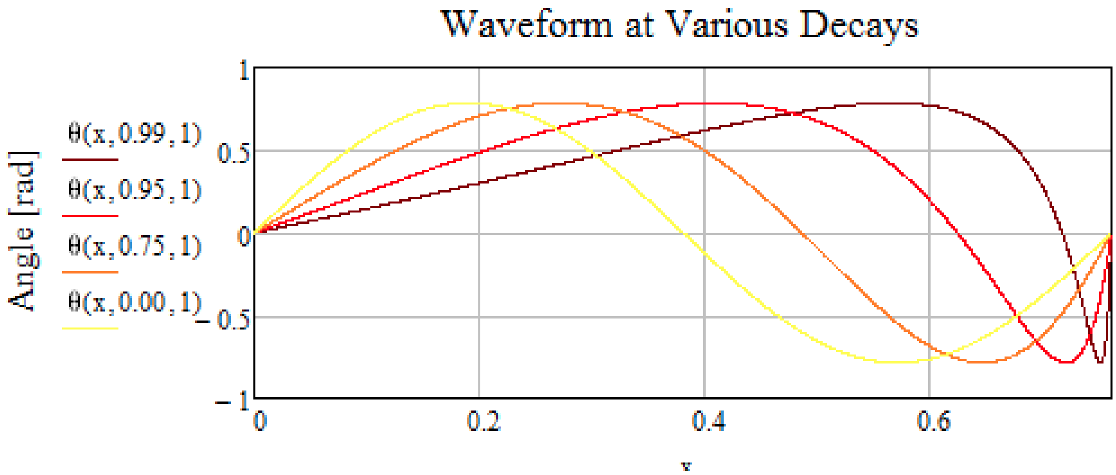
Waveform at Various Decays

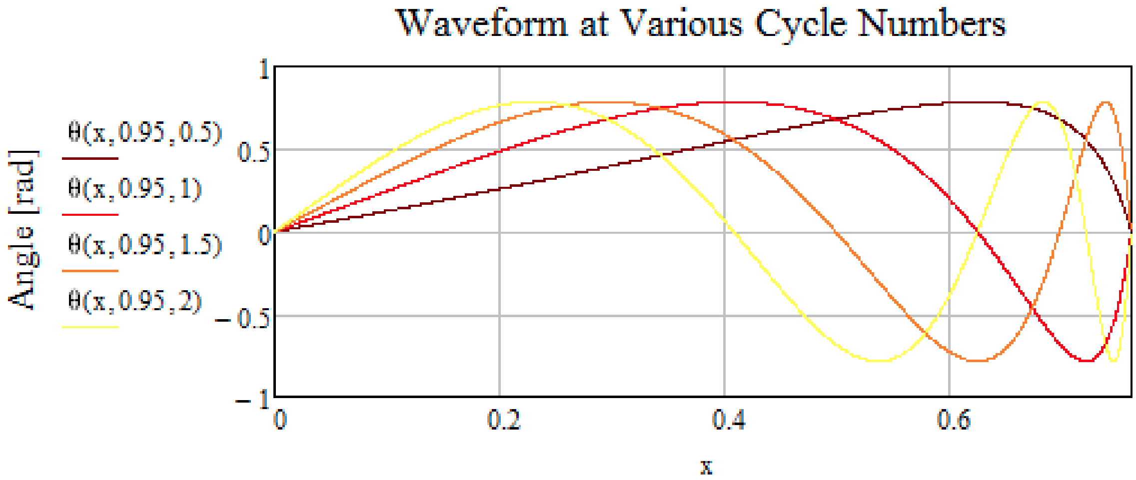
Waveform at Various Cycle Numbers

Axial Position [m]

$r := 0, \frac{r_0}{100} .. r_0$ $\quad$ $\varepsilon := 0, 0.01 .. 1$ $\quad$ $n := 0, 0.1 .. 10$

$$\mathrm{finL}(r, \varepsilon, n) := \int_0^{len} \sqrt{1 + \left(\frac{d}{dx}\theta(x, \varepsilon, n) \cdot r\right)^2}\, dx$$

$$\mathrm{Area}(\varepsilon, n) := \int_0^{r_0} \mathrm{finL}(r, \varepsilon, n)\, dr$$

Appendix D: Data Scatterplots

Hybrid Fin Torque Speed Power Curves

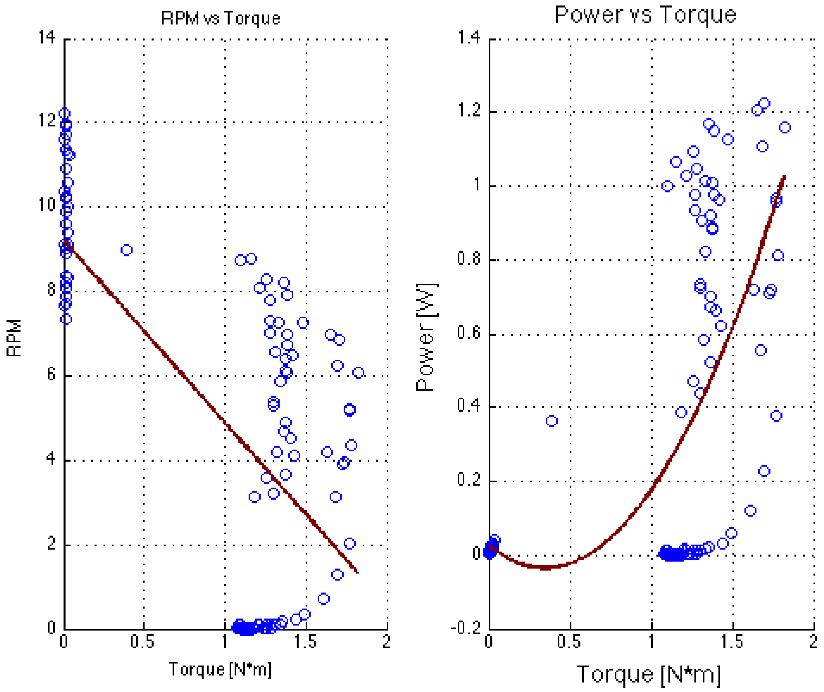

Figure D-1: Flow Speed of 0.331m/s

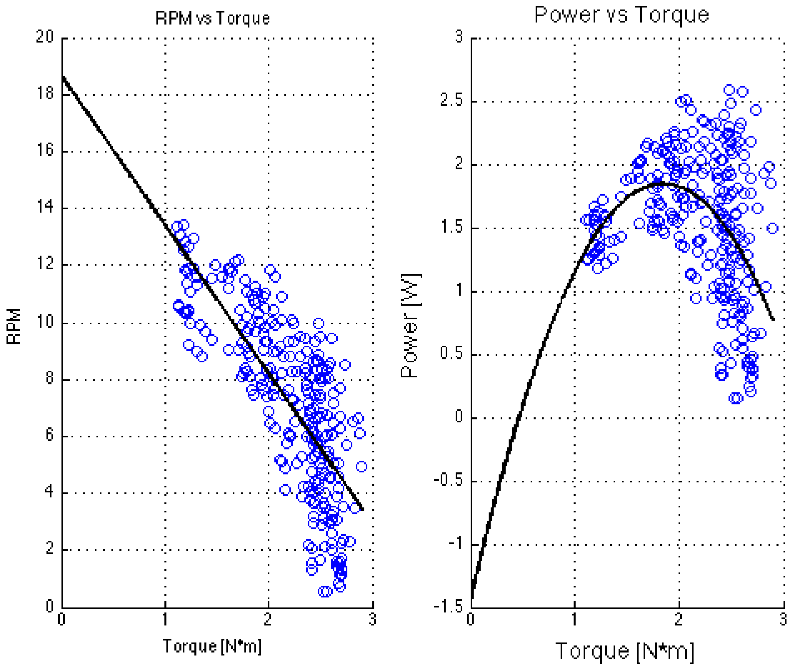

Figure D-2: Flow Speed of 0.403m/s

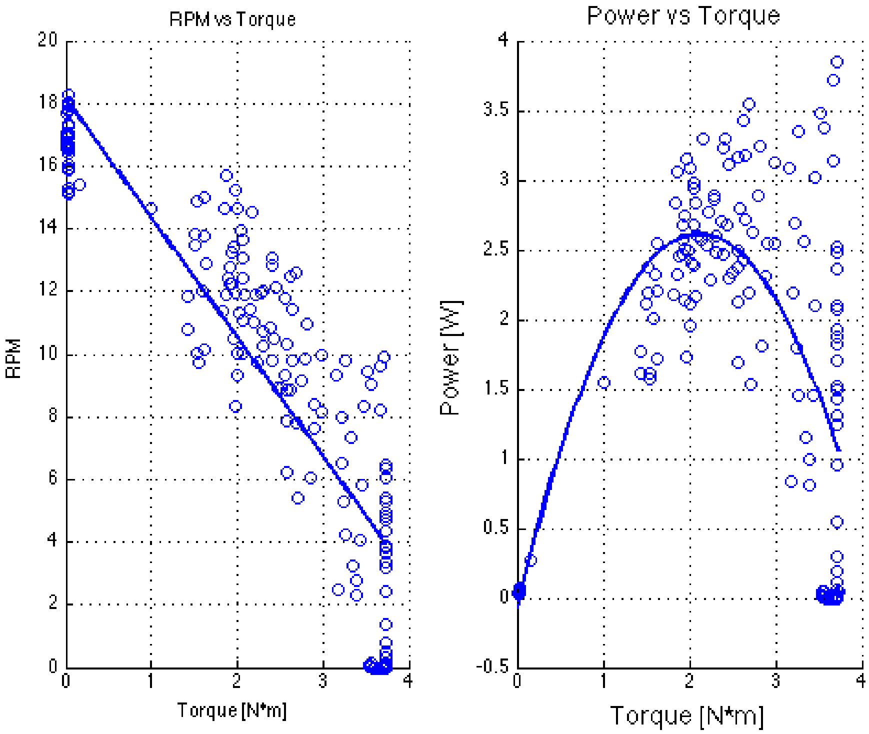

Figure D-3: Flow Speed of 0.533m/s

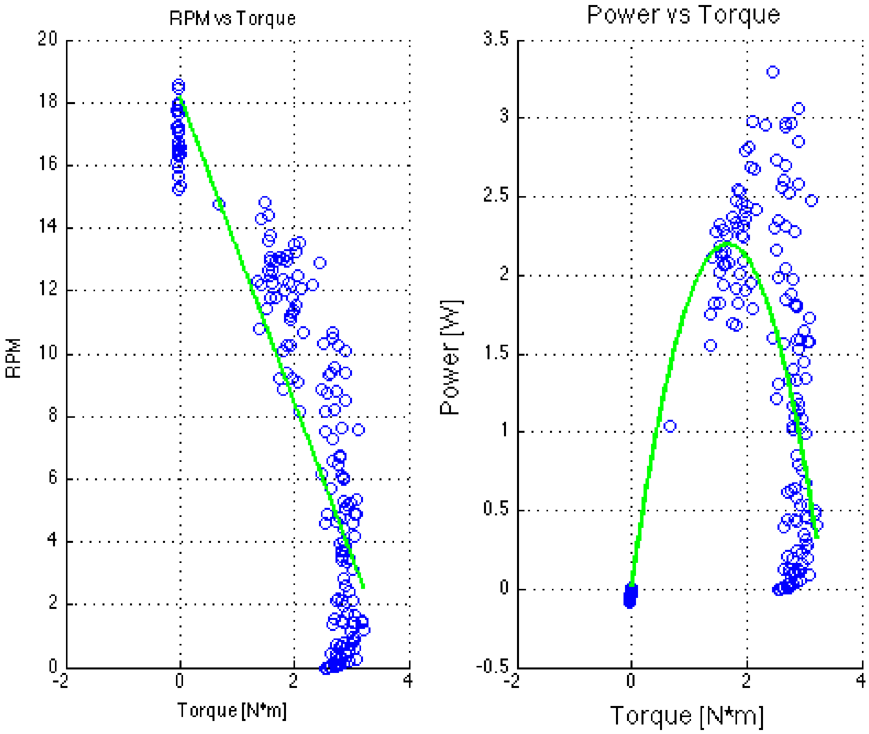

Figure D-4: Flow Speed of 0.619m/s

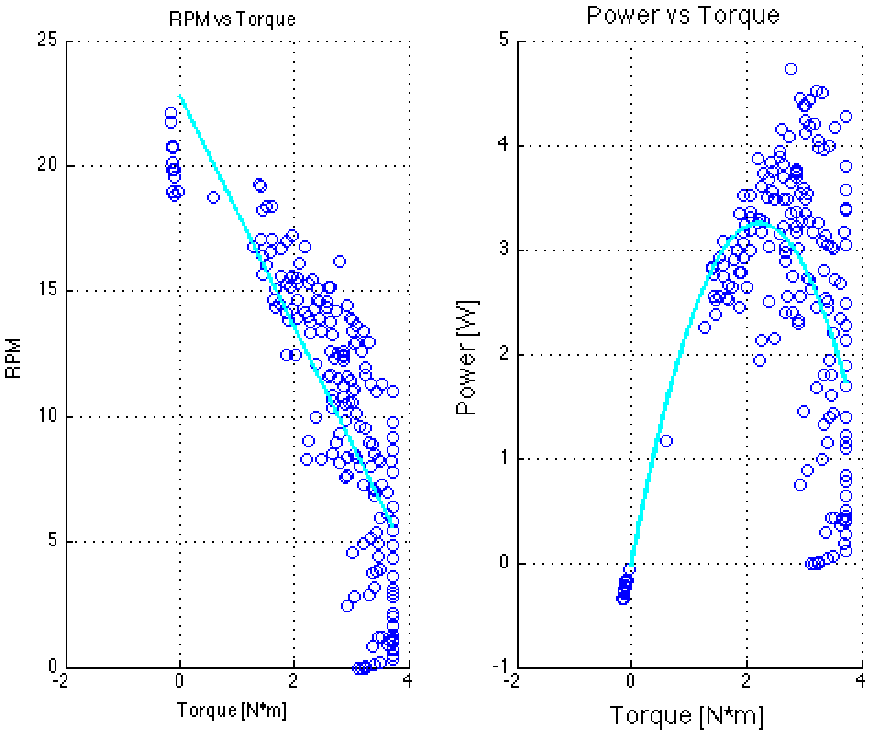

Figure D-5: Flow Speed of 0.703m/s

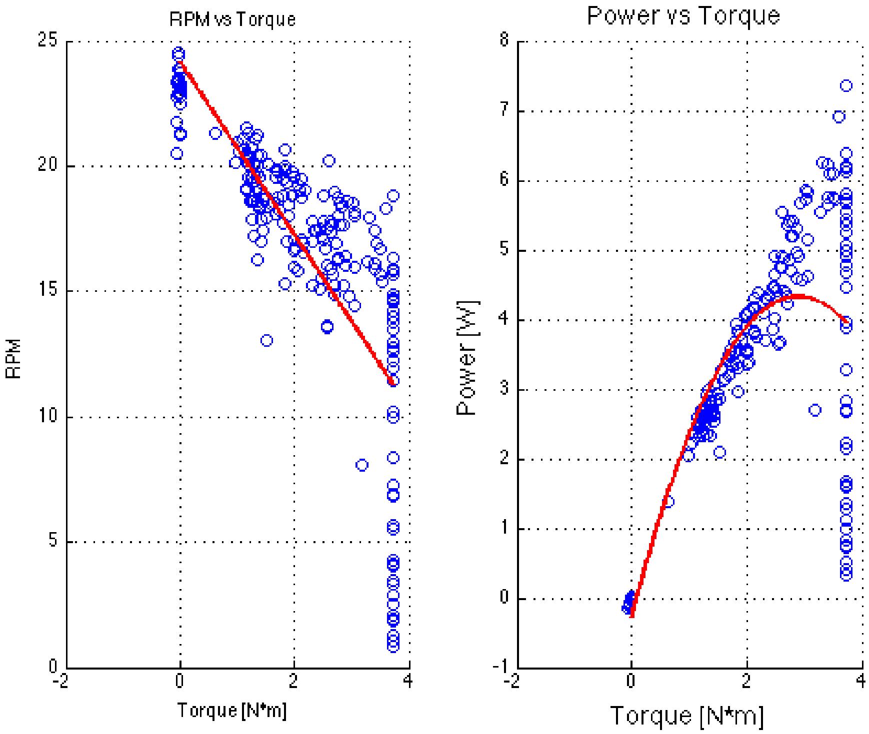

Figure D-6: Flow Speed of 0.769m/s

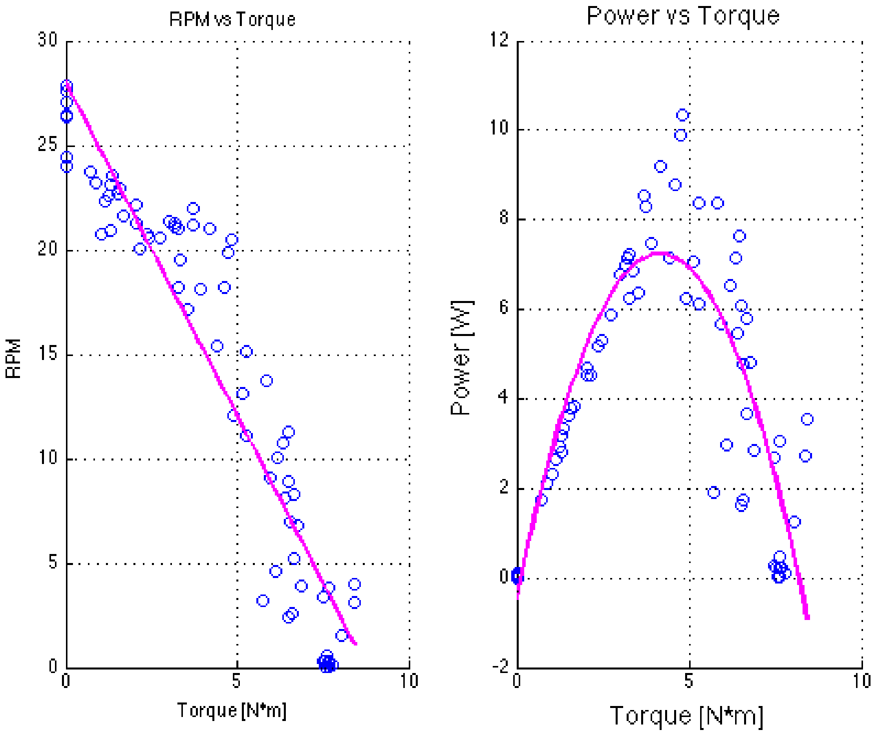

Figure D-7: Flow Speed of 0.896m/s

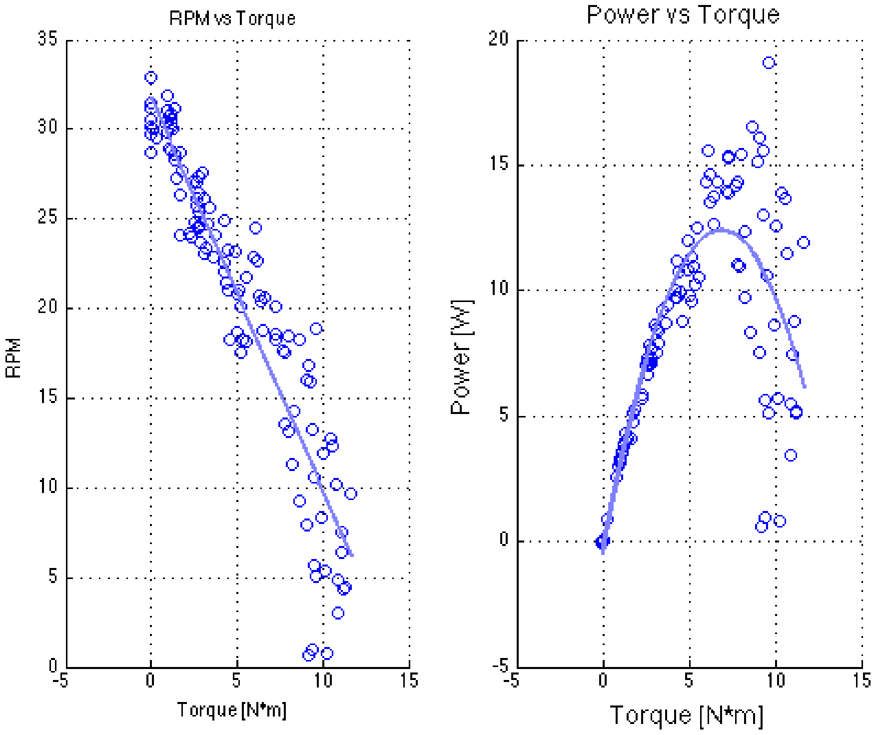

Figure D-8: Flow Speed of 0.970m/s

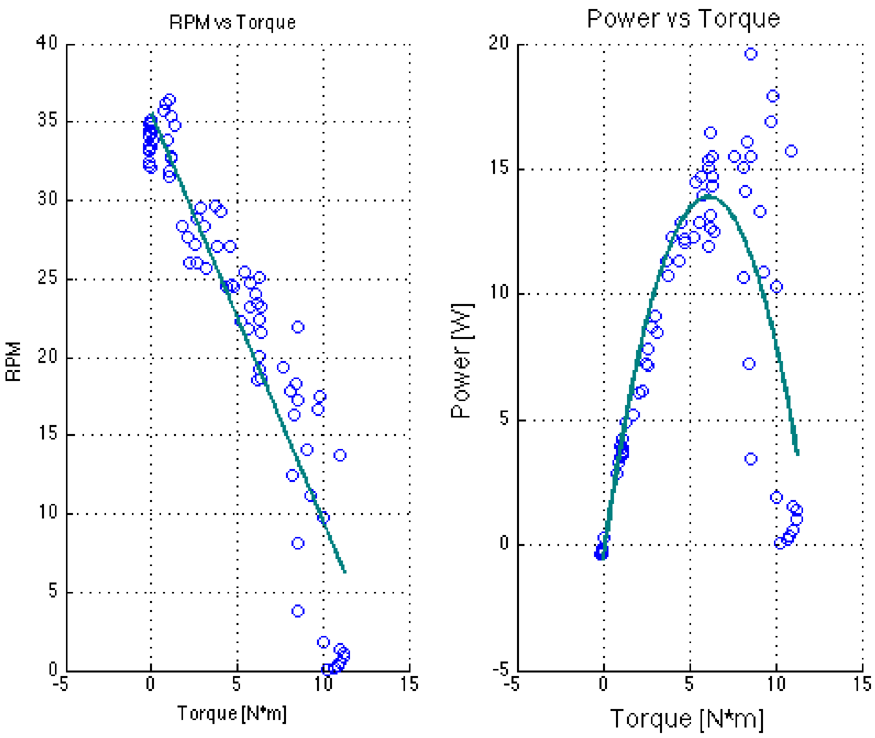

Figure D-9: Flow Speed of 1.230m/s

12” Neoprene Fin Torque Speed Power Curves

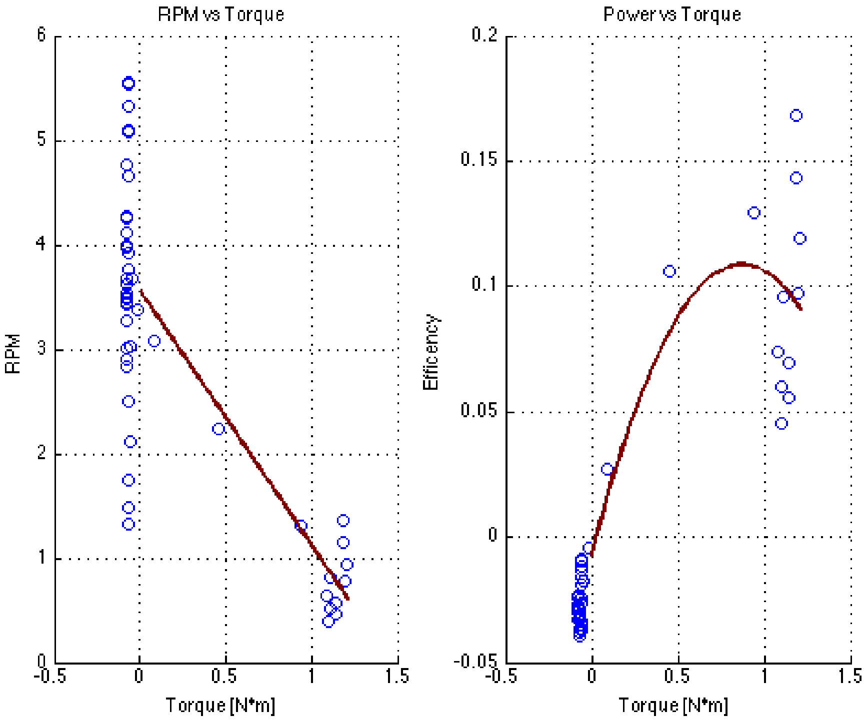

Figure D-10: Flow Speed of 0.233m/s

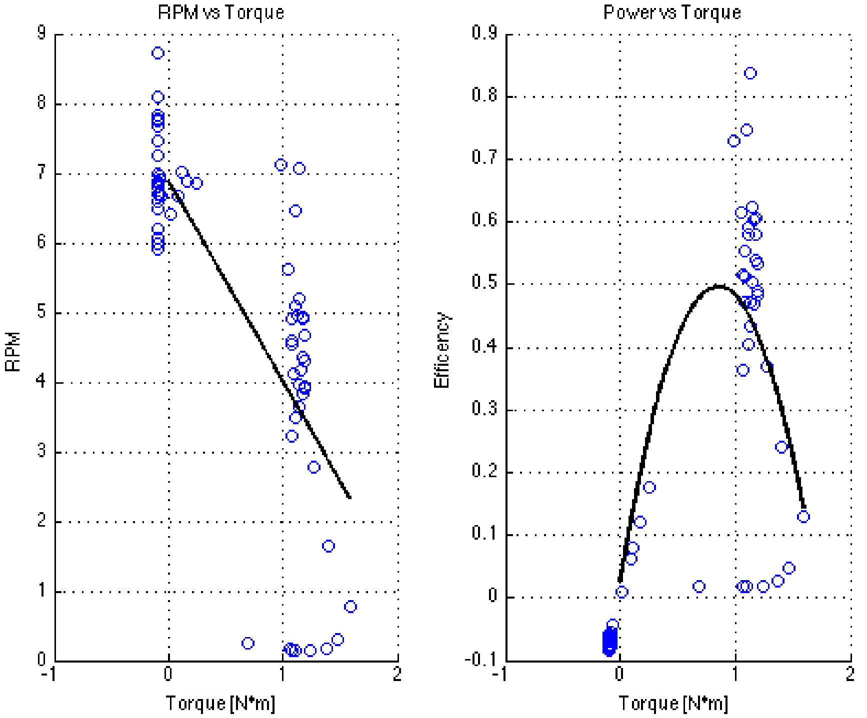

Figure D-11: Flow Speed of 0.311m/s

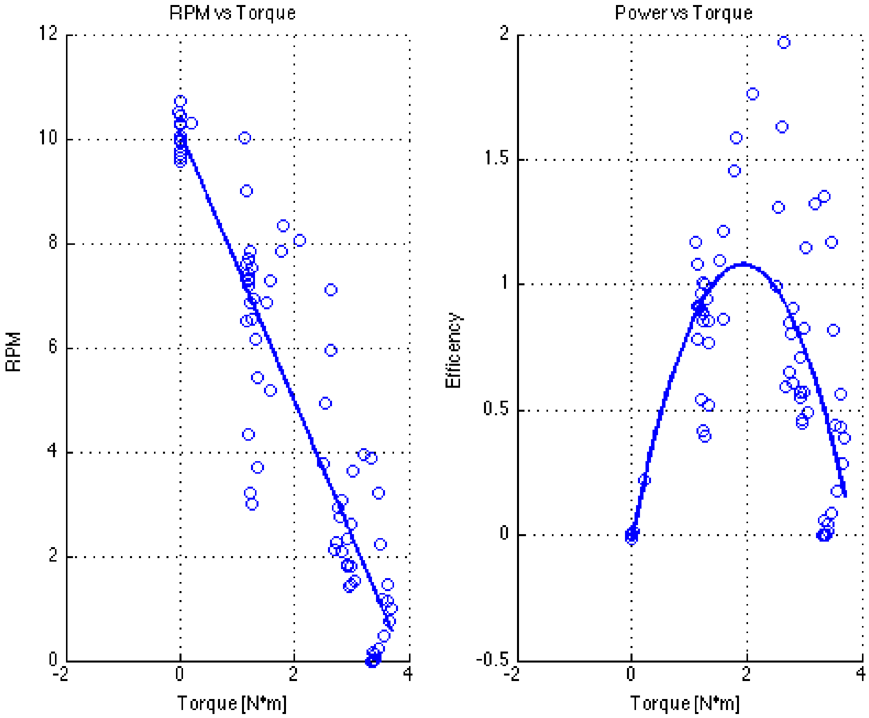

Figure D-12: Flow Speed of 0.399m/s

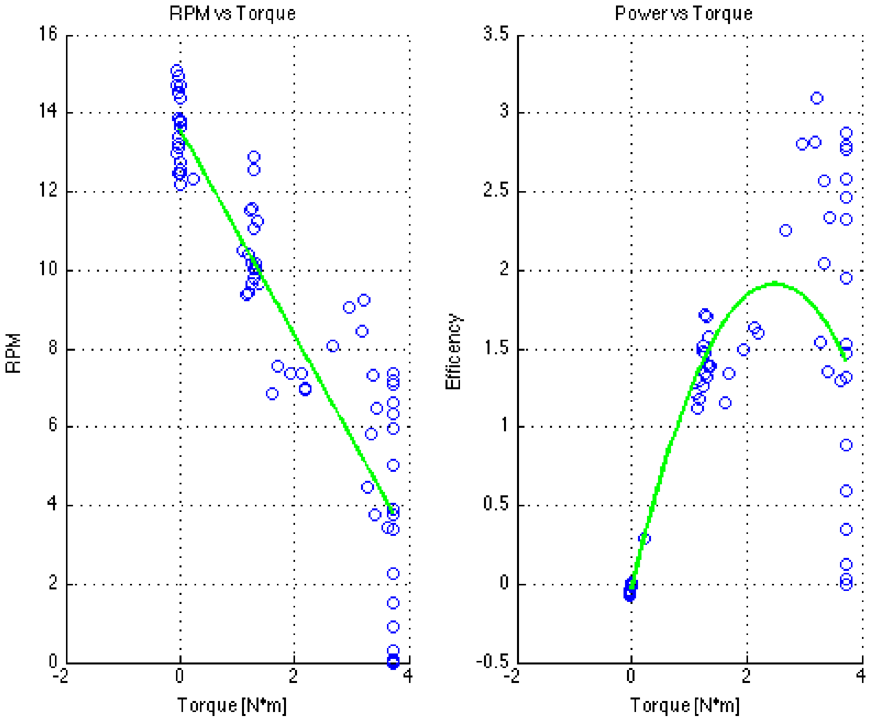

Figure D-13: Flow Speed of 0.488m/s

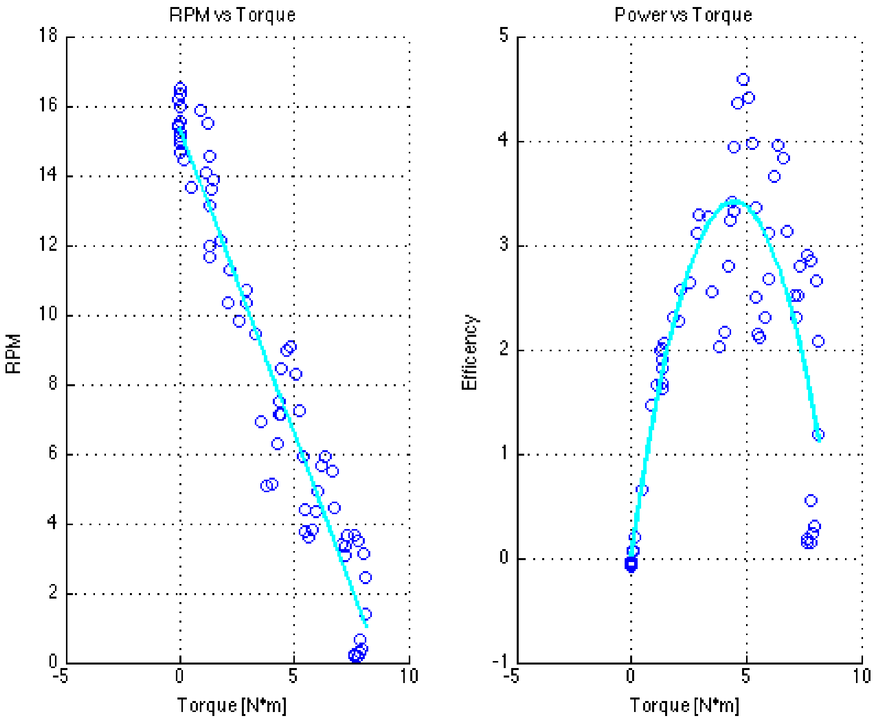

Figure D-14: Flow Speed of 0.578m/s

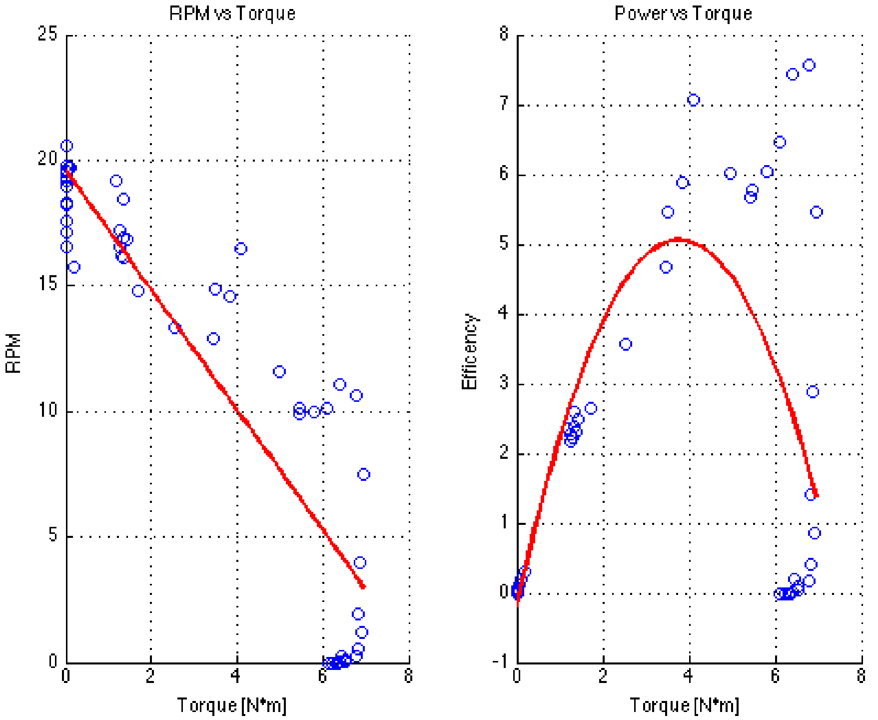

Figure D-15: Flow Speed of 0.640m/s

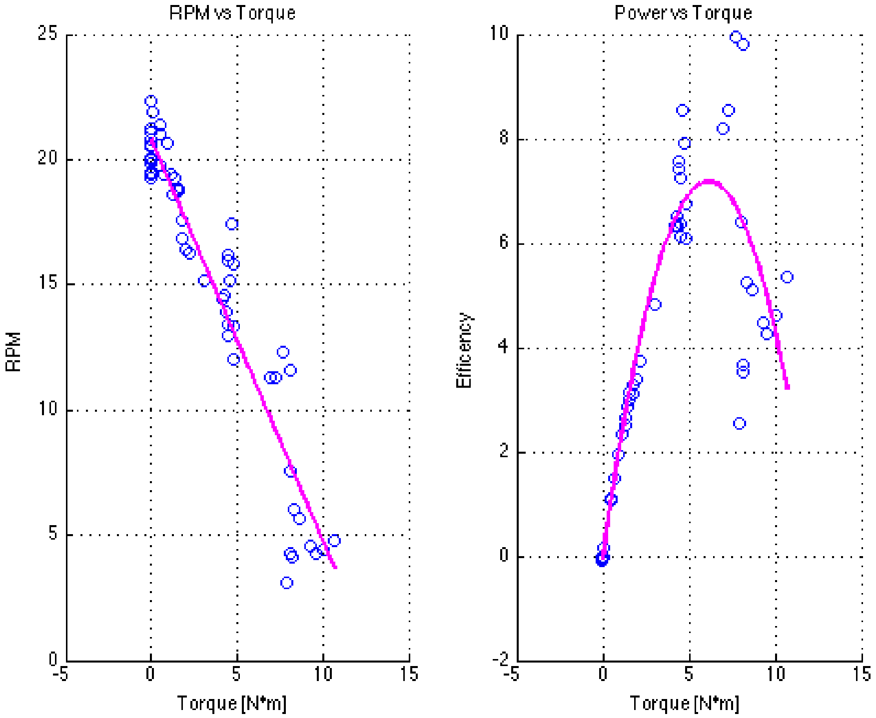

Figure D-16: Flow Speed of 0.855m/s

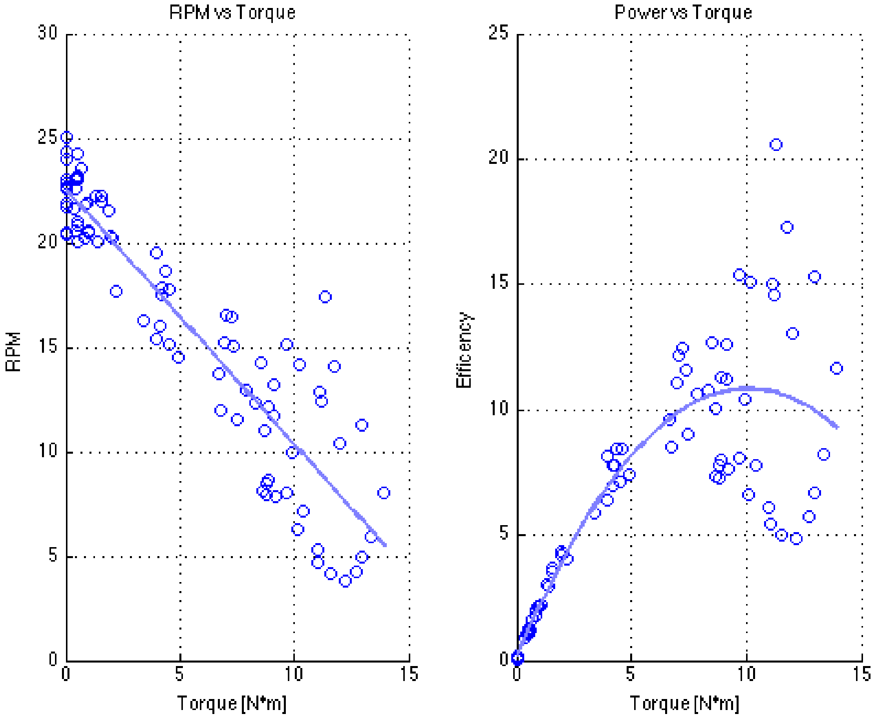

Figure D-17: Flow Speed of 0.969m/s

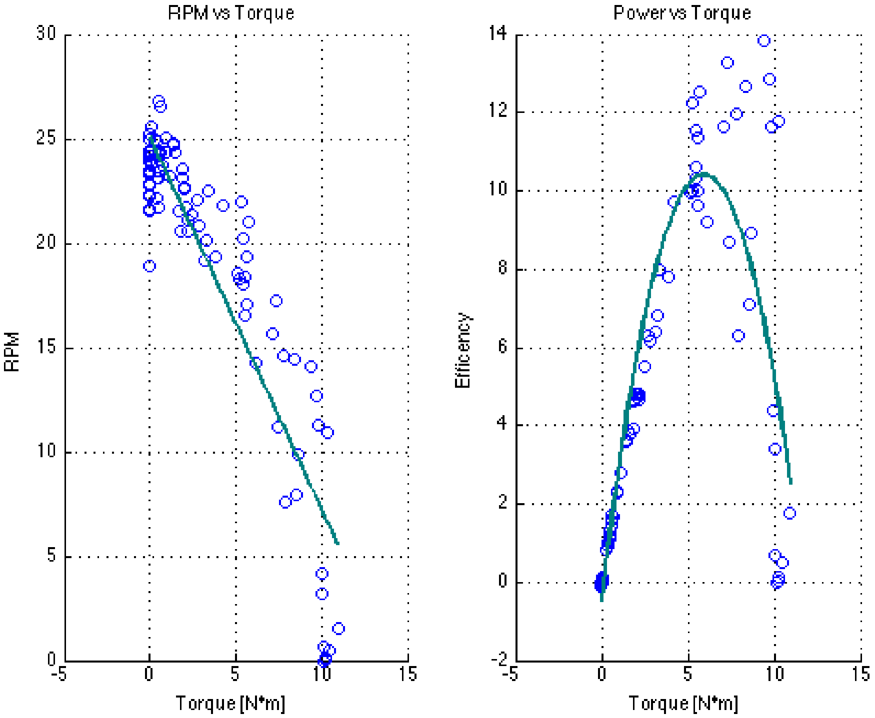

Figure D-18: Flow Speed of 1.08m/s

8” Neoprene Fin Torque Speed Power Curves

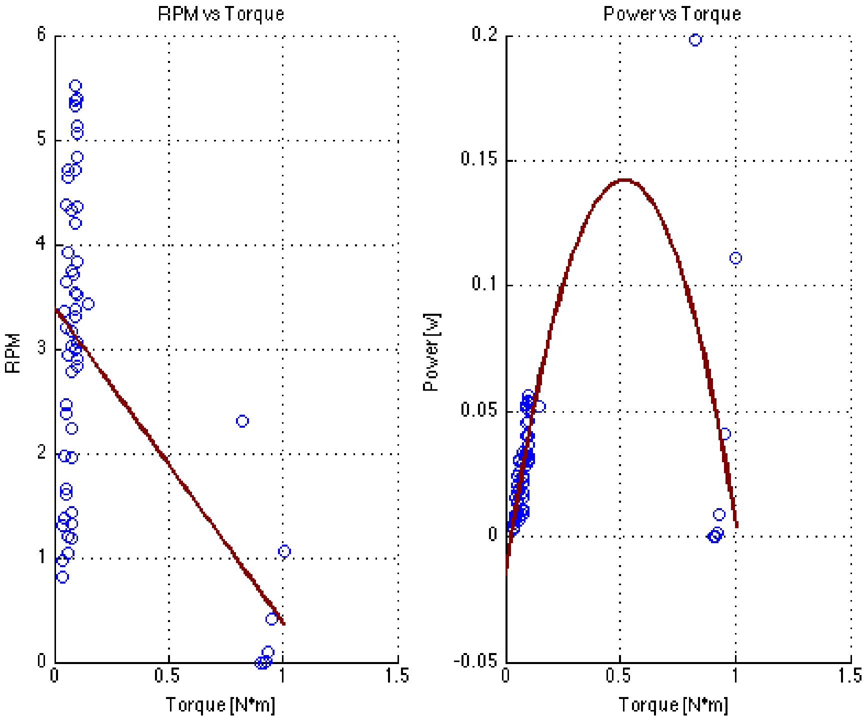

Figure D-19: Flow Speed of 0.252m/s

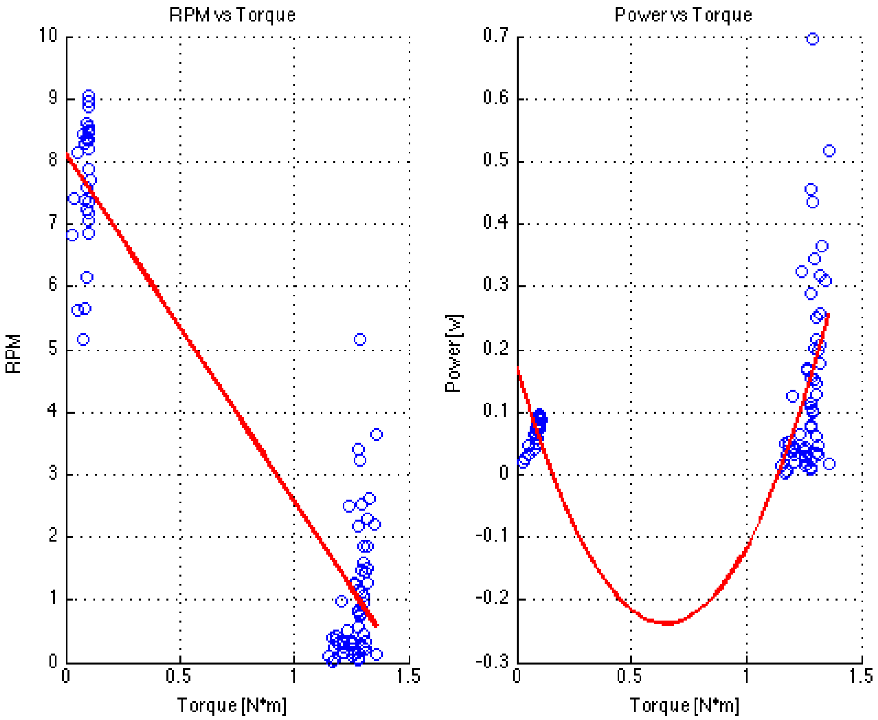

Figure D-20: Flow Speed of 0.366m/s

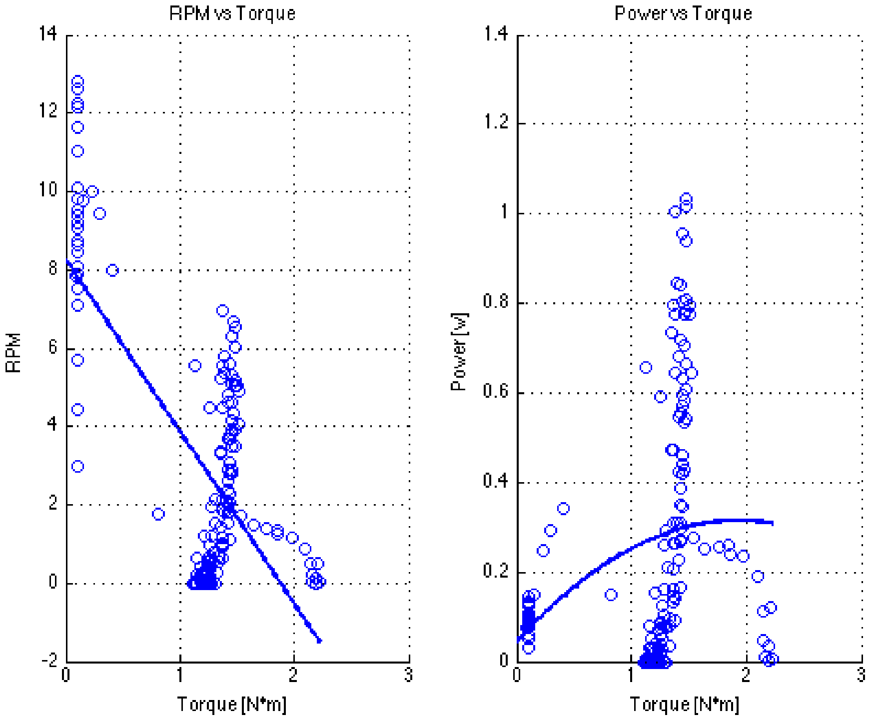

Figure D-21: Flow Speed of 0.433m/s

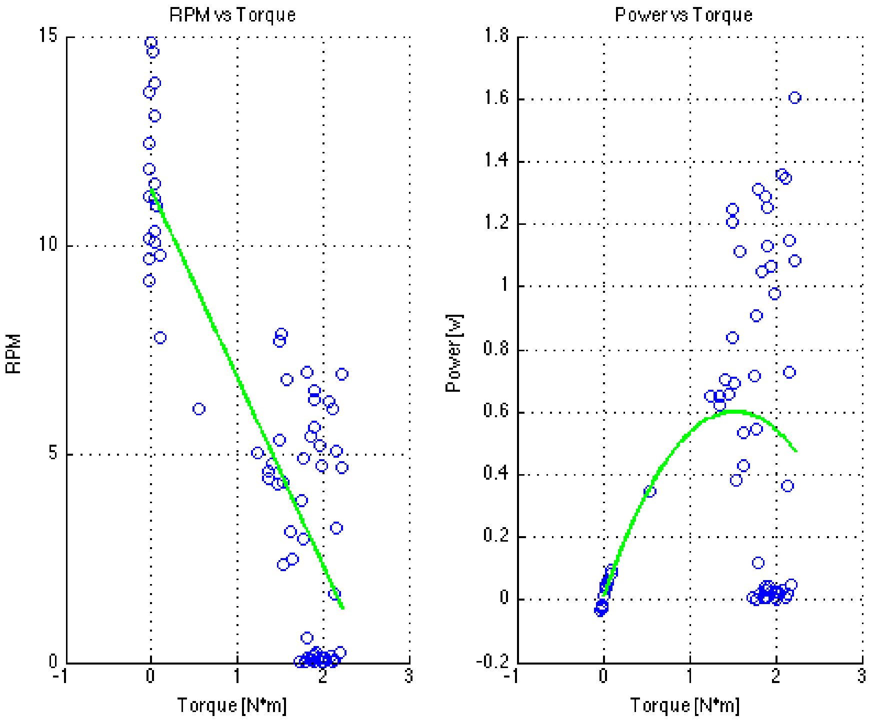

Figure D-22: Flow Speed of 0.543m/s

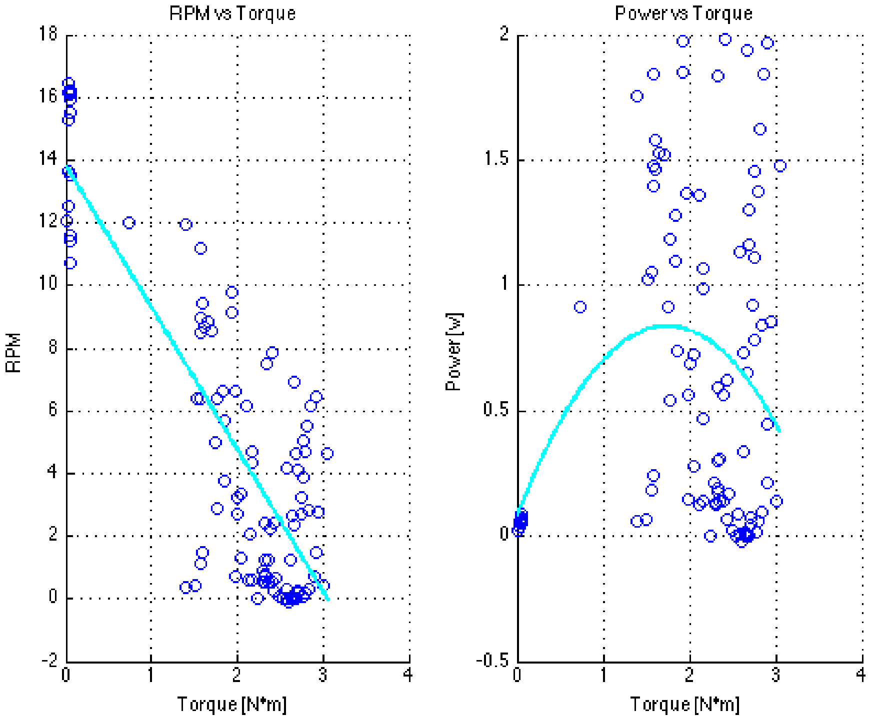

Figure D-23: Flow Speed of 0.635m/s

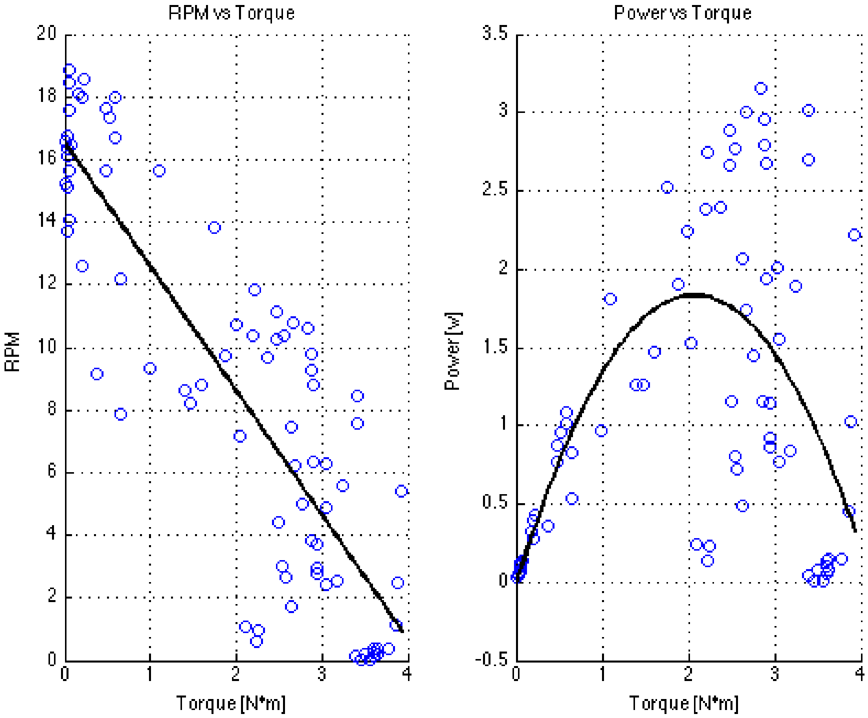

Figure D-24: Flow Speed of 0.683m/s

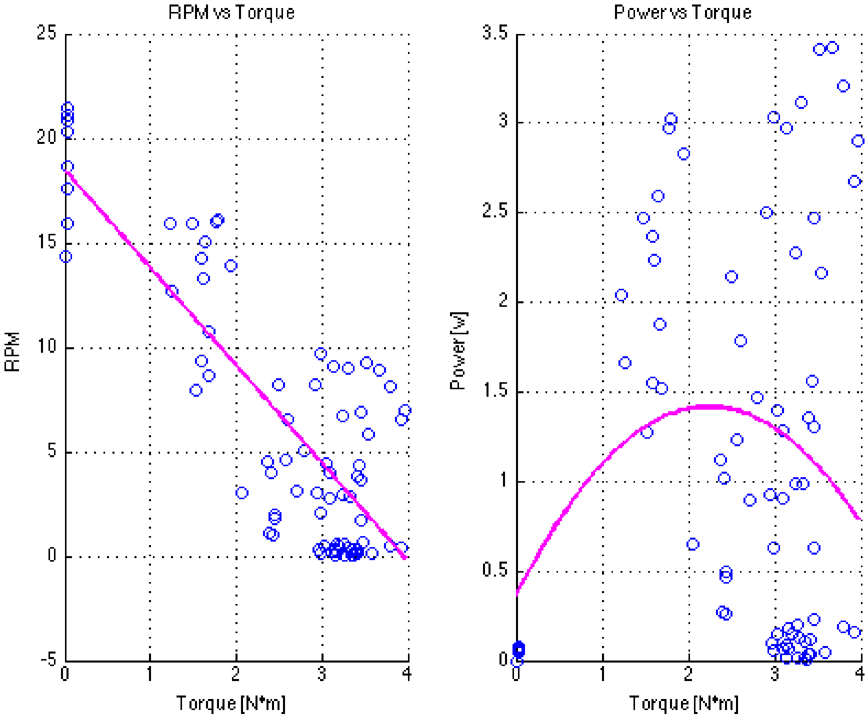

Figure D-25: Flow Speed of 0.789m/s

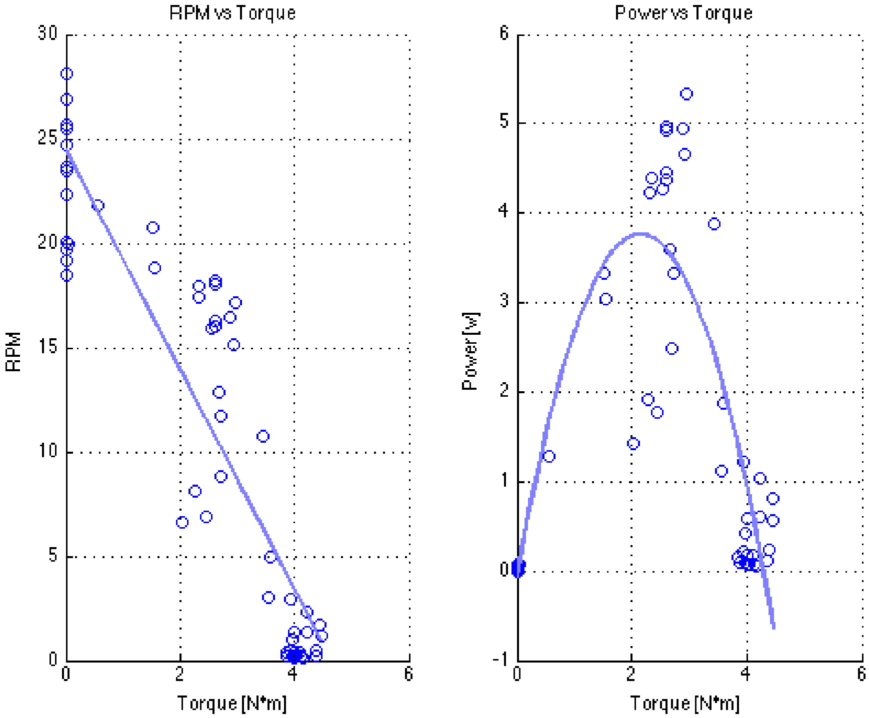

Figure D-26: Flow Speed of 0.880m/s

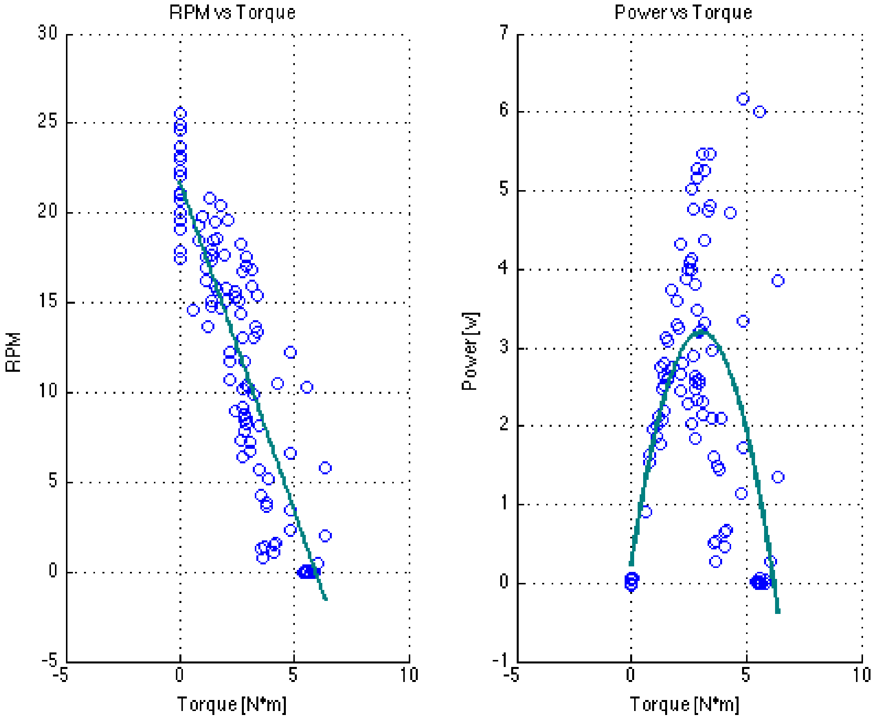

Figure D-27: Flow Speed of 1.08m/s

4” Neoprene Fin Torque Speed Curves

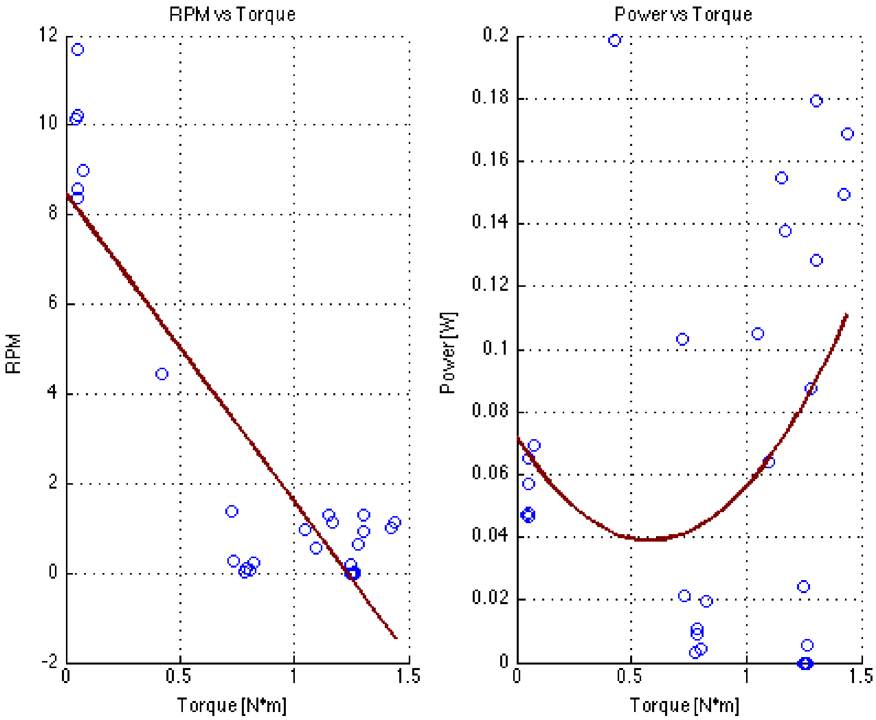

Figure D-28: Flow Speed of .653m/s

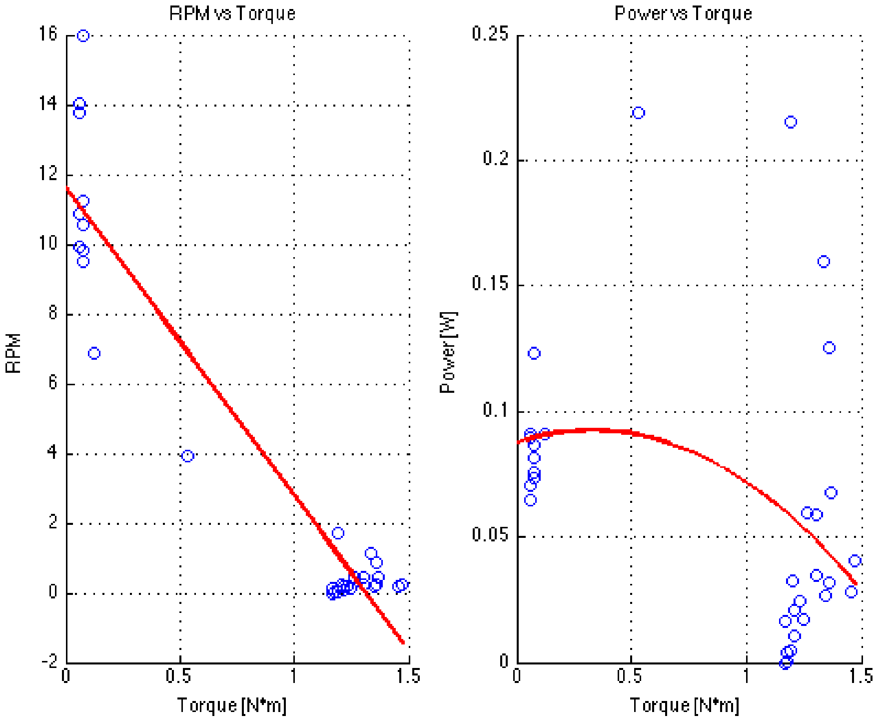

Figure D-29: Flow Speed of 0.791m/s

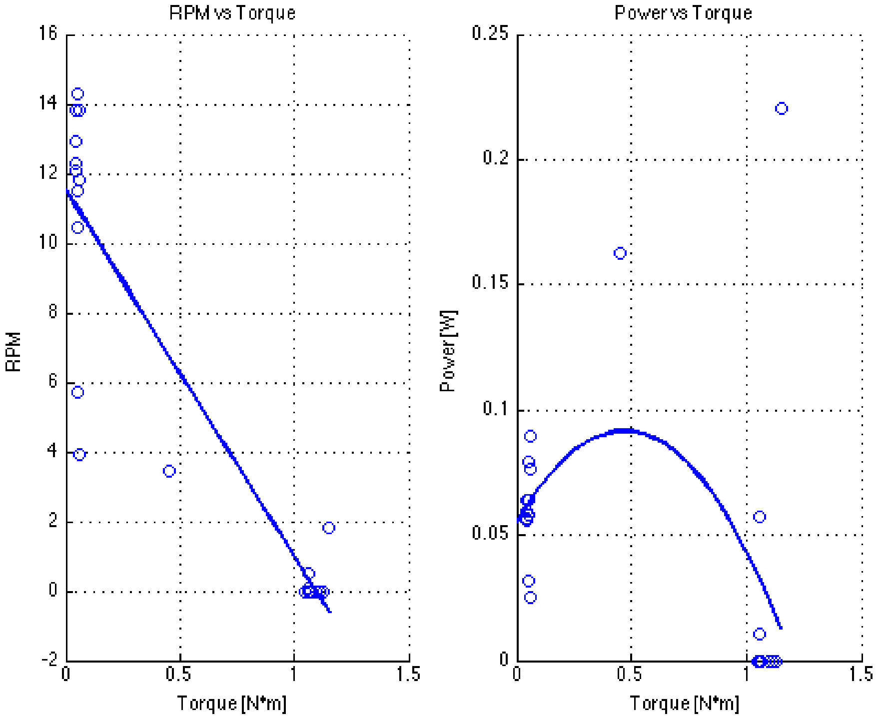

Figure D-30: Flow Speed of 0.918m/s

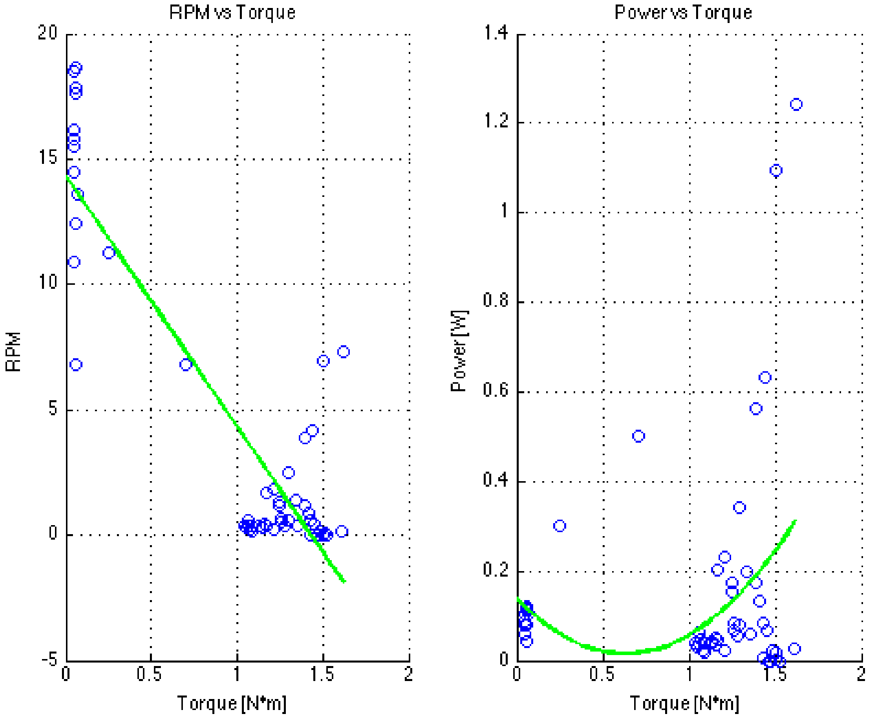

Figure D-31: Flow Speed of 1.012m/s

Hybrid RPM vs Flow Speed Curve

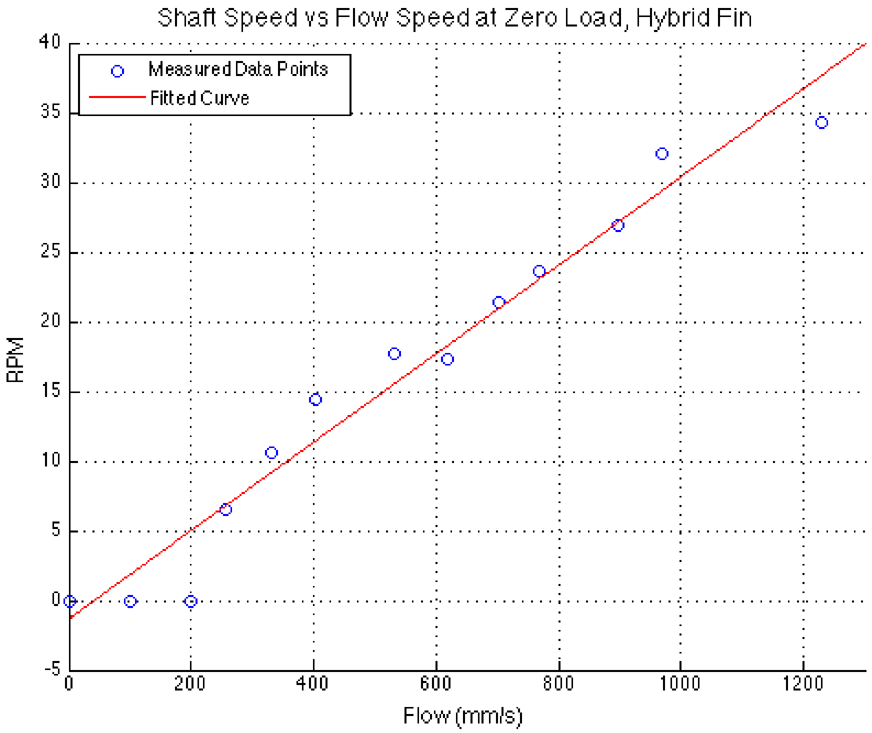

12” Neoprene Fin RPM vs Flow Speed Curve

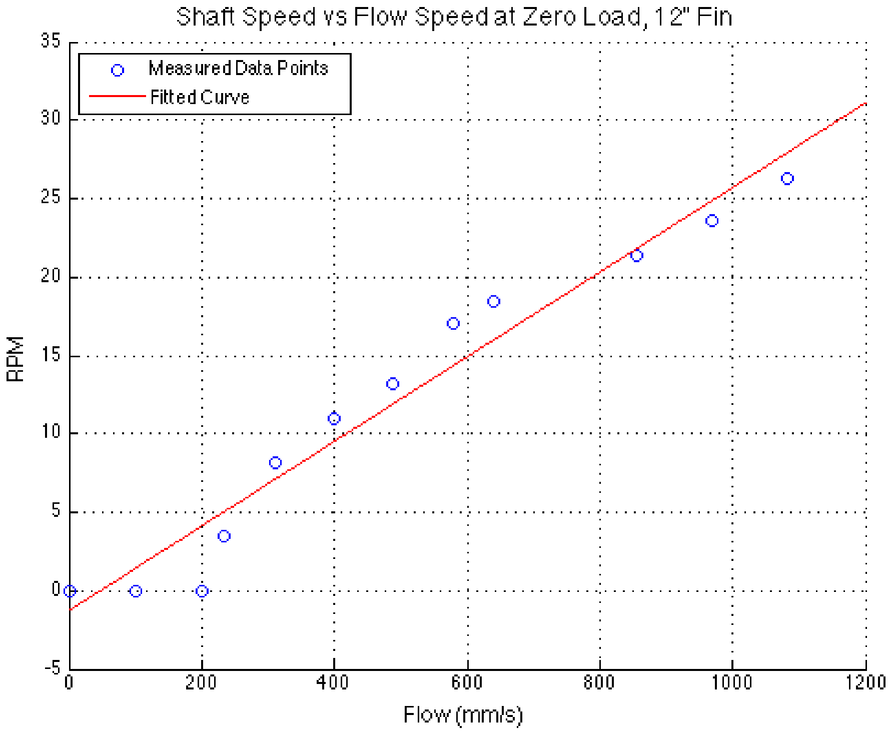

8” Neoprene Fin RPM vs Flow Speed Curve

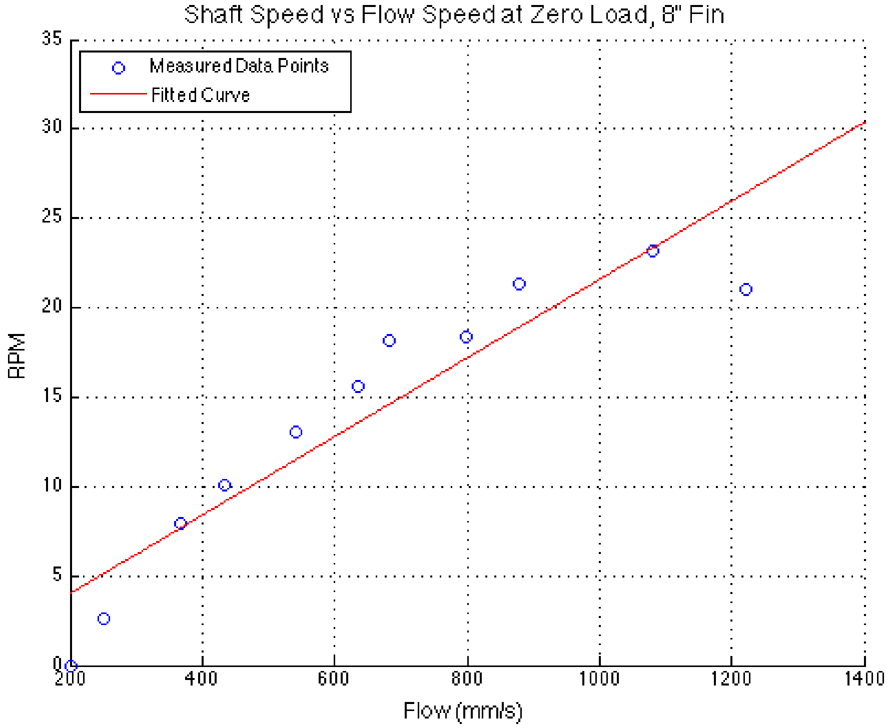

4” Neoprene Fin RPM vs Flow Speed Curve

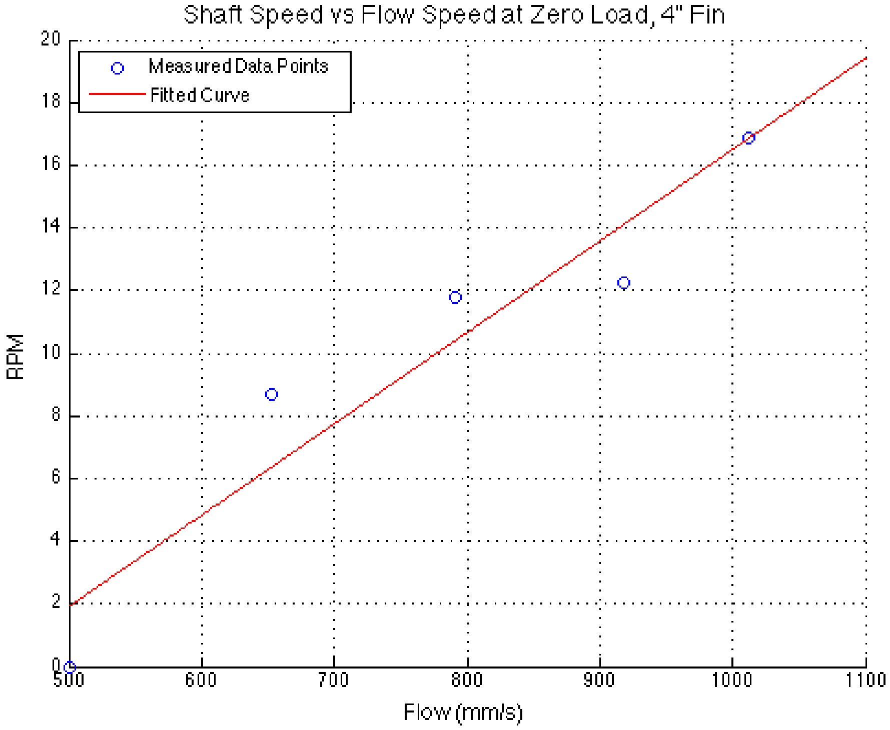

Appendix E: MATLAB Scripts

RPM vs Flow Speed, 8” Neoprene Fin Example

```
%WATER HARVESTING MQP
%Ian Costanzo, Alden Kelsey, Fiona Ogren, David Wians
%Professor Brian Savilonis
%August 2014 - March 2015
% RPM versus Flow
%8" Neoprene Fin

clear all; close all;

%Constants
Flow = [200 252 366 433 542 635 683 798 880 1082 1221]; %Flow Speed [mm/s]
length = length(Flow);
RPM = zeros(1,length);
radius = 0.295; %Radius of dyno wheel [meters]
R1 = 1; %Initial Row
R2 = 180; %Final Row
C1 = 4; %Colume for angular velcity data
C2 = 4;
i = 1;

% Sensor Read Zero RPM for Speeds 0-200mmps
% RPM(i) = 0; %0mmps
% i = i+1;
% RPM(i) = 0; %100mmps
% i = i+1;
RPM(i) = 0; %200mmps
i = i+1;

filename = 'ConstTorque_2015-2-17_252mmps.csv';
samplecount = 180;
sensorangvelocity = csvread(filename,R1,C2,[R1 C2 R2 C2]); %File Read from
Rotational Sensor
avgsensorvelocity = sum(sensorangvelocity)./samplecount; %Average sensor
velocity
angvelratio = 29.2/47.8; %Ratio to account for radius difference
angvelocity = sensorangvelocity.*angvelratio; %Corrected angular velocty
avgangvelocity = sum(angvelocity)./samplecount; %Average angular velocity
rpm = 9.5493.*angvelocity; %Convert to RPM
avgrpm = sum(rpm)./samplecount; %revolutions/minute
SD(i) = std(angvelocity);
RPM(i) = avgrpm;
i = i+1;

filename = 'ConstTorque_2015-2-17_366mmps.csv';
samplecount = 180;
sensorangvelocity = csvread(filename,R1,C2,[R1 C2 R2 C2]); %File Read from
Rotational Sensor
avgsensorvelocity = sum(sensorangvelocity)./samplecount; %Average sensor
velocity
angvelratio = 29.2/47.8; %Ratio to account for radius difference
angvelocity = sensorangvelocity.*angvelratio; %Corrected angular velocty
avgangvelocity = sum(angvelocity)./samplecount; %Average angular velocity
```

```
rpm = 9.5493.*angvelocity; %Convert to RPM
avgrpm = sum(rpm)./samplecount; %revolutions/minute
SD(i) = std(angvelocity);
RPM(i) = avgrpm;
i = i+1;

filename = 'ConstTorque_2015-2-17_433mmps.csv';
samplecount = 180;
sensorangvelocity = csvread(filename,R1,C2,[R1 C2 R2 C2]); %File Read from
Rotational Sensor
avgsensorvelocity = sum(sensorangvelocity)./samplecount; %Average sensor
velocity
angvelratio = 29.2/47.8; %Ratio to account for radius difference
angvelocity = sensorangvelocity.*angvelratio; %Corrected angular velocty
avgangvelocity = sum(angvelocity)./samplecount; %Average angular velocity
rpm = 9.5493.*angvelocity; %Convert to RPM
avgrpm = sum(rpm)./samplecount; %revolutions/minute
SD(i) = std(angvelocity);
RPM(i) = avgrpm;
i = i+1;

filename = 'ConstTorque_2015-2-17_542mmps.csv';
samplecount = 180;
sensorangvelocity = csvread(filename,R1,C2,[R1 C2 R2 C2]); %File Read from
Rotational Sensor
avgsensorvelocity = sum(sensorangvelocity)./samplecount; %Average sensor
velocity
angvelratio = 29.2/47.8; %Ratio to account for radius difference
angvelocity = sensorangvelocity.*angvelratio; %Corrected angular velocty
avgangvelocity = sum(angvelocity)./samplecount; %Average angular velocity
rpm = 9.5493.*angvelocity; %Convert to RPM
avgrpm = sum(rpm)./samplecount; %revolutions/minute
SD(i) = std(angvelocity);
RPM(i) = avgrpm;
i = i+1;

filename = 'ConstTorque_2015-2-17_635mmps.csv';
samplecount = 180;
sensorangvelocity = csvread(filename,R1,C2,[R1 C2 R2 C2]); %File Read from
Rotational Sensor
avgsensorvelocity = sum(sensorangvelocity)./samplecount; %Average sensor
velocity
angvelratio = 29.2/47.8; %Ratio to account for radius difference
angvelocity = sensorangvelocity.*angvelratio; %Corrected angular velocty
avgangvelocity = sum(angvelocity)./samplecount; %Average angular velocity
rpm = 9.5493.*angvelocity; %Convert to RPM
avgrpm = sum(rpm)./samplecount; %revolutions/minute
SD(i) = std(angvelocity);
RPM(i) = avgrpm;
i = i+1;

filename = 'ConstTorque_2015-2-17_683mmps.csv';
samplecount = 180;
sensorangvelocity = csvread(filename,R1,C2,[R1 C2 R2 C2]); %File Read from
Rotational Sensor
```

```
avgsensorvelocity = sum(sensorangvelocity)./samplecount; %Average sensor
velocity
angvelratio = 29.2/47.8; %Ratio to account for radius difference
angvelocity = sensorangvelocity.*angvelratio; %Corrected angular velocty
avgangvelocity = sum(angvelocity)./samplecount; %Average angular velocity
rpm = 9.5493.*angvelocity; %Convert to RPM
avgrpm = sum(rpm)./samplecount; %revolutions/minute
SD(i) = std(angvelocity);
RPM(i) = avgrpm;
i = i+1;

filename = 'ConstTorque_2015-2-17_798mmps.csv';
samplecount = 180;
sensorangvelocity = csvread(filename,R1,C2,[R1 C2 R2 C2]); %File Read from
Rotational Sensor
avgsensorvelocity = sum(sensorangvelocity)./samplecount; %Average sensor
velocity
angvelratio = 29.2/47.8; %Ratio to account for radius difference
angvelocity = sensorangvelocity.*angvelratio; %Corrected angular velocty
avgangvelocity = sum(angvelocity)./samplecount; %Average angular velocity
rpm = 9.5493.*angvelocity; %Convert to RPM
avgrpm = sum(rpm)./samplecount; %revolutions/minute
SD(i) = std(angvelocity);
RPM(i) = avgrpm;
i = i+1;

filename = 'ConstTorque_2015-2-17_880mmps.csv';
samplecount = 180;
sensorangvelocity = csvread(filename,R1,C2,[R1 C2 R2 C2]); %File Read from
Rotational Sensor
avgsensorvelocity = sum(sensorangvelocity)./samplecount; %Average sensor
velocity
angvelratio = 29.2/47.8; %Ratio to account for radius difference
angvelocity = sensorangvelocity.*angvelratio; %Corrected angular velocty
avgangvelocity = sum(angvelocity)./samplecount; %Average angular velocity
rpm = 9.5493.*angvelocity; %Convert to RPM
avgrpm = sum(rpm)./samplecount; %revolutions/minute
SD(i) = std(angvelocity);
RPM(i) = avgrpm;
i = i+1;

filename = 'ConstTorque_2015-2-17_1082mmps.csv';
samplecount = 180;
sensorangvelocity = csvread(filename,R1,C2,[R1 C2 R2 C2]); %File Read from
Rotational Sensor
avgsensorvelocity = sum(sensorangvelocity)./samplecount; %Average sensor
velocity
angvelratio = 29.2/47.8; %Ratio to account for radius difference
angvelocity = sensorangvelocity.*angvelratio; %Corrected angular velocty
avgangvelocity = sum(angvelocity)./samplecount; %Average angular velocity
rpm = 9.5493.*angvelocity; %Convert to RPM
avgrpm = sum(rpm)./samplecount; %revolutions/minute
SD(i) = std(angvelocity);
RPM(i) = avgrpm;
i = i+1;
```

```
filename = 'ConstTorque_2015-2-17_1221mmps.csv';
samplecount = 180;
sensorangvelocity = csvread(filename,R1,C2,[R1 C2 R2 C2]); %File Read from Rotational Sensor
avgsensorvelocity = sum(sensorangvelocity)./samplecount; %Average sensor velocity
angvelratio = 29.2/47.8; %Ratio to account for radius difference
angvelocity = sensorangvelocity.*angvelratio; %Corrected angular velocty
avgangvelocity = sum(angvelocity)./samplecount; %Average angular velocity
rpm = 9.5493.*angvelocity; %Convert to RPM
avgrpm = sum(rpm)./samplecount; %revolutions/minute
SD(i) = std(angvelocity);
RPM(i) = avgrpm;
%Plot

Flow = Flow';
RPM = RPM';

%Plot
hold on;
scatter(Flow,RPM);
h = fit(Flow,RPM,'poly1')
plot(h);
grid on;
xlabel('Flow (mm/s)','FontSize',12);
ylabel('RPM','FontSize',12)
title('Shaft Speed vs Flow Speed at Zero Load, 8" Fin','FontSize',14);
legend('Measured Data Points','Fitted Curve','Location','NorthWest');
```

Torque Speed Power Curves, 12" Neoprene Fin Example

```
%WATER HARVESTING MQP
%Ian Costanzo, Alden Kelsey, Fiona Ogren, David Wians
%Professor Brian Savilonis
%August 2014 - March 2015
%Torque Speed Power Curves
%12" Neoprene Fin

clear all; close all;

%Constants
radius = 0.295; %Radius of dyno wheel [meters]
lamda = 0.7315 %Wavelength of fin [meters]
rho = 1000; % Density of water [kg/m^3]
theta = pi/2; % Angle of sweep [rad]
r = .3048; % Radius of fin [meters]
A = theta/2*r^2; %Xsection of Flow [m^2]
R1 = 1; %Initial row for CSV call
C1 = 2; %Column for force sensor data
C2 = 4; %Column for angular velocity data
colorcell = [0.502 0 0; 0 0 0; 0 0 1; 0 1 0; 0 1 1;...
            1 0 0; 1 0 1; 0.502 0.502 1; 0 0.502 0.502; 0 0.251 0];
file = {'VaryTorque_2015-2-13_0233mmps.csv';...
    'VaryTorque_2015-2-13_0311mmps.csv'; ...
    'VaryTorque_2015-2-13_0399mmps.csv';...
    'VaryTorque_2015-2-13_0488mmps.csv'; ...
    'VaryTorque_2015-2-13_0578mmps.csv';...
    'VaryTorque_2015-2-13_0640mmps.csv'; ...
    'VaryTorque_2015-2-13_0855mmps.csv';...
    'VaryTorque_2015-2-13_0969mmps.csv'; ...
    'VaryTorque_2015-2-13_1083mmps.csv';};
V = [.233 .311 .399 .488 .578 .640 .855 .969 1.083]; %Measured Flow Speed
cellsize = size(file);
i = cellsize(1);

while i > 0
filename = file(i);
filename = char(filename);
M = csvread(filename,R1,C1);
sizeM = size(M);
R2 = sizeM(1);
%Torque
force = csvread(filename,R1,C1,[R1 C1 R2 C1]); %Measured force [N]
torque = radius.*force; %Shaft torque [N*m]
%RPM
sensorangvelocity = csvread(filename,R1,C2,[R1 C2 R2 C2]); %Measured omega
angvelratio = 29.2/47.8; %Ratio to account for radius difference
angvelocity = sensorangvelocity.*angvelratio; %Shaft omega
rpm = 9.5493.*angvelocity;
%Power
power = torque.* angvelocity; %Watts

color = colorcell(i,:);

figure(i)
```

```
%Plot Torque RPM
subplot(1,2,1)
hold on
scatter (torque,rpm);
P = polyfit(torque,rpm,1); %Best Fit Torque Curve
N = length(torque);
M = max(torque);
x1 = linspace(0,M,N);
rpmfit = polyval(P,x1);
plot(x1,rpmfit,'color',color,'LineWidth',2);
ylabel('RPM');
xlabel('Torque [N*m]');
title('RPM vs Torque');
grid on;

%Plot Torque Power
subplot(1,2,2)
hold on
scatter (torque, power);
H = polyfit(torque,power,2); %Best Fit Power Curve
powerfit = polyval(H,x1);
plot(x1,powerfit,'color',color,'LineWidth',2);
ylabel('Power [W]');
xlabel('Torque [N*m]');
title('Power vs Torque');
grid on;

figure(11)
%Plot Torque vs RPM
subplot (1,2,1)
hold on;
grid on;
plot(x1,rpmfit,'color',color,'LineWidth',2);
ylabel('RPM','FontSize',14);
xlabel('Torque [N*m]','FontSize',14);
title('RPM vs Torque','FontSize',14);
axis([0 15 0 25]);
set(gca,'xTick',0:15)

Legend=cell(i,1);%  two positions
 Legend{1}='1.08m/s';
 Legend{2}='0.969m/s';
 Legend{3}='0.855m/s';
 Legend{4}='0.640m/s';
 Legend{5}='0.578m/s';
 Legend{6}='0.488m/s';
 Legend{7}='0.399m/s';
 Legend{8}='0.311m/s';
 Legend{9}='0.233m/s';
legend(Legend,'FontSize',14);

%Plot Torque vs Power
subplot (1,2,2)
hold on;
grid on;
plot(x1,powerfit,'color',color,'LineWidth',2);
```

```
ylabel('Power [W]','FontSize',14);
xlabel('Torque [N*m]','FontSize',14);
title('Power vs Torque','FontSize',14);
axis([0 15 0 11]);
set(gca,'xTick',0:15)
set(gca,'yTick',0:11)

i = i-1;
end
```

Wave Speed Plot, 12” Neoprene Fin Example

```
%WATER HARVESTING MQP
%Ian Costanzo, Alden Kelsey, Fiona Ogren, David Wians
%Professor Brian Savilonis
%August 2014 - March 2015
%Torque Speed Power Curves
%12" Neoprene Fin

clear all; close all;

%Constants
radius = 0.295; %Radius of dyno wheel [meters]
lamda = 0.7315 %Wavelend of fin [meters]
rho = 1000; % Density of water [kg/m^3]
theta = pi/2; % Angle of sweep [rad]
r = .3048; % Radius of fin [meters]
A = theta/2*r^2; %Xsection of Flow [m^2]
R1 = 1; %Initial row for CSV call
C1 = 2; %Column for force sensor data
C2 = 4; %Column for angular velocity data
colorcell = [0.502 0 0; 0 0 0; 0 0 1; 0 1 0; 0 1 1;...
            1 0 0; 1 0 1; 0.502 0.502 1; 0 0.502 0.502; 0 0.251 0];
file = {'VaryTorque_2015-2-13_0233mmps.csv';...
    'VaryTorque_2015-2-13_0311mmps.csv'; ...
    'VaryTorque_2015-2-13_0399mmps.csv';...
    'VaryTorque_2015-2-13_0488mmps.csv'; ...
    'VaryTorque_2015-2-13_0578mmps.csv';...
    'VaryTorque_2015-2-13_0640mmps.csv'; ...
    'VaryTorque_2015-2-13_0855mmps.csv';...
    'VaryTorque_2015-2-13_0969mmps.csv'; ...
    'VaryTorque_2015-2-13_1083mmps.csv';};
V = [.233 .311 .399 .488 .578 .640 .855 .969 1.083]; %Measured Flow Speed
cellsize = size(file);
i = cellsize(1);


while i > 0
filename = file(i);
filename = char(filename);
M = csvread(filename,R1,C1);
sizeM = size(M);
R2 = sizeM(1);
%Torque
force = csvread(filename,R1,C1,[R1 C1 R2 C1]); %Measured force [N]
torque = radius.*force; %Torque [N*m]
```

```
%RPM
sensorangvelocity = csvread(filename,R1,C2,[R1 C2 R2 C2]); %Measured omega
angvelratio = 29.2/47.8; %Ratio to account for radius difference
angvelocity = sensorangvelocity.*angvelratio; %Shaft omega
rpm = 9.5493.*angvelocity;
%Power
power = torque.* angvelocity; %Output power [W]

color = colorcell(i,:);

figure(i)
%Plot Torque RPM
subplot(1,2,1)
hold on
scatter (torque,rpm);
P = polyfit(torque,rpm,1); %Best Fit Torque Curve
N = length(torque);
M = max(torque);
x1 = linspace(0,M,N);
rpmfit = polyval(P,x1);

%Plot Torque Power
subplot(1,2,2)
hold on
scatter (torque, power);
H = polyfit(torque,power,2); %Best Fit Power Curve
powerfit = polyval(H,x1);

%Phase Velocity
[max_value, index] = max(powerfit(:)) %Determine max power
tor(i) = x1(index); %Find related torque
speed(i) = rpmfit(index)    %find related omega
omega = speed./9.9493;
frequency = omega./(2*pi);  %determine frequency
wavespeed = frequency.*0.7315   %phase velocity
maxpower(i) = max(powerfit);


figure (12)
%Plot wave speed
c = linspace(1,10,length(V));
scatter (V, wavespeed,[],c,'filled');
ylabel('Wavespeed [m/s]','FontSize',14);
xlabel('Flow Speed [m/s]','FontSize',14);
title('Wave Speed at Max Power with respect to Flow Speed','FontSize',14);
lsline;
grid on;

i = i-1;
end
```

Efficiency vs Torque Plots, 12” Neoprene Fin Example

```
%WATER HARVESTING MQP
%Ian Costanzo, Alden Kelsey, Fiona Ogren, David Wians
%Professor Brian Savilonis
%August 2014 - March 2015
%Efficency Torque Curves
%12" Neoprene Fin

clear all; close all;

%Constants
radius = 0.295; %Radius of dyno wheel [meters]
lamda = 0.7315 %Wavelend of fin [meters]
rho = 1000; % Density of water [kg/m^3]
theta = pi/2; % Angle of sweep [rad]
r = .3048; % Radius of fin [meters]
A = theta/2*r^2; %Xsection of Flow [m^2]
R1 = 1; %Initial row for CSV call
C1 = 2; %Column for force sensor data
C2 = 4; %Column for angular velocity data
colorcell = [0.502 0 0; 0 0 0; 0 0 1; 0 1 0; 0 1 1; 1 0 0;...
    1 0 1; 0.502 0.502 1; 0 0.502 0.502; 0 0.251 0];
file = {'VaryTorque_2015-2-13_0233mmps.csv';...
    'VaryTorque_2015-2-13_0311mmps.csv'; ...
    'VaryTorque_2015-2-13_0399mmps.csv';...
    'VaryTorque_2015-2-13_0488mmps.csv'; ...
    'VaryTorque_2015-2-13_0578mmps.csv';...
    'VaryTorque_2015-2-13_0640mmps.csv'; ...
    'VaryTorque_2015-2-13_0855mmps.csv';...
    'VaryTorque_2015-2-13_0969mmps.csv'; ...
    'VaryTorque_2015-2-13_1083mmps.csv';};
V = [.233 .311 .399 .488 .578 .640 .855 .969 1.083]; %Flow Speed [m/s]
cellsize = size(file);
i = cellsize(1);


while i > 0
filename = file(i);
filename = char(filename);
M = csvread(filename,R1,C1);
sizeM = size(M);
R2 = sizeM(1);
%Torque
force = csvread(filename,R1,C1,[R1 C1 R2 C1]); %Measured Force [N]
torque = radius.*force; %Torque [N*m]
%RPM
sensorangvelocity = csvread(filename,R1,C2,[R1 C2 R2 C2]); %Measured omega
angvelratio = 29.2/47.8; %Ratio to account for radius difference
angvelocity = sensorangvelocity.*angvelratio; %Shaft omega
rpm = 9.5493.*angvelocity;
%Power
power = torque.* angvelocity; %Shaft Power [W]
flowPower = 0.5*rho*A*V(i)^3; %Available Power [W]
normPower = power./flowPower; %Efficency
```

```
color = colorcell(i,:);

figure(i)
%Plot Efficiency Torque
scatter (torque, normPower);
H = polyfit(torque,normPower,2); %Best Fit Power Curve
N = length(torque);
M = max(torque);
x1 = linspace(0,M,N);
powerfit = polyval(H,x1);
ylabel('Efficency');
xlabel('Torque [N*m]');
title('Efficency vs Power');
grid on;
eff(i) = max(powerfit)

figure(11)
%Plot Efficiency vs Torque
hold on;
grid on;
plot(x1,powerfit,'color',color,'LineWidth',2);
ylabel('Efficiency','FontSize',14);
xlabel('Torque [N*m]','FontSize',14);
title('Efficiency vs Torque, 12" Fin','FontSize',14);
axis([0 15 0 1]);
set(gca,'xTick',0:15)
set(gca,'yTick',0:0.1:1)

Legend=cell(i,1);%  two positions
 Legend{1}='1.08m/s';
 Legend{2}='0.969m/s';
 Legend{3}='0.855m/s';
 Legend{4}='0.640m/s';
 Legend{5}='0.578m/s';
 Legend{6}='0.488m/s';
 Legend{7}='0.399m/s';
 Legend{8}='0.311m/s';
 Legend{9}='0.233m/s';
legend(Legend,'FontSize',12);


i = i-1;
end
```

Dimensionless Plots (n vs C and k vs C), Hybrid Fin Example

```
%WATER HARVESTING MQP
%Ian Costanzo, Alden Kelsey, Fiona Ogren, David Wians
%Professor Brian Savilonis
%August 2014 - March 2015
%Dimensionless efficiency and torque coefficient curves
%HYBRID FIN

clear all; close all;

%Constants
radius = 0.295; %Radius of dyno wheel [meters]
lamda = 0.7315 %Wavelend of fin [meters]
rho = 1000; % Density of water [kg/m^3]
theta = pi/2; % Angle of sweep [rad]
r = .3048; % Radius of fin [meters]
A = theta/2*r^2; %Xsection of Flow [m^2]
R1 = 1; %Initial row for CSV call
C1 = 1; %Column for force sensor data
C2 = 4; %Column for angular velocity data
colorcell = [0.502 0 0; 0 0 0; 0 0 1; 0 1 0; 0 1 1; 1 0 0; 1 0 1;...
            0.502 0.502 1; 0 0.502 0.502; 0 0.251 0];
file = {'VaryTorque_2015-2-11_0331mmps.csv';...  %CSV files
    'VaryTorque_2015-2-11_0403mmps.csv'; ...
    'VaryTorque_2015-2-11_0533mmps.csv';...
    'VaryTorque_2015-2-12_0619mmps.csv';...
    'VaryTorque_2015-2-12_0703mmps.csv';...
    'VaryTorque_2015-2-12_0769mmps.csv';...
    'VaryTorque_2015-2-12_0896mmps.csv';...
    'VaryTorque_2015-2-12_0970mmps.csv';...
    'VaryTorque_2015-2-12_1230mmps.csv'};
V = [.331 .403 .533 .619 .703 .769 .896 .970 1.230]; %Measured flow speeds
cellsize = size(file);
i = cellsize(1);
C = []; %Empty array for storing dimensionless speed
n = []; %Empty array for storing efficiency
k=[];   %Empty array for storing torque coefficients

while i > 0
%File read
filename = file(i);
filename = char(filename);
M = csvread(filename,R1,C1);
sizeM = size(M);
R2 = sizeM(1);

%Torque
force = csvread(filename,R1,C1,[R1 C1 R2 C1]); %Measured force [N]
torque = radius.*force; %Shaft torque [N*m]
flowEng = rho.*V(i).^2.*A.*r; %Flow pressure along radius of fin [J]
torqueCoefficient = torque./flowEng; %Torque coefficient
k = [k; torqueCoefficient];

%RPM
sensorangvelocity = csvread(filename,R1,C2,[R1 C2 R2 C2]); %Sensor omega
```

```
angvelratio = 29.2/47.8; %Ratio to account for radius difference
angvelocity = sensorangvelocity.*angvelratio; %Shaft omega
rpm = 9.5493.*angvelocity;

%Power
power = torque.* angvelocity; %Capture Power [Watts]
flowPower = 0.5*rho*A*V(i)^3; %Available Power [Watts]
normPower = power./flowPower; %Efficiency
n = [n; normPower];

%Speed
v = (angvelocity.*lamda)./(2*pi); %Phase velocity of fin [m/s]
normFlow = v./V(i);    %Speed ratio of phase velocity to flow speed
C= [C; normFlow];

color = colorcell(i,:);

figure(1)
%Plot Speed Power Scatter
hold on
grid on
scatter (normFlow, normPower);
H = polyfit(normFlow,normPower,2); %Best Fit Power Curve
N = length(normFlow);
M = max(normFlow);
x1 = linspace(0,M,N);
powerfit = polyval(H,x1);
ylabel('n [\tau\omega/\rhoAU^{3}]','FontSize',14);
xlabel('C [v_{p}/U]','FontSize',14);
title('n vs C, Hybrid Fin','FontSize',14);
axis([0 .5 0 1]);
set(gca,'xTick',0:0.05:.5)
set(gca,'yTick',0:0.1:1)

figure(2)
%Plot Speed Power Fit
hold on
grid on;
plot(x1,powerfit,'color',color,'LineWidth',2);
ylabel('n [\tau\omega/\rhoAU^{3}]','FontSize',14);
xlabel('C [v_{p}/U]','FontSize',14);
title('n vs C, Hybrid Fin','FontSize',14);
axis([0 .5 0 1]);
set(gca,'xTick',0:0.05:.5)
set(gca,'yTick',0:0.1:1)

Legend=cell(i,1);%  two positions
 Legend{1}='1.230m/s';
 Legend{2}='0.970m/s';
 Legend{3}='0.896m/s';
 Legend{4}='0.769m/s';
 Legend{5}='0.703m/s';
 Legend{6}='0.619m/s';
 Legend{7}='0.533m/s';
 Legend{8}='0.403m/s';
 Legend{9}='0.331m/s';
```

```
legend(Legend,'FontSize',14);

i = i-1;
end
figure (3)
%nC Plot
hold on
grid on
scatter (C,n)
B = polyfit(C,n,2);
N = length(C);
M = max(n);
x1 = linspace(0,M,N);
fit = polyval(B,x1);
plot(x1,fit,'color',color,'LineWidth',4);
ylabel('n [\tau\omega/\rhoAU^{3}]','FontSize',14);
xlabel('C [v_{p}/U]','FontSize',14);
title('n vs C, Hybrid Fin','FontSize',14);
axis([0 .5 0 1]);
set(gca,'xTick',0:0.05:.5)
set(gca,'yTick',0:0.1:1)
legend('Data points for all measured flowspeeds','Best fit of data');

figure (4)
%kC Plot
hold on
grid on
scatter (C,k)
B = polyfit(C,k,1);
N = length(C);
M = max(n);
x1 = linspace(0,M,N);
fit = polyval(B,x1);
plot(x1,fit,'color',color,'LineWidth',4);
ylabel('k [\tau/\rhoU^{2}Ar]','FontSize',14);
xlabel('C [v_{p}/U]','FontSize',14);
title('k vs C, Hybrid Fin','FontSize',14);
axis([0 .5 0 1]);
set(gca,'xTick',0:0.05:.5)
set(gca,'yTick',0:0.1:1)
legend('Data points for all measured flowspeeds','Best fit of data');
```